Mapping of Electroencephalogram (EEG) Responses to Newsvendor Decision Model and Cerebral Hemodynamic Responses to Transcranial Photobiomodulation (tPBM) in Humans

Nghi Cong Dung Truong

Presented to the Faculty of the Graduate School of
The University of Texas at Arlington in Partial Fulfillment
of the Requirements for the Degree of

DOCTOR OF PHILOSOPHY

THE UNIVERSITY OF TEXAS AT ARLINGTON
May 2022

Acknowledgments

First of all, I would like to acknowledge my supervising professor, Dr. Hanli Liu, who allowed me to join her lab and has constantly supported me. I greatly appreciate her guidance, patience, thoughtfulness, and constant encouragement. Without her help and support, I could not reach the point I have today.

Second, I would like to thank my committee members, Dr. Alexandrakis, Dr. Nerur, and Dr. Chen, for their willingness to be my dissertation committee. I appreciate their time, support, and constructive feedback.

I would also like to thank Dr. Xinlong Wang for his help and support from the first day I came to Dr. Liu's lab. Thanks for being patient with me and always willing to help with everything anytime.

I am grateful for the time working with Dr. Wu in preparing the OISI system, as well as all the time I joined the lab. Thanks very much for his patience, thoughtfulness, encouragement, and helpful advice.

I have had such an excellent opportunity to work with amazing labmates: Dr. Parisa Rabbani, Dr. Liangchieh Ma, Dr. Yudhajit Das, Dr. Hashini Wanniarachchi, Dr. Tyrell Pruitt, Dr. Phuong Pham, Sadra Shahdadian, Akhil Chaudhri, Shu Kang, Devarshi Desai, Sakshi Ranade, and Saurabh Nair. Thanks for their tremendous support, help, advice, and discussions during these three years. I feel so grateful that I have been in the lab.

Thank you to everyone who gave me their support and help in one way or another during these three years.

Finally, I would like to thank my parents, sister, and big family, who have always supported and encouraged me throughout my long journey. Without them, I wouldn't have come this far. Special thanks to my husband and kids for their unconditional love, encouragement, patience, and immense support. Thanks for coming and being a particular part of my life.

Nghi Truong
May 05, 2022

Abstract

Mapping of Electroencephalogram (EEG) Responses to Newsvendor Decision Model and Cerebral Hemodynamic Responses to Transcranial Photobiomodulation (tPBM) in Humans

Nghi Cong Dung Truong

The University of Texas at Arlington, 2022

Supervising Professor: Dr. Hanli Liu

Decision-making is one of the most critical activities of human beings. Various studies have investigated the brain responses to a variety of decision tasks by deploying the EEG data. The first aim of my dissertation was to investigate the neurocognitive mechanisms and correlations across multiple subjects when people make risky economic decisions. A decision-making task was designed based on the newsvendor problem (NP) with two scenarios: low-profit margins (LM) as the more challenging scenario and high-profit margins (HM) as the less difficult one. The EEG signals were acquired from healthy humans while subjects were performing the task. The Correlated Component Analysis (CorrCA) method was adopted to identify linear combinations of EEG channels that maximize the correlation across subjects or trials. The inter-subject or inter-trial correlation values (ISC or ITC) of the first three components were estimated to investigate the modulation of the task difficulty on subjects' EEG signals and respective correlations. The alpha- and beta-band power of the projection components obtained by the CorrCA was also calculated to assess the brain responses across multiple task periods. Finally, the CorrCA forward models, which represent the scalp projections of the brain activities by the maximally correlated components, were further translated into source distributions of underlying cortical activity using the exact Low

Resolution Electromagnetic Tomography Algorithm (eLORETA). In Chapter 2, I reported strong and significant correlations in EEG signals among multiple subjects and trials during the more difficult decision-making task than the easier one. Experimental results also disclosed that the NP decision-making and feedback tasks desynchronized the normalized alpha and beta powers of the CorrCA components, reflecting the engagement state of subjects. Source localization results also suggested several sources of neural activities during the NP decision-making process, including the dorsolateral prefrontal cortex (DLPFC), anterior PFC (aPFC), orbitofrontal cortex (OFC), posterior cingulate cortex (PCC), and somatosensory association cortex (SAC).

My second aim focused on the mechanistic understanding of transcranial photobiomodulation (tPBM) effects. Over the past decade, tPBM has been considered a safe and effective brain stimulation modality being able to enhance cerebral oxygenation and neurocognitive function. To better understand the underlying neurophysiological effects of tPBM in the human brain, a 111-channel functional near infrared spectroscopy (fNIRS) system was utilized to map cerebral hemodynamic responses over the whole head to 8-min tPBM with 1064-nm laser given on the forehead of 19 healthy participants. Instead of analyzing broad-frequency hemodynamic signals (0-0.2 Hz), frequency-specific effects of tPBM on three infra-slow oscillation (ISO) components consisting of endogenic, neurogenic, and myogenic vasomotions were investigated. Chapter 3 reported significant changes induced by tPBM in spectral power of oxygenated hemoglobin concentration (Δ[HbO]), functional connectivity (FC), and global network metrics at each of the three ISO frequency bands for three ISO frequency bands. Experimental results revealed that tPBM significantly increased endogenic Δ[HbO] powers over the right frontopolar area near the stimulation site. Also, tPBM enabled significant enhancements of endogenic and myogenic FC across cortical regions as well as of several global network metrics.

My third aim sought to derive a theoretical analysis to quantify how the signal-to-noise ratio

(SNR) of a near infrared spectroscopy (NIRS) device influences the accuracy on calculated changes of oxy-hemoglobin (Δ[HbO]), deoxy-hemoglobin (Δ[HHb]), and oxidized cytochrome c oxidase (Δ[oxCCO]). In theory, all NIRS experimental measurements include variations due to thermal or electrical noise, drifts, and disturbance of the device. I applied the error propagation analysis to compute the variability or variance of Δ[HbO], Δ[HHb], and Δ[oxCCO] depending on the system SNR. The quantitative expressions of variance or standard deviations of changes in chromophore concentrations were derived based on the error propagation analysis and the modified Beer-Lambert law. In order to compare and confirm the derived variances versus those from the actual measurements, two datasets of broadband NIRS (bbNIRS) measurements using a solid tissue phantom and the human forearm were collected. A Monte Carlo framework was also executed to simulate the bbNIRS data under two physiological conditions for further confirmation of the theoretical analysis. Finally, the confirmed expression for error propagation was utilized for quantitative analyses to guide optimal selections of wavelength ranges and different wavelength combinations for minimal variances of Δ[HbO], Δ[HHb], and Δ[oxCCO] in actual experiments.

Contents

List of Tables

List of Figures

List of Abbreviations

ANOVA	Analysis of Variance
BA	Brodmann Area
bbNIRS	Broadband Near Infrared Spectroscopy
CBPT	Cluster-based Permutation Test
CCO	Cytochrome C Oxidase
CorrCA	Correlation Component Analysis
DLPFC	Dorsolateral Prefrontal Cortex
EEG	Electroencephalogram
eLORETA	Exact Low Resolution Electromagnetic Tomography Algorithm
FC	Functional Connectivity
FDR	False Discovery Rate
fMRI	Functional Magnetic Resonance Imaging
fNIRS	Functional Near Infrared Spectroscopy
HbO	Oxy-hemoglobin
HHb	Deoxy-hemoglobin
HM	High-profit Margins
ISC	Inter-Subject Correlation
ISO	Infraslow Oscillations
ITC	Inter-Trial Correlation
LM	Low-profit Margins
MEG	Magnetoencephalography
MC	Monte Carlo
NIRS	Near Infrared Spectroscopy
NP	Newsvendor Probem
OISI	Optical Intrinsic Signal Imaging
OFC	Orbitofrontal Cortex
oxCCO	Oxidized Cytochrome C Oxidase
PCC	Posterior Cingulate Cortex
PFC	Prefrontal Cortex
PBM	Photobiomodulation
rPFC	Right Prefrontal Cortex
SAC	Somatosensory Association Cortex
SD	Standard Deviation
SNR	Signal-to-Noise Ratio
tPBM	Transcranial photobiomodulation

Chapter 1

Introduction

1.1 Significance and Specific Aims

Biological image processing, algorithm development, and signal-to-noise analysis are several key components to achieve successful medical images that can provide physiological and functional information to better understand human conditions for either healthy human beings or patients with certain diseases. In particular, neuroimaging tools, such as multi-channel electroencephalogram (EEG) and multi-channel functional near infrared spectroscopy (fNIRS), have been used to investigate brain functions in response to task-driven or neuromodulation-driven interventions. Accordingly, my dissertation focused on algorithm developments and image analyses for two specific topics: (1) to map EEG responses to the newsvendor decision model so as to understand how the human brain reacts to such a risk decision-making problem in the business context, and (2) to map cerebral hemodynamic responses to transcranial photobiomodulation (tPBM) in healthy humans. Furthermore, since tPBM has become an important neuromodulation tool for treating several neurological disorders, it is essential to monitor hemodynamic and metabolic enhancement by tPBM. It becomes critical to determine appropriate broadband NIRS (bbNIRS) devices for the need. Thus, my third aim was to perform a Signal-to-Noise Ratio analysis to determine the variance of chromophore concentration quantification in bbNIRS.

1.1.1 Newsvendor Problem decision-making task and the need for understanding underlying neurocognitive mechanisms using electroencephalogram (EEG)

Decision-making, one of the most critical activities of humans, is influenced by a complicated interplay among available information, external factors, and internal biases or constraints. Various studies on decision-making have focused on unveiling neurocognitive mechanisms while making decisions or identifying the engagement of different brain regions in such a process [81, 105, 107, 151, 218]. Different brain imaging modalities, including functional magnetic resonance imaging (fMRI) [53, 103, 108, 173], electroencephalography (EEG) [63, 182, 198], and magnetoencephalography (MEG) [61, 203], can be employed concurrently with various decision-based tasks to investigate underlying neural mechanisms while making decisions.

The newsvendor problem (NP) is one of the well-known problems in the field of operations management [147, 148] and behavioral research [177]. Such a problem deals with stocking level decisions in the presence of uncertainty and costs associated with overstocking and understocking. The newsvendor model has been applied to diverse decision-making contexts in manufacturing and service industries, as well as in operation management. My first aim sought to investigate the neurocognitive mechanism underlying economic decision-making. The decision-making task was designed based on the newsvendor problem (NP). Two NP-based scenarios were designed: (1) low-profit margins (LM) resulting in high difficulty to make money and (2) high-profit margins (HM) resulting in low difficulty to make money. EEG signals were acquired while subjects were making business decisions throughout performing the NP-based tasks.

Unlike previous risk decision-making studies, I focused on analyzing the relationship between subjects' engagement while playing the NP tasks and two difficulty levels. The correlation component analysis (CorrCA) method [46, 47] was first employed to identify spatial combinations of

EEG signals that maximize the correlation across multiple subjects or trials. The inter-subject correlation (ISC) or inter-trial correlation (ITC) of the EEG signals, which is considered a marker of the attentional state [46, 47], was estimated and statistically analyzed to investigate the effects of the task difficulty on subjects' engagement. I also analyzed further the spectral power of spatially filtered EEG signals, namely, CorrCA projection components, to understand better cortical synchrony or desynchrony of brain responses evoked through different NP task periods. Finally, the scalp projections of the brain activities by the correlation components were translated into distributions of underlying cortical activity. The source analysis suggested possible sources of neural activities, which helps to induce hypotheses about the spatial origins of neural activities while performing the NP-based task.

1.1.2 Need for quantifying tPBM-induced changes in infraslow oscillations (ISO) of hemodynamic signals and functional connectivity at three ISO frequency bands

Over the past decade, photobiomodulation (PBM) has gained considerable interest as an innovative modality for various disease treatments. This technique uses low-dose light from red to near-infrared (630-1100 nm) to modulate tissue. Transcranial PBM (tPBM), which refers to PBM applied on the cerebral cortex, has also been demonstrated to enhance neural function and human cognition [15, 49]. tPBM mechanism has been suggested in relation to cytochrome c oxidase (CCO), a biological agent absorbing light in the NIR range [34, 93].

My second aim shared the data reported earlier [201] that utilized a 111-channel fNIRS system concurrently with tPBM delivered on the right prefrontal cortex (rPFC) of 19 healthy participants to investigate the cerebral hemodynamic activity over the whole cortex. Complementary to the previous work [201] only considering Δ[HbO] signals of a few PFC channels, I assessed the whole-head Δ[HbO] time series. The cluster-based permutation test (CBPT) [17, 122, 138, 144] was applied to identify cortical regions having significant increases in Δ[HbO] induced by tPBM. Prior studies using bbNIRS have demonstrated that tPBM leads to significant increases of Δ[HbO] of the channel nearby the stimulation site [158, 195, 211]. However, no study has been investigated tPBM-evoked changes of brain-wide Δ[HbO].

I also examined the changes in hemodynamic power, FC, and global topographical network metrics of three infra-slow oscillation (ISO) frequency bands: endogenic, neurogenic, and myogenic. A few existing tPBM-related studies assessed FC computed from EEG [59, 232], fMRI [45, 130], or broad frequency band fNIRS [201], but not frequency-band-specific fNIRS. Therefore, this work would help answer our major question: does tPBM modulate hemodynamic power, FC, and global topographical network metrics differently for these three frequency bands? If so, which frequency bands are more responsive to tPBM? The hypothesis was that tPBM would enhance FC at specific frequency bands, depending on molecular mechanisms of tPBM. By the end of this work, I observed significant improvements in FC for endogenic and myogenic frequency bands, which confirmed our hypothesis. Moreover, the enhancement of FC induced by tPBM in specific cortical regions observed in our study supported reported findings of improved brain functions following tPBM.

1.1.3 Need for computational analysis to quantify how signal-to-noise ratio (SNR) of a near infrared spectroscopy (NIRS) device influences the accuracy of calculated chromophore concentration changes

Near-infrared spectroscopy (NIRS) is a well-known non-invasive modality to monitor/measure changes in chromophore concentrations. Beyond two main chromophores of interest in most NIRS-based studies, namely, oxyhemoglobin (HbO) and deoxyhemoglobin (HHb), researchers have gained more interest in investigating the metabolic changes in tissue by measuring the oxidation state of the metabolic enzyme cytochrome c oxidase (oxCCO). However, measuring oxCCO using NIRS is more complex than HbO and HHb due to its low concentration percentage compared to hemoglobin and broad spectral signature. Broadband NIRS (bbNIRS) [13, 75, 101, 102, 124], which provides a full or broad wavelength range of measurement, is expected to offer reliable quantification results of changes in oxCCO (Δ[oxCCO]), beyond HbO (Δ[HbO]) and HHb (Δ[HHb]).

Since Δ[HbO], Δ[HHb], and Δ[oxCCO] must be inferred from the optical densities measured at multiple wavelengths, measurement variations caused by the system's thermal or electrical noise, drifts, and disturbance will lead to variability in the quantification results. To my knowledge, very few studies have been addressed such a problem. Most existing works have focused on the effect of extinction coefficients, optical pathlengths, or wavelength combinations on the accuracy of the estimated chromophore concentration changes. Thus, my third aim focuses on investigating the influence of SNR of a NIRS system on quantifications of Δ[HbO], Δ[HHb], and Δ[oxCCO]. In theory, all measured data are not noise-free; they must consist of natural variability or uncertainty from the measurement system. The accuracy of the results derived from these measurements will depend on the measurement errors or SNR [19, 64]. In other words, measurement variances or errors will propagate to the quantified results. Note that the objective of this study was to quantify the SNR-derived variance of Δ[HbO], Δ[HHb], and Δ[oxCCO] caused only by the noise of the NIRS instruments/devices. Other parameters, such as the extinction coefficients and the optical pathlengths, are not the concern of variables in this study.

1.2 Dissertation Outline

The dissertation consists of five chapters and one appendix. This first chapter briefly introduces the research strategy and significance of three specific aims. The three following chapters correspond to one accepted paper (Chapter 4) and two manuscripts that were submitted (Chapters 2 and 3).

Chapter 2 investigates the neural mechanisms underlying the NP-based decision-making process and the potential sources of neural activities involved in such a complex process. Chapter 3 presents the study utilizing a 111-channel fNIRS system concurrently with tPBM delivered on the right prefrontal cortex. The results of ISO powers of Δ[HbO], ISO-specific functional connectivity, and global topographical network metrics under the active/sham tPBM conditions are presented in this chapter. Chapter 4 proposes a quantification framework to assess the influence of the signal-to-noise ratio of the measurement system on the variance of calculated chromophore concentration changes in the bbNIRS system. Finally, chapter 5 concludes the main findings of the dissertation and proposes some general perspectives.

Chapter 2

Mapping and Understanding of Correlated Electroencephalogram (EEG) Responses to the Newsvendor Problem

Nghi Cong Dung Truong, Xinlong Wang, Hashini Wanniarachchi, Yan Lang,
Sridhar Nerur, Kay-Yut Chen, Hanli Liu

(This chapter is a manuscript that has been submitted to Scientific Reports)

2.1 Introduction

Decision-making, one of the most critical activities of humans, is influenced by a complicated interplay among available information, external factors, and internal biases or constraints. Various studies on decision-making have focused on unveiling neurocognitive mechanisms while making decisions or identifying the engagement of different brain regions in such a process [81, 105, 107, 151, 218]. Functional magnetic resonance imaging (fMRI) has been the most popular brain imaging modality for determining different brain areas involved in the decision process [53, 103, 108, 173]. However, although fMRI can provide high spatial resolution images of cerebral activities, its poor temporal resolution limits its application in studies requiring precise information regarding the relative timing of decision signals. Other imaging modalities with a better temporal resolution than that of fMRI, including electroencephalography (EEG) [63, 182, 198] and magnetoencephalography (MEG) [61, 203], are employed to capture the fast neural responses underlying decision-making.

Many studies have utilized EEG concurrently with various decision-based tasks to investigate underlying neural mechanisms while making decisions [28, 54, 63, 89, 137, 218]. Different EEG characteristics were analyzed to assess the decision-induced effects. For instance, Wyart et al. [218] demonstrated that the delta band's slow oscillations of EEG signals during categorical decisions were strongly correlated with the decision weight on a categorical choice. In [54], Fink et al. investigated variations of EEG alpha power while subjects were making moving decisions in a soccer match. They observed substantial decreases in alpha power of parietal and occipital cortices in subjects making more creative moves. Golnar-Nik et al. [63] extracted different features from EEG power and demonstrated that the customer's decision to buy a product could be predicted using those features with high accuracy. Besides analyzing EEG oscillations of different frequency bands, many EEG studies on risk decision-making focused on analyzing event-related potentials (ERPs) [71, 197, 217]. Different ERP components such as Feedback Related Negativity (FRN), P3, N5, or N200 [153, 194, 227] were investigated to understand the neurocognitive mechanism underlying decision-making under risk. Other techniques, including Independent Component Analysis (ICA) [181], Linear Discriminant Analysis (LDA) [182], or Canonical Correlation Analysis (CCA) [6], were also employed to extract event-related salient features. These features can be used to predict people's future behavior or decisions based on the current outcomes [63, 154].

The present study sought to investigate the neurocognitive mechanism underlying economic decision-making. The decision-making task was designed based on the newsvendor problem (NP) [147, 177, 214], which emulates the problem experienced by newspaper vendors when they have to make a stocking decision every morning for an optimal profit. If the newspaper vendors stock too much and are unable to sell all the stocked newspapers, they would incur investment and inventory costs. On the contrary, if the vendors stock too little, they will lose the opportunity to earn more profit. In our experiment, participants faced the same dilemma as the NP when playing a computer game in which they had to decide the product quantity they wanted to stock [198]. Two NP-based scenarios were designed: (1) low-profit margins (LM) resulting in high difficulty to make money and (2) high-profit margins (HM) resulting in low difficulty to make money. EEG signals were acquired while subjects were making business decisions through performing the NP-based tasks.

This paper presents some novel analysis and findings. We applied the Correlated Component Analysis (CorrCA) method, developed by Dmochowski et al. [46, 47], to our specific EEG data acquired while subjects performed the NP-based, decision-making task. The CorrCA method was previously employed along with only natural audiovisual stimuli [39, 46, 47, 92, 95, 155]. In our study, the stimulus was not synchronized among participants in nature, but our results from both ISC and ITC analysis revealed significant correlation and modulation of the attention state of subjects through different decision-making periods and across two levels of task difficulty. Moreover, the power analysis of projected EEG signals confirmed the brain engagement or attention state of players, especially within the decision period. Finally, the forward models obtained by the CorrCA method, which represent the scalp projections of the brain activities by the maximally correlated components, were further translated into distributions of underlying cortical activity using the exact Low Resolution Electromagnetic Tomography Algorithm (eLORETA) [8, 141]. The results derived from eLORETA suggested potential sources of neural activities involved in working memory, effortful attention, computational and emotional processing.

2.2 Materials and methods

2.2.1 Participants and experimental setup

A total of 31 healthy subjects (mean age ± standard deviation (SD) of 26 ± 6.5 years) were recruited for this study. The experimental protocol was approved by the Institutional Review Board (IRB) of the University of Texas at Arlington. All methods were performed in accordance with the relevant guidelines and regulations. Informed consent was obtained from each participant prior to all measurements.

All subjects were healthy and did not have any neurological or psychiatric disorder history. Subjects were randomly assigned to two groups corresponding to two NP-based scenarios: LM and HM. In the former, subjects found it hard to earn profit and frequently lose their money. Contrarily, in the HM context, subjects could easily gain substantial profit and rarely lost their money. The NP-based task protocol was explained to subjects prior to the experiment. Subjects could also try the game a few times (maximum 5) before starting the measurement. Participants were paid according to the equivalent accumulative profit they earned at the end of the experiment.

The whole experiment consisted of 30 s of resting-state and 40 consecutive trials as shown in Figure 3.1A. Each trial included a maximum of 20 s for the decision period, 5 s for resting before receiving 10 s feedback on the profit, and finally another 5 s of rest before starting the subsequent trial. The decision and feedback screens are depicted in Figure 3.1B-C. During the decision period, subjects needed to decide the product quantity they wanted to buy based on the provided information, including the cost, the price, and the demand range of the product. The decision had to be made within 20 s. After 20 s, the product quantity would be set to 0 automatically, and the software switched to 5 s of the resting period. Feedback on the profit of the last trial was then displayed on the feedback screen for 10 s. EEG data were acquired throughout the whole experiment using a 64-channel EEG instrument (ActiveTwo, Biosemi, Netherlands). After carefully assessing the EEG data quality, we excluded 8 subjects due to the low signal-to-noise ratio, leaving 23 subjects, 12 for the LM and 11 for the HM groups.

2.2.2 EEG signal preprocessing

64-channel EEG data were preprocessed using the EEGLAB toolbox [43]. The raw EEG signals were first bandpass filtered between 1-70 Hz and further notch filtered at 60 Hz to remove undesired

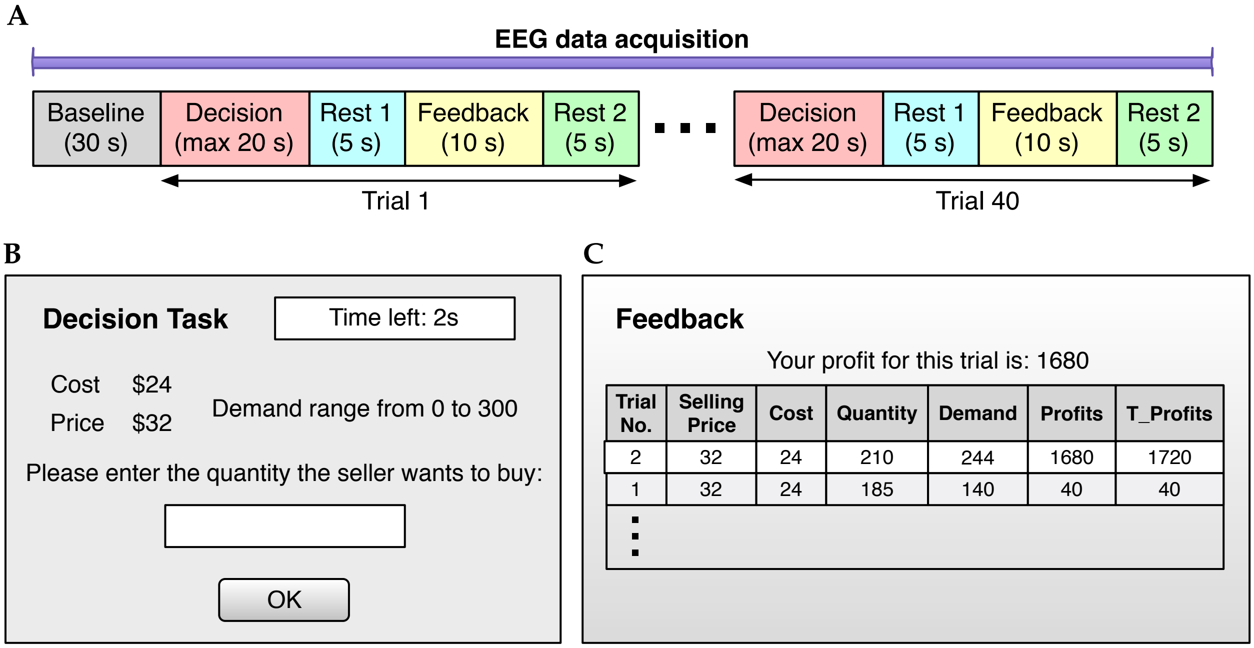

Demand range from 0 to 300

Please enter the quantity the seller wants to buy:

Your profit for this trial is: 1680

Trial No.	Selling Price	Cost	Quantity	Demand	Profits	T_Profits
2	32	24	210	244	1680	1720
1	32	24	185	140	40	40
⋮						

Figure 2.1: Experimental protocol. (**A**) Diagram of the NP-based experimental protocol. The whole experiment consisted of 30 s of rest (baseline) and 40 consecutive trials. Each trial included a maximum of 20 s of decision, 5 s of the first rest, 10 s of feedback, and 5 s of the second rest. EEG data were recorded throughout the whole experiment. (**B, C**) Computer screens of decision and feedback phases shown to subjects during the NP-based task.

frequencies. Artifacts from eye blinks, eye movements, or jaw clenches were then removed using the Independent Component Analysis (ICA) method [30]. Finally, outlier EEG samples, whose magnitude exceeded four standard deviations of the channel's mean, were replaced by zeros. Steps of the EEG preprocessing procedure are depicted in Figure 3.2A.

2.2.3 Correlation component analysis (CorrCA) across multiple subjects or trials

The first step in our EEG data analysis pipeline was to identify spatial combinations of EEG signals that maximize the correlation across multiple subjects or trials by using the CorrCA method developed by Dmochowski et al. [46, 47]. The principle of CorrCA was similar to PCA, except that the components were computed to maximize the correlation of EEG data among multiple subjects or trials. CorrCA helped to convert EEG data from the electrode-by-time format to the

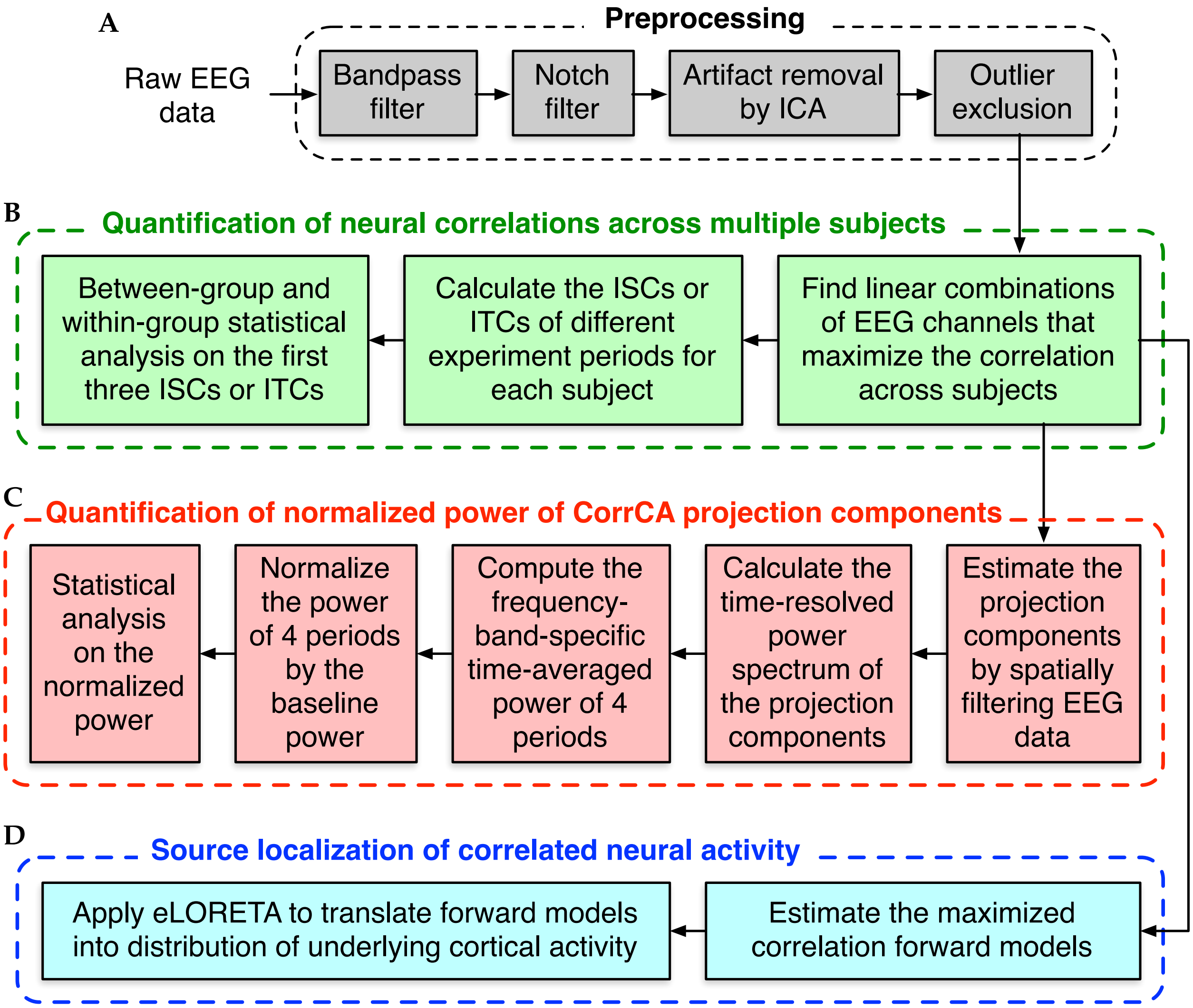

Figure 2.2: Flowchart for EEG data analysis. (**A**) EEG data preprocessing procedure. (**B**) Processing procedure for quantifying neural correlations across multiple subjects or trials. (**C**) Steps for investigating of normalized power of CorrCA projection components. (**D**) Steps for source localization of correlated neural activities.

component-by-time format, in which each component corresponds to an electrode combination. These components are sorted in descending order of across-subject or across-trial correlation. Since we kept only a few first correlated components, the number of components was much smaller than the number of electrodes, which helps mitigate the high-dimensionality problems of EEG data and makes further analysis of data more efficient.

Given our specific experimental design, we opted for the CorrCA in two different data structures to maximize the inter-subject or inter-trial correlation (ISC or ITC). The EEG data generation for these two analyses was slightly different and is illustrated in Figure 2.3.

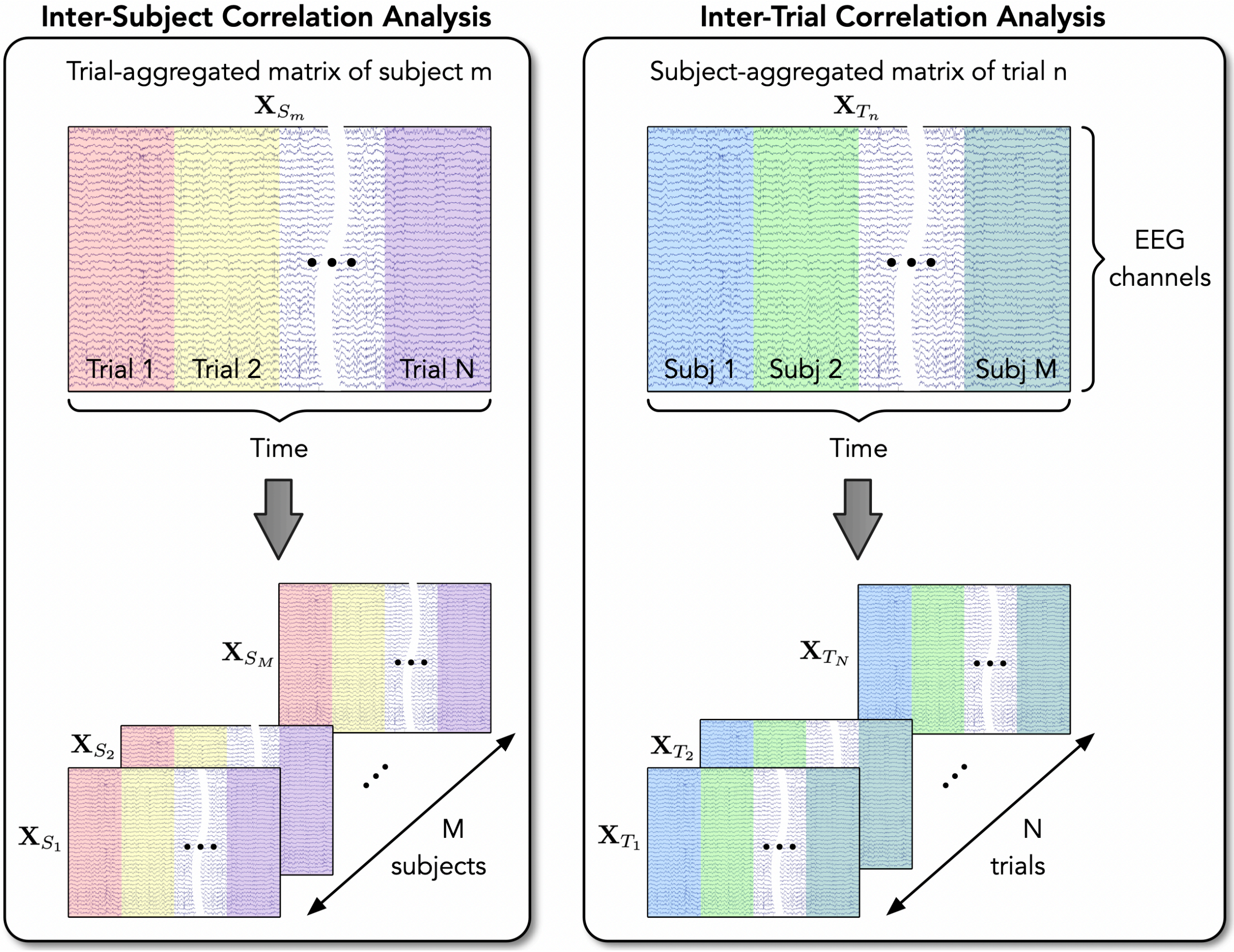

Figure 2.3: Illustration of the EEG data generation for the ISC and ITC analyses.

For the ISC, we defined the trial-aggregated matrix $\mathbf{X}_{S_m}$ for subject m by concatenating multi-trial data along the temporal axis as follows:

$$\mathbf{X}_{S_m} = \left[\begin{array}{cccc} \mathbf{X}_{S_m,T_1} & \mathbf{X}_{S_m,T_2} & \cdots & \mathbf{X}_{S_m,T_N} \end{array} \right] \tag{2.1}$$

where $\mathbf{X}_{S_m,T_n}$ is the EEG data for trial n of subject m ($m = 1 \ldots M$ and $n = 1 \ldots N$, where M is the total number of subjects and N is the number of trials). $\mathbf{X}_{S_m,T_n} \in \mathbb{R}^{D \times N_T}$, where D is the number of

EEG channels, and N_T is the number of time samples of one trial.

Given M subjects participating in both LM and HM tasks, we had a set of M trial-aggregated EEG data $\left\{\mathbf{X}_{S_1}, \ldots, \mathbf{X}_{S_M}\right\}$. The between-subject covariance $\mathbf{C}_b$ and the within-subject covariance $\mathbf{C}_w$ were calculated as follows:

$$\mathbf{C}_b = \frac{1}{M(M-1)} \sum_{i=1}^{M} \sum_{j=1, j \neq i}^{M} \mathbf{C}_{ij} \tag{2.2}$$

$$\mathbf{C}_w = \frac{1}{M} \sum_{i=1}^{M} \mathbf{C}_{ii} \tag{2.3}$$

where $\mathbf{C}_{ij} = \mathrm{cov}(\mathbf{X}_{S_i}, \mathbf{X}_{S_j})$ is the cross-covariance of EEG signals of subject i and subject j across all EEG channels, and $\mathbf{C}_{ii} = \mathrm{cov}(\mathbf{X}_{S_i}, \mathbf{X}_{S_i})$ is the auto-covariance of EEG signals of subject i.

The linear combinations of EEG channels that maximize the correlation across multiple subjects were the solutions of the generalized eigenvalue problem:

$$\mathbf{C}_w^{-1} \mathbf{C}_b \mathbf{w} = \lambda \mathbf{w} \tag{2.4}$$

We kept three solutions of equation (2.4), $\mathbf{w}_k$ ($k = 1 \ldots 3$), corresponding to the first three largest eigenvalues. The ISC $I_{m,k}^{\langle p \rangle}$ of subject m and component k for period $\langle p \rangle$, including 'DCS' for the decision period, 'R1' for the first rest, 'FB' for feedback, and 'R2' for the second rest, was estimated as follows:

$$I_{m,k}^{\langle p \rangle} = \frac{\mathbf{w}_k^T \mathbf{C}_{b,m}^{\langle p \rangle} \mathbf{w}_k}{\mathbf{w}_k^T \mathbf{C}_{w,m}^{\langle p \rangle} \mathbf{w}_k} \tag{2.5}$$

where the between-subject covariance matrix $\mathbf{C}_{b,m}^{\langle p \rangle}$ and the within-subject covariance matrix $\mathbf{C}_{w,m}^{\langle p \rangle}$

for subject m and experimental period $\langle p \rangle$ were defined as:

$$\mathbf{C}_{b,m}^{\langle p \rangle} = \frac{1}{N}\frac{1}{M-1}\sum_{n=1}^{N}\sum_{i,i\neq m}\left(\mathbf{C}_{im}^{\langle p \rangle_{T_n}} + \mathbf{C}_{mi}^{\langle p \rangle_{T_n}}\right) \tag{2.6}$$

$$\mathbf{C}_{w,m}^{\langle p \rangle} = \frac{1}{N}\frac{1}{M-1}\sum_{n=1}^{N}\sum_{i,i\neq m}\left(\mathbf{C}_{mm}^{\langle p \rangle_{T_n}} + \mathbf{C}_{ii}^{\langle p \rangle_{T_n}}\right) \tag{2.7}$$

where $\mathbf{C}_{im}^{\langle p \rangle_{T_n}}$ is the cross-covariance matrix computed from EEG data within period $\langle p \rangle$ of trial T_n for subjects i and m; $\mathbf{C}_{ii}^{\langle p \rangle_{T_n}}$ is the auto-covariance matrix for subject i computed from EEG data within period $\langle p \rangle$ of trial T_n.

For the case of computing the ITC, we generated the subject-aggregated matrix $\mathbf{X}_{T_n}$ for trial n by concatenating multi-subject data along the temporal axis as follows:

$$\mathbf{X}_{T_n} = \begin{bmatrix} \mathbf{X}_{S_1,T_n} & \mathbf{X}_{S_2,T_n} & \cdots & \mathbf{X}_{S_M,T_n} \end{bmatrix} \tag{2.8}$$

The procedure for finding the linear combinations of EEG channels that maximize the correlation across multiple trials was similar to the process described above, except the input data, in this case, is a set of N subject-aggregated EEG data $\{\mathbf{X}_{T_1}, \ldots, \mathbf{X}_{T_N}\}$, where N is the total number of trials of the whole experiment. The between-trial covariance $\mathbf{C}_b$ and within-trial covariance $\mathbf{C}_w$ were calculated using the cross- and auto-covariance of EEG signals of trials i and j, i.e., $\mathbf{X}_{T_i}$ and $\mathbf{X}_{T_j}$.

The CorrCA procedure was applied to all subjects to obtain the common linear combinations of EEG channels that maximize the correlation across multiple subjects or trials. The ISCs or ITCs of the first three CorrCA components were then calculated for each subject and for different experimental periods. Finally, in the statistical analysis step, we separated the ISCs and ITCs obtained from subjects participating in LM and HM tasks accordingly to investigate the effects of the task difficulty on the ISCs and ITCs of different experimental periods between these two groups. Figure 3.2B outlines the steps for CorrCA across multiple subjects and trials.

2.2.4 Normalized spectral power of spatially filtered EEG signals

We sought to analyze further the spectral power of spatially filtered EEG signals, namely, CorrCA projection components, to better understand cortical synchrony or desynchrony of brain responses evoked through different NP task periods. For example, desynchronization in the alpha band was reported being associated with increased attention [98], while increased alpha oscillations were proposed to reflect an attention suppression mechanism [55].

Given the linear combinations $\mathbf{w}_k$ ($k = 1 \ldots 3$) obtained from the generalized eigenvalue problem in equation (2.4), the projected components $\mathbf{y}_{k,S_m}$ of subject m is defined as follows:

$$\mathbf{y}_{k,S_m} = \mathbf{w}_k^T \mathbf{X}_{S_m} \tag{2.9}$$

where $\mathbf{X}_{S_m}$ is the trial-aggregated EEG data of subject m, including the first 30 s of baseline. Note that although the linear combinations $\mathbf{w}_k$ can be obtained from ISC or ITC analysis, the time-resolved projection component $\mathbf{y}_{k,S_m}$ was calculated using the same EEG data for both cases.

For each projection component $\mathbf{y}_{k,S_m}$, we first computed the power spectral density (PSD) of every 1-sec data segment to generate a $[N_f \times N_t]$ time-resolved power spectrum, where N_f is the number of frequencies, and N_t is the whole task duration in second with the time resolution of 1 sec. Frequency-band-specific power was then calculated for five commonly used EEG frequency bands, namely, delta (0.5-4 Hz), theta (4-8 Hz), alpha (8-13 Hz), beta (13-30 Hz), and gamma (30-60 Hz), by averaging the frequency-dependent power within the corresponding frequency range. We further calculated the time-averaged power of four periods of the NP task, including decision (DCS), first rest (R1), feedback (FB), and second rest (R2) for each trial and the time-averaged power of the baseline. The power during four task/rest periods was also normalized by dividing by the baseline power. Statistical analysis was finally applied to investigate the difference in brain responses across four task/rest phases of two decision-difficulty levels. Figure 3.2C outlines the steps for analysis of normalized power of CorrCA projection components.

2.2.5 Sources of maximally correlated neural activity using eLORETA

As mentioned above, CorrCA led to multiple linear combinations of EEG electrodes that maximize the correlation of neural activity among different subjects or trials while performing the decision-making task. The "forward models", which represent the scalp projections of the brain activities by the correlation components, were computed as follows:

$$\mathbf{A} = \mathbf{C}_w \mathbf{W}(\mathbf{W}^T \mathbf{C}_w \mathbf{W})^{-1} \tag{2.10}$$

where $\mathbf{W}$ is a weight matrix whose columns are K largest eigenvectors with $\mathbf{w}_k$ obtained from equation (2.4). Each column of $\mathbf{A}$ corresponds to a forward model, which depicts an approximate spatial distribution of the neural sources.

To investigate further the sources of correlated neural activity defined by the correlation component, we employed the eLORETA [8, 141] to translate the obtained forward models into distributions of underlying cortical activity. Figure 3.2D outlines the steps for inverse calculations using eLORETA. Compared to standardized LORETA (sLORETA), eLORETA can provide exact localization of deeper sources with zero error despite the presence of both measurement and biological noise [87, 140]. As reported in [87], eLORETA produced more accurate localization of active sources compared to sLORETA.

2.2.6 Statistical analysis

Two-way factorial ANOVA with NP-based task (LM vs. HM) as between-subjects factor and task period (DCS, R1, FB, and R2) as within-subjects factor was first used to investigate the statistical significance for both ISC/ITC and projection component's normalized power. ANOVA assumptions, namely, the normality distribution of each group and the homogeneity of variances, were validated prior to performing the analysis. Post-hoc pairwise comparisons with FDR adjustment for multiple comparisons were then performed to test significant differences between LM and HM tasks within each level of task periods, as well as pairwise comparisons of task periods within each task. We report FDR adjusted p-values for all analyses involving multiple comparisons.

For the case of normalized power, since no significant difference was found between LM and HM groups by the two-way factorial ANOVA, we pooled these two groups and performed one-way repeated-measures ANOVA on the pooled data to test the task period effects. We also verified the normality and homoscedasticity characteristics of the pooled data to ensure that ANOVA usage was appropriate. Post-hoc pairwise comparisons were finally carried out using Tukey adjustment for multiple comparisons to assess significant differences across 4 task phases (DCS, R1, FB, and R2).

2.3 Experimental results

2.3.1 ISC and ITC were modulated by the engagement of subjects

Figure 2.4 presents the ISC and ITC results of the first three CorrCA components of LM and HM tasks for four experimental periods. We employed two-way factorial ANOVA to investigate the statistical significance of ISC/ITC across NP-based tasks (LM and HM) and task periods (DCS, R1, FB, and R2). ANOVA assumptions, including the normality distribution of each group and the homogeneity of variances, were validated before performing the analysis. Two-way factorial ANOVA revealed significant effects of task period factor for both ISC and ITC of the first component ($F = 4.25$, $p = 0.008$ for ISC and $F = 3.56$, $p = 0.019$ for ITC). No significant effects were found for the second and third components.

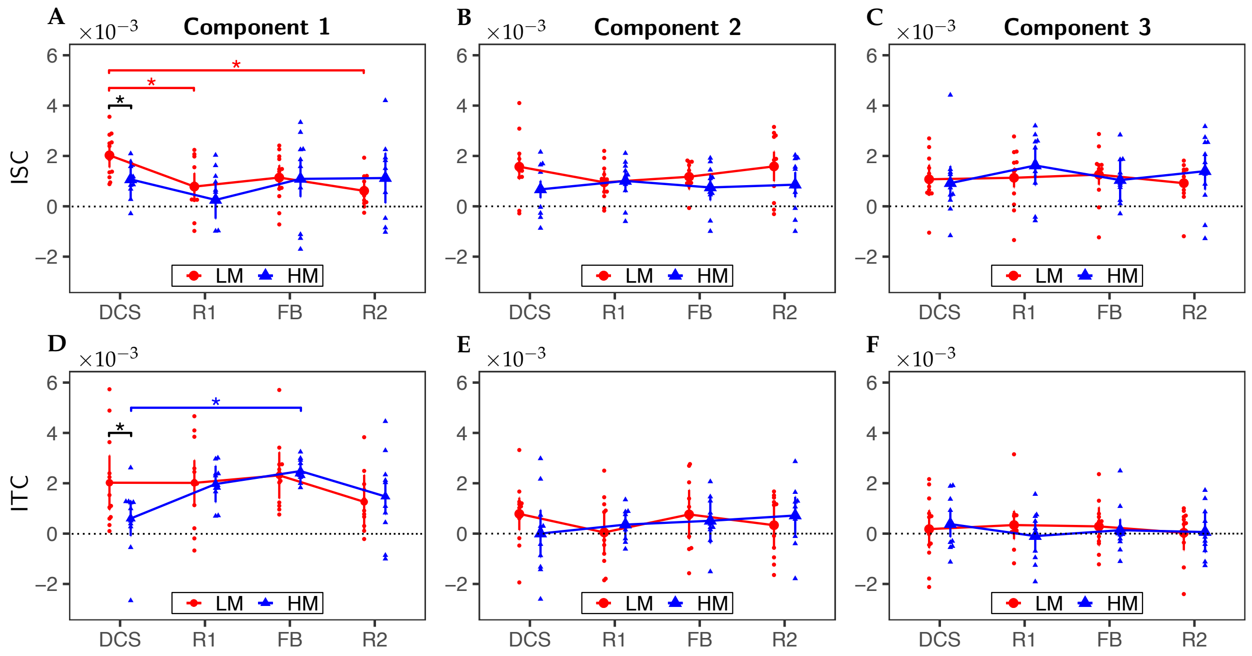

Figure 2.4: Results of the first three CorrCA components for (**A**-**C**) ISC and (**E**-**F**) ITC in response to LM (red; $n = 12$) and HM (blue; $n = 11$) decision-making tasks during four experimental periods, namely, decision (DCS), first rest (R1), feedback (FB), and second rest (R2). Significant differences between a period pair or between LM and HM tasks are marked as '*' for $p < 0.05$ after FDR correction.

For the ISC analysis, follow-up pairwise analyses showed significant differences between DCS and R1 periods ($p_{FDR} = 0.024$, i.e., p-value after FDR correction for 12 comparisons) and between DCS and R2 periods ($p_{FDR} = 0.023$) for the LM task. Moreover, although two-way factorial ANOVA did not show a strong effect of the NP-based task factor ($F = 0.64$, $p = 0.43$), post-hoc analyses still revealed a significant difference between LM and HM tasks only for the DCS period ($p_{FDR} = 0.037$, FDR corrected for 4 comparisons). Overall, the ISC of the first component reached the maximum value during the DCS period for the more challenging task (i.e., the LM task). In other words, neural responses among subjects were strongly correlated by the attentional state, which is depicted clearly in Figure 2.4A by the peak value during the DCS period of the LM task. In principle, the DCS period of the NP-based task would require the most engagement or attention of subjects compared to the other periods. While the HM task allowed the players to gain profit easily, the LM task would force them to engage and focus along with the protocol more promptly or concurrently to achieve profitable outcomes. Thus, ISC was significantly stronger during the DCS period for the LM task than the HM task and stronger than during two resting periods (R1 and R2) of the same LM task.

Post-hoc pairwise analyses for the ITC case showed a marginally significant difference (p_{FDR} = 0.0496, FDR corrected for 4 comparisons) between LM and HM tasks during DCS only, similar to the ISC case, as shown in Figure 2.4D. In addition, another marginally significant difference was found between the DCS and FB periods for the HM task (p_{FDR} = 0.048, FDR corrected for 12 comparisons).

2.3.2 Alterations in alpha- and beta-band power are linked to the attentional state of subjects through different task periods

As mentioned in the statistical analysis section, two-way factorial ANOVA with NP-based task as between-subjects factor and task period as within-subjects factor was first performed to investigate the statistical significance of both factors. Since no significant difference in normalized power of the CorrCA projection components was found between the LM and HM groups by the two-way factorial ANOVA, we pooled these two groups and performed one-way repeated-measures ANOVA on the pooled data to assess the task period effects. Figure 2.5 depicts the normalized alpha- and beta-band power of the pooled data for the first three CorrCA projection components across 4 task periods: DCS, R1, FB, and R2. Figures 2.5A-B present power values of the components obtained

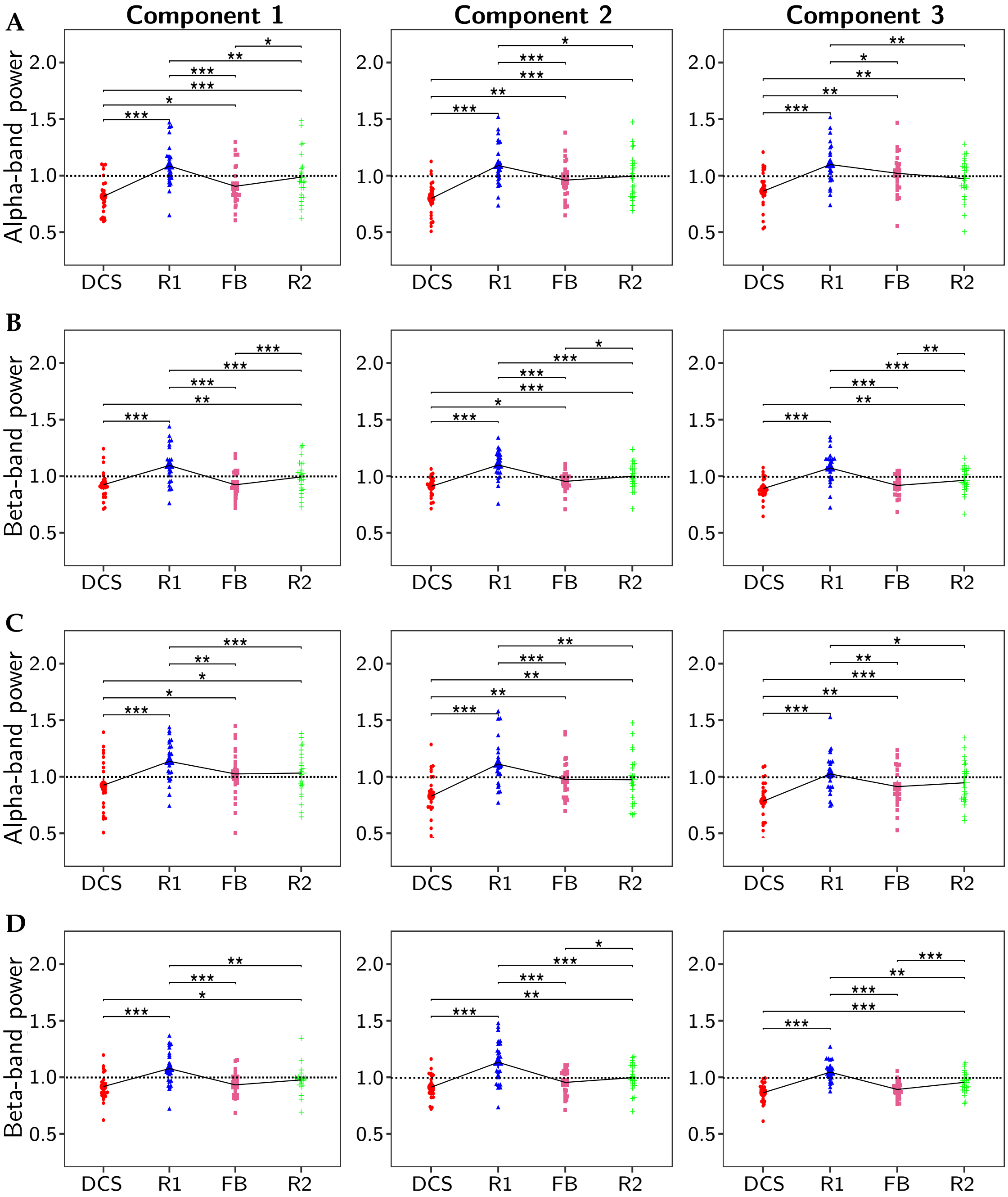

Figure 2.5: Normalized alpha- and beta-band power of the first three CorrCA projection components for ISC and ITC under four task periods (DCS, R1, FB, and R2) pooled from HM and LM. Specifically, (**A**) shows normalized alpha-band power of three ISC projection components; (**B**) normalized beta-band power of three ISC projection components; (**C**) normalized alpha-band power of three ITC projection components; (**D**) normalized beta-band power of three ITC projection components. Statistical results obtained by Tukey multiple comparison tests are mark as '***' for $p_{Tukey} < 0.001$, '**' for $p_{Tukey} < 0.01$, and '*' for $p_{Tukey} < 0.05$.

by the ISC analysis, while Figures 2.5C-D show those of the ITC analysis. ANOVA assumptions, namely, the normality distribution of each group and the homogeneity of variances, were also validated before performing the analysis.

In the case of ISC, one-way repeated-measures ANOVA on the alpha-band normalized power indicated a strong effect of the experimental period factor for all three projection components (component 1: $F = 35$, $p = 1.17 \times 10^{-13}$; component 2: $F = 26.4$, $p = 2.45 \times 10^{-11}$; component 3: $F = 19$, $p = 5.45 \times 10^{-9}$). Post-hoc pairwise comparisons with Tukey adjustment revealed significant differences for multiple period pairs, as shown in Figure 2.5A. Similarly, one-way repeated-measures ANOVA on the beta-band normalized power of the ISC analysis also revealed significant differences among four task periods for all three projection components (component 1: $F = 36.7$, $p = 4.45 \times 10^{-14}$; component 2: $F = 37.3$, $p = 3.3 \times 10^{-14}$; component 3: $F = 39.9$, $p = 7.7 \times 10^{-15}$). Figure 2.5B show the results of Tukey multiple comparison tests among 4 experimental periods.

The alpha- and beta-band normalized power computed from the ITC spatial filters also led to results similar to those in the ISC case. Briefly, for the alpha-band normalized power, one-way repeated-measures ANOVA revealed significant differences among four task periods for all three components (component 1: $F = 14.9$, $p = 1.7 \times 10^{-7}$; component 2: $F = 22.7$, $p = 3.3 \times 10^{-10}$; component 3: $F = 18.6$, $p = 7.6 \times 10^{-9}$). Similarly, for the beta-band normalized power, the statistical results were as follows: $F = 28.1$, $p = 7.8 \times 10^{-12}$ for component 1, $F = 32.7$, $p = 4.5 \times 10^{-13}$ for component 2, and $F = 38.4$, $p = 1.8 \times 10^{-14}$ for component 3. The post-hoc analysis results are presented in Figures 2.5C-D.

Figure 2.5 clearly shows overall similar trends in normalized powers at both alpha and beta bands for both ISC and ITC across four experimental periods. The normalized powers during the DCS phase were lower than 1 across all 12 cases, meaning that the power during the DCS period decreased compared to the baseline. On the contrary, the normalized powers during the R1 period were all higher than 1. For all cases, highly significant differences were found between DCS and R1 periods with $p_{Tukey} < 0.001$. Similarly, the normalized powers during FB were significantly lower than those during R1 in all 12 cases (i.e., at alpha- and beta-bands for both ISC and ITC). Thus, all these results demonstrate that the more the focus of subjects (i.e., during DCS and FB periods), the lower the alpha- and beta-band power. In other words, these results affirm that the engagement state of subjects modulated and reduced the alpha- and beta-band power.

For other frequency bands (Delta, Theta, and Gamma), statistical analysis did not reveal any significant differences across 4 experimental periods and 2 task types. Thus, no report for these frequency bands was presented.

2.3.3 Sources of correlated neural activity for maximally correlated components using the exact Low Resolution Electromagnetic Tomography Algorithm (eLORETA)

As mentioned in Section 2.2.5, we would like to investigate further the brain sources that are responsible for the scalp projections of the brain activities by the maximally correlated components. eLORETA was employed to translate the ISC and ITC forward models into distributions of underlying cortical activity. The eLORETA-derived results suggest possible cortical origins of the neural activity while performing the tasks.

Figure 2.6 depicts the results obtained by using LORETA to estimate the neural source distributions from the scalp projections obtained by the ISC analysis. The localization results for the first component show one primary source in Brodmann Area (BA) 23 (Precuneus, Occipital Lobe), which is involved in memory and emotion [91]. The second component resulted in a significant source corresponding to BA 9 (Medial Frontal Gyrus, Frontal Lobe). BA 9 is believed to be involved in cognitive functions such as working memory, planning, and effortful attention [120]. Finally,

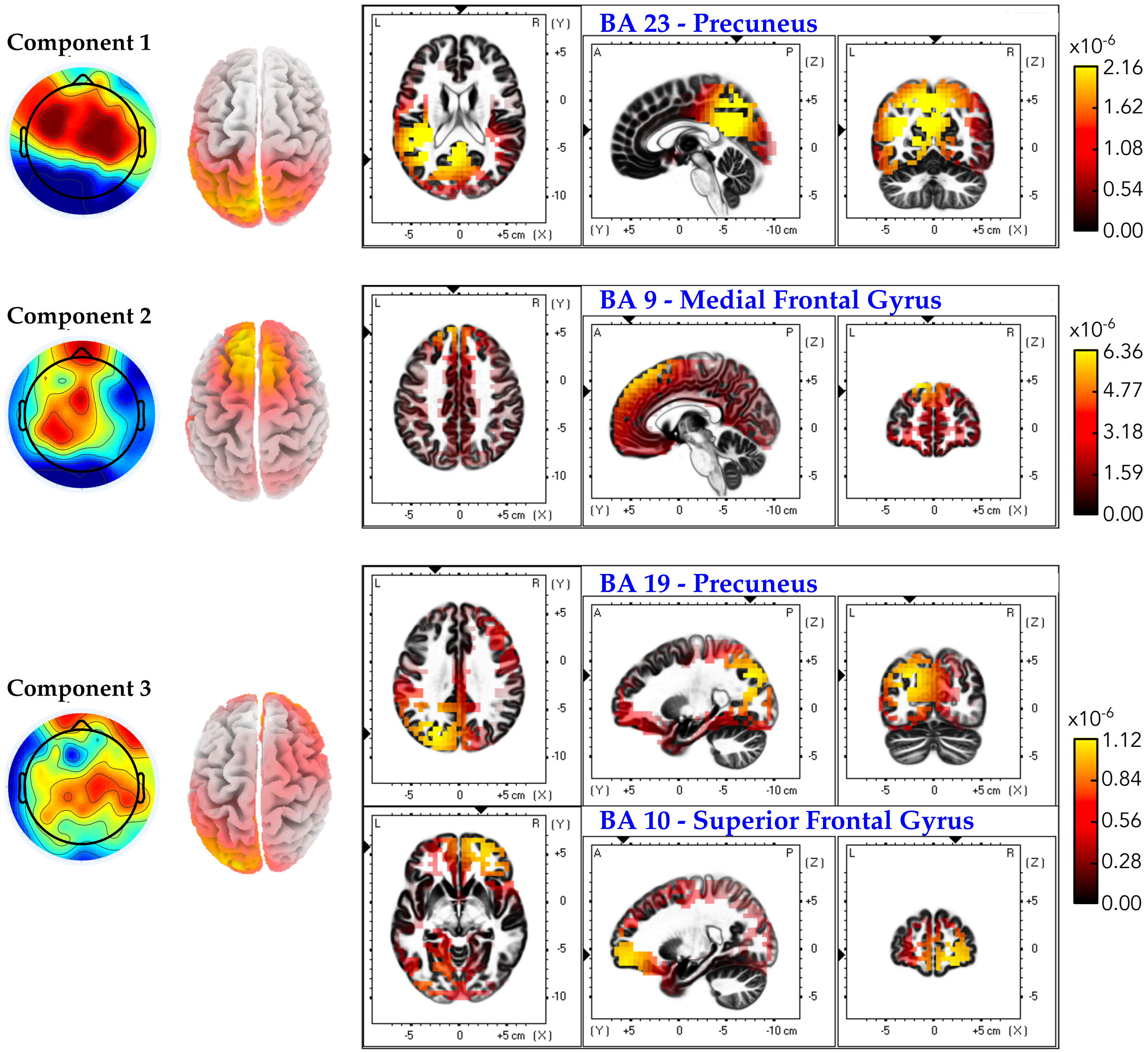

Figure 2.6: Neural source localization results for the first three ISC components. The scalp projections are shown in the top left of each group. The second column presents the estimated source distributions (top view). The remaining plots exhibit three orthogonal slices corresponding to the primary sources of the localization results.

the source analysis of the third component reveals possible sources from the BA 19 (Precuneus, Parietal Lobe) and BA 10 (Superior Frontal Gyrus, Frontal Lobe). While BA 19 is associated with complex processing of visual information, BA 10 is also involved in cognitive functions such as task management and planning.

Similarly, the source localization results from the forward models of the ITC analysis are presented in Figure 2.7. For the first ITC component, the source analysis disclosed one primary source in BA 11 (Inferior Frontal Gyrus, Frontal Lobe), which is involved in thought and cognitive functions. The second ITC component resulted in one primary source from the BA 31 (Cingulate Gyrus, Limbic Lobe) associated with emotion. Finally, the localization results of the third ITC component revealed one primary source in BA 7 (Precuneus, Parietal Lobe). BA 7 is believed to be associated with visual perception.

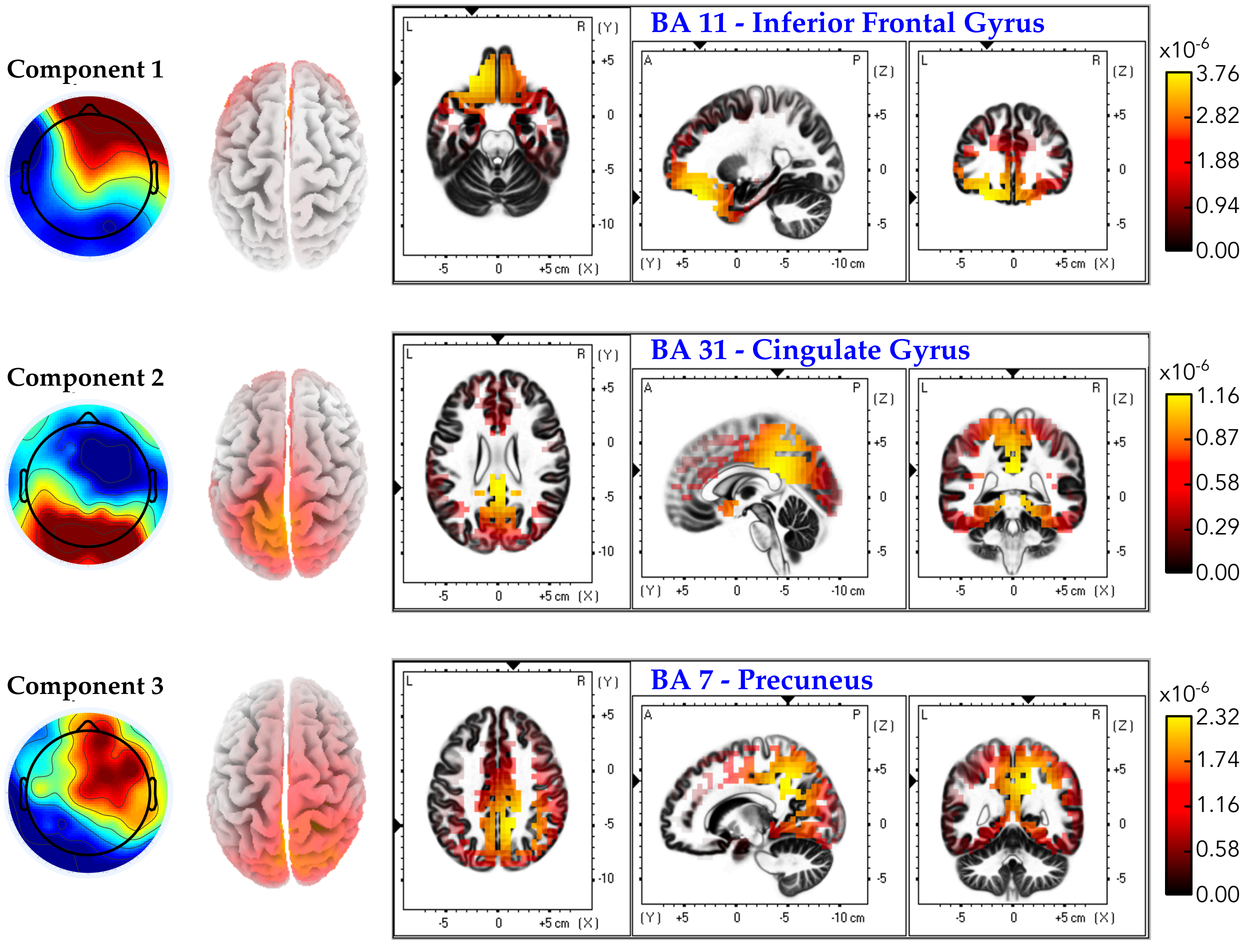

Figure 2.7: Neural source localization results for the first three ITC components. The scalp projections are shown in the top left of each group. The second column presents the estimated source distributions (top view). The remaining plots exhibit three orthogonal slices corresponding to the primary sources of the localization results.

2.4 Discussion

In the present study, we designed a decision-making task based on the principle of NP with two difficulty levels. In such a complex business context, decision-making was influenced by external and internal factors [105], such as provided information, personal experiences, or computational capacity. Neural responses underlying decision-making in this scenario were particularly complicated and altered throughout different experimental periods and trials. Thus, we adopted the CorrCA method [46, 47] to identify linear combinations of EEG channels that maximized the correlation across multiple subjects or trials. We first estimated ISC and ITC of the first three components for different task stages under both LM and HM tasks. Then, each spectral power of the three CorrCA-derived projection components was also computed to investigate the power alterations induced by the task difficulty. Finally, eLORETA [8, 141] was employed to translate the ISC and ITC forward models into source distributions of underlying cortical activity. This final step revealed possible cortical sources while subjects were making decisions through the NP-based task.

2.4.1 Correlations in EEG signals across multiple subjects or multiple trials are modulated by the engagement or attention state

In order to investigate the correlation in EEG signals across multiple subjects and multiple trials, we defined two types of aggregated matrices: (1) trial-aggregated matrix by concatenating multi-trial data along the temporal axis and (2) subject-aggregated matrix by concatenating multi-subject data along the temporal axis. The CorrCA method was then applied to search for the linear combinations of EEG channels that maximize the correlation among subjects or trials. The ISCs and ITCs of the first three components were computed for different experimental periods of both

LM and HM tasks. Both ISC and ITC of the first CorrCA component showed significant differences between LM and HM tasks during the DCS period. Since the effort and concentration requirements during the DCS period were substantially distinctive between LM and HM tasks, the results of ISC and ITC confirmed the modulation of the engagement state of subjects on the correlations in EEG signals across multiple subjects or trials.

We observed different trends in the ITC results of the LM and HM groups over different experimental periods compared with those from the ISC analysis. Such a difference can be explained as follows. For the case of HM, since the player can easily earn the profit without having to think carefully during the decision-making period, the subjects' concentration at this stage decreased more and more throughout multiple trials, which explains why the ITC of the HM task during the DCS period had a weaker ITC value. For the HM group, the highest ITC occurred during the FB period. This observation indicated that subjects were continuously interested in the profits they gained during the game, leading to a higher correlation in the neural signals of the FB period over multiple trials than those during the other periods. For the LM group, because participants always had to think carefully to make the most profitable decisions, the ITC of the LM task during the DCS stage was much higher than that of the HM task. However, although the ITCs of the DCS and FB periods of the LM tasks were higher than those of the resting periods, the differences were not significant as in the ISC case. This observation implies that the correlation in neural responses among trials was weaker than that among multiple subjects.

Existing studies have employed the CorrCA method to investigate the alteration of ISC while subjects were watching movie excerpts [39, 47] or television episodes and commercials [46, 95, 155]. A more recent study assessed neural correlation during music listening using the same method [92]. ISC extracted from the EEG signals has been demonstrated to reflect various cognitive and behavioral states of subjects, including audience appreciations [46, 47], memory retrieval [39], or top-down attention [95]. Unlike the mentioned studies that used natural audiovisual stimuli to investigate the ISC of EEG responses, we adopted the NP-based decision-making task as a semi-natural stimulus. In this case, subjects had to face a variety of cognitive and emotional states from the decision-making stage to the feedback stage. Interestingly, CorrCA demonstrated that the challenge levels of decision making (LM vs. HM) modulated and correlated the attentional state of the neural activity of subjects, as represented by the ISC or ITC. The harder the NP was, the more correlated subjects or task trials were.

2.4.2 EEG power of alpha and delta frequency bands is modulated by the task difficulty

Through the CorrCA method, we were able to identify linear combinations of EEG channels that maximize the correlation across multiple subjects or trials. The CorrCA projection components were then computed by spatially weighting EEG data as spatial filters. We calculated frequency-specific powers of the CorrCA projection components for four experimental periods to investigate further the modulation of the decision difficulty on the spectral power. Statistical analysis revealed significant differences in normalized alpha and beta powers of the three CorrCA components among four task periods. Specifically, the normalized powers during DCS and FB periods were significantly decreased compared to the resting period (i.e., R1). As expected, both DCS and FB periods would require more attention from subjects. Thus, our results demonstrated synchrony reduction of the alpha and beta rhythms by the engagement state of subjects during either DCS or FB.

Our findings were consistent with existing studies in the literature. Various studies have demonstrated correlations between the alpha power of EEG data and the attentional or arousal state of subjects [2, 10, 41, 54, 71, 95, 118]. For instance, alpha power can be used to evaluate subjects' attentional or emotional status while viewing video advertisements [186]. Other studies revealed a decrease of alpha power when people focused on external stimuli [41, 95] or tasks [10, 54]. In [114], the authors investigated the alpha-power lateralization and found that the relationship between alpha-power lateralization and behavioral performance was more complex and depended on baseline alpha power levels.

Furthermore, the beta oscillation was also believed to be strongly correlated with the engagement state of the human brain in cognitive tasks [65, 66, 73, 206] or emotional state during feedback/reward processing [70, 121, 222]. For instance, existing studies have demonstrated a decrease in beta-band power when people made effort to memorize [73, 206] or process provided information [65, 66]. Moreover, the beta oscillation was assumed to respond to feedback or reward events. Several studies sought to investigate the alterations of beta-band power induced by the "gain" or "loss" feedback conditions [70, 222]. In our beta power results, significant differences were found not only between DCS and recovery periods but also between recovery and FB periods. Our results implied that the beta rhythm was strongly correlated among subjects when they received the feedback of gained or lost profit in their last trial during the FB phase.

2.4.3 Source analysis suggests cognitive and emotional involvement

We further applied eLORETA, a source localization method, to translate the ISC and ITC forward models into distributions of underlying cortical activity. Although the analysis of the cortical origins for the scalp projections of the maximally correlated components could only suggest possible sources of neural activities [5, 220], it helps to induce hypotheses about the spatial origins of neural activities while performing the NP-based task. For the case of maximizing ISC, eLORETA results suggested possible sources in the frontal (BAs 9 and 10), parietal (BA 19), and occipital (BA 23) lobes. BA 9 corresponds to the dorsolateral prefrontal cortex (DLPFC), while BA 10 belongs to the anterior prefrontal cortex (aPFC) [50, 58]. Both BAs 9 and 10 are believed to have a significant role in regulating effortful attention and working memory [100, 120, 162]. Various studies on decision-making using fMRI revealed the activation of BAs 9 and 10 during the decision-making process [4, 76, 193]. Our previous study using the same NP-based task with fNIRS also disclosed the brain activation within the DLPFC and partial orbitofrontal cortex (OFC) joined with the frontal polar area (FPA) [214].

Two other potential sources found in the ISC analysis were BAs 23 and 19. BA 23 is considered a part of the posterior cingulate cortex (PCC). Some studies found evidence for the involvement of PCC in the control of cognition and working memory [3, 29, 110, 111], while others demonstrated the PCC activation by emotional stimuli [119, 152]. In our experiment, subjects had to make a decision on the product quantities they wanted to stock and confront a variety of emotional states while receiving feedback on the profits they gained for each trial. Thus, the neural activation of BA 23 in our scenario is reasonable. The last potential activated area, BA 19, corresponds to the visual association cortex. This area is widely known to be associated with complex processing of visual information [86, 125, 126, 183]. Since subjects continuously perceive different information on the computer screen throughout the experiment, the activation of this area is understandable.

For the ITC analysis, the source localization resulted in three potential sources: BAs 11, 31, and 7. BA 11 corresponds to the orbitofrontal cortex (OFC), which has been investigated intensively in various studies relating to decision-making and emotional processing [16, 145, 163, 166]. For instance, Bechara et al. [16] assessed the role of OFC in decision-making in a gambling task. Rolls and Grabenhorst [166] focused on the activation of OFC in emotional processing and decision-making with a variety of rewarding stimuli. Recently, Pelletier and Fellows [145] reviewed different studies regarding the contribution of OFC to value-based decision-making. Our recent study combining the NP-based task and fNIRS [214] also revealed the activation of OFC during the decision-making process.

The second possible source of the ITC analysis was BA 31, belonging to the PCC. Interestingly, BA 31 and BA 23, another potential source found in the ISC analysis, are both subregions of the PCC [112]. Although there are some arguments about the PCC's precise functions due to its specific location that is highly connected with other subcortical regions, some evidence demonstrated that PCC is involved in working memory or computational processes [3, 29, 62, 112]. Finally, the last ITC potential source, BA 7, is a part of the somatosensory association cortex (SAC). The activation of BA 7 may be related to the control of finger movement. Also, BA 7 is believed to be responsive to visual and somatosensory input [69, 170, 231].

2.4.4 Limitations and Future Work

First, our sample size was small, so the statistical power of our analysis was weak. Second, although subjects were informed to limit their motion before participating in the study, they still needed to type their chosen value of the product quantity during the DCS period for each trial. In addition, subjects could possibly experience a variety of emotional states while receiving feedback on the gained profits. Both situations could cause unpredictable and/or uncontrollable body motions of subjects during data acquisition. Although pre-processing steps were applied to remove motion artifacts, such noise may not be completely removable. Third, the protocol needed human subjects to read and enter numbers on a computer keyboard. Those actions would involve or stimulate the visual and sensitometer cortex, which should be discriminated from the measured EEG signal for NP-derived correlation analysis. Last, 64-channel EEG would not facilitate high-spatial-resolution, source-localization images. To overcome all these limitations, a larger subject pool should be planned, while an improved protocol design with less dependence on hand/finger movements as well as with a more channel EEG system would be ideal to accurately map neural responses of the human brain to NP decision-making task phases.

2.5 Conclusion

The present study sought to investigate the neural mechanisms underlying the decision-making process, particularly under the NP context. NP-based decision-making tasks with two challenge levels were designed to assess the modulation and correlation of the task difficulty on subjects' decision-making engagement. We employed the CorrCA method to identify combinations of EEG channels that maximized the correlation across subjects or trials. The ISC and ITC values, which were considered as the attentional state marker, were computed for different task periods at the two difficulty levels. The frequency-specific powers of the CorrCA-derived projection components were also calculated. Finally, eLORETA was used to translate the forward models obtained by the ISC and ITC analyses to the potential primary sources on the human cortex. Experimental results and statistical analysis revealed strong and significant correlations in EEG signals among multiple subjects and trials during the difficult decision-making (LM) task than the easier (HM) task. Also, the NP decision-making and feedback desynchronized the normalized alpha and beta powers of the EEG, reflecting the engagement state of subjects. Source localization results also revealed several cortical/brain areas during the decision-making process, including DLPFC, aPFC, OFC, PCC, and SAC. These potential sources of neural activities were consistent with results presented in previous studies on decision-making, especially the decision-making under the business context.

Chapter 3

Enhancement of Frequency-Specific Hemodynamic Power and Functional Connectivity by Transcranial Photobiomodulation in Healthy Humans

Nghi Cong Dung Truong, Xinlong Wang, Hashini Wanniarachchi, and Hanli Liu

(This chapter is a manuscript that has been accepted for publication in Frontiers in Neuroscience)

3.1 Introduction

Over the past decade, photobiomodulation (PBM) has gained considerable interest as an innovative modality for various disease treatments. This technique uses low-dose light from red to near-infrared (630-1100 nm) to modulate tissue function. A large number of PBM studies on different conditions and diseases has shown positive outcome, including wound healing [40, 127, 146, 223], pain relief [56], traumatic brain injury [38], Parkinson disease [161], and Alzheimer disease [67]. Transcranial PBM (tPBM), which refers to PBM applied on the cerebral cortex, has also been demonstrated to enhance neural function and human cognition [15, 49]. tPBM mechanism has been suggested in relation to cytochrome c oxidase (CCO), a biological agent absorbing light in the NIR range [34, 93]. CCO is an essential enzyme associated with energy generation within the mitochondria and thus a biological mediator of PBM. Light absorption by CCO leads to an increase of CCO activity, release of nitric oxide (NO), and thus an increase of ATP production [80, 142]. As a consequence, tPBM enhances cerebral blood flow (CBF) [109, 131] and brain energy metabolism [159, 165].

Different imaging modalities have been utilized concurrently with tPBM administration to investigate its effects on the brain, such as electroencephalography (EEG) [59, 208], functional magnetic resonance imaging (fMRI) [45, 202], broadband near-infrared spectroscopy (bbNIRS) [158, 175, 195, 211], or functional near-infrared spectroscopy (fNIRS) [78, 201]. Among them, NIRS (both fNIRS and bbNIRS) has been considered as an effective and non-invasive tool for assessing the hemodynamic [23, 24, 160, 176, 205] and metabolic state of the brain [185, 195, 205, 211]. The level of near-infrared light attenuation in tissue can be used to quantify the changes in chromophore concentrations of the investigation site and hence monitor tissue hemodynamic and metabolic state in real time. Both bbNIRS and fNIRS have advantages and disadvantages. The former is able to monitor changes in CCO metabolism but limited with the number of bbNIRS channels, especially for applications that require multi-channel monitoring. On the other hand, fNIRS can provide regional or global mapping of cerebral hemodynamics [36, 214], which helps better understand the influence of any intervention, including tPBM, on different cortical regions.

One primary source of cerebral activity is the vasomotion [1, 25, 26, 204], which is associated to spontaneous oscillations derived from the blood vessel wall. There are three main intrinsic infra-slow oscillation (ISO) components of cerebral activity, including endogenic oscillation (0.003-0.02 Hz) relating to the vascular endothelial metabolic activity [168], neurogenic oscillation (0.02-0.04 Hz) of the intrinsic neuronal activity, and myogenic oscillation (0.04-0.15 Hz) reflecting the vascular smooth muscle activity. ISO can be estimated using fNIRS, followed by appropriate frequency-domain analysis methods [31, 200]. Analyzing cerebral ISO activities facilitates to better understand the neurophysiological responses under different stimulation conditions or diseases.

This work shared the data reported earlier [201] that utilized a 111-channel fNIRS system concurrently with tPBM delivered on the right prefrontal cortex (rPFC) of 19 healthy participants to investigate the cerebral hemodynamic activity over the whole cortex. Compared to our previous work [201], this paper reports several new analysis methodology and novel findings. First, the cluster-based permutation test (CBPT) [17, 122, 138, 144] was applied to the 111-channel fNIRS data to identify tPBM-evoked, brain-wide changes of oxygenated hemoglobin concentration (Δ[HbO]). Second, we analyzed frequency-specific hemodynamic signals by quantifying three ISO-based metrics under the active/sham tPBM conditions. The novel findings of this publication included (1) quantification of ISO powers of Δ[HbO], (2) ISO-specific functional connectivity (FC) across the whole cortex, and (3) global topographical network metrics at three ISO frequency bands. A few existing tPBM-related studies assessed FC computed from EEG [59, 232], fMRI [45, 130], or broad-frequency fNIRS [201], but not frequency-specific fNIRS. Therefore, the current work would help answer two key questions: Does tPBM modulate FC differently at different ISO frequencies? If so, which ISO frequency bands are more responsive to tPBM? We hypothesized that tPBM would enhance FC at specific frequency bands, depending on molecular mechanisms of tPBM. By the end of this work, our results would show significant increase in ISO powers of Δ[HbO], FC and global network metrics for endogenic or/and myogenic oscillations, which confirmed our hypothesis.

3.2 Materials and Methods

3.2.1 Participants

A total of 19 healthy adults (14 men, 5 women), mean age ± standard deviation (SD) of 31.7 ± 9.5 years, were recruited for this study. All participants were healthy and did not have any history of psychiatric or neurological disorders. The experimental protocol was approved by the Institutional Review Board (IRB) of the University of Texas at Arlington (IRB # 2017-0859). Informed consent was required prior to all experiments. Of the original 19 participants, two were excluded due to significant noise during the fNIRS acquisition, which left 17 subjects for further analysis.

3.2.2 Experimental Procedures

We employed a multichannel continuous-wave (CW) fNIRS system (LABNIRS OMM-3000, Shimadzu Corporation, Kyoto, Japan) with laser diodes at three near-infrared wavelengths (780, 805, and 830 nm) to measure cerebral hemodynamic responses. LABNIRS utilized Multialkali photomultiplier tubes as photodetectors, which have a very low quantum yield and have non-detectability at 1064 nm used in our tPBM. Therefore, the interference from the tPBM laser to fNIRS measurements was minimal. Detected signals were sampled at 10.1 Hz. Thirty-two emitters and thirty-four detectors were arranged over the entire head, resulting in a 111-channel layout (Figure 3.1A). Anatomical optode locations with respect to the standard cranial reference points (nasion, inion, left and right preauricular) were determined for each subject using a 3D digitizer (FASTRAK, Polhemus VT, USA). The Montreal Neurological Institute (MNI) coordinates and the corresponding Brodmann Area (BA) for each channel were determined using the NIRS-SPM software [224]. 111 fNIRS channels covered eleven main cortical areas as shown in Figure 3.1B: frontopolar area (FP) (red), dorsolateral prefrontal cortex (DLPFC) (green), Broca's area (purple), BA8 (orange), BA44/45 (pink), premotor cortex (PMC) (blue), primary motor and somatosensory cortices (M1/S1) (yellow), temporal gyrus (cyan), Wernicke's area (olive), somatosensory association cortex (SAC) (teal), and BA39 (gray).

An FDA-cleared 1064-nm CW laser (Model CG-5000 Laser, Cell Gen Therapeutics LLC, Dallas, Texas) was used for noninvasive tPBM [15, 22, 195, 208, 211, 212]. The laser's irradiation area was 13.6 cm^2, and the laser power was set to 3.4 W. This laser power resulted in a power density of 0.25 W/cm^2 and a total energy dose of 1632 J over 8-min tPBM duration ($3.4\ \text{W} \times 60\ \text{s/min} \times 8\ \text{min} = 1632\ \text{J}$). The light was applied by noncontact delivery over the right frontopolar area near the Fp2 location according to the 10/20 international standard system [90] (Figure 3.1B). For sham

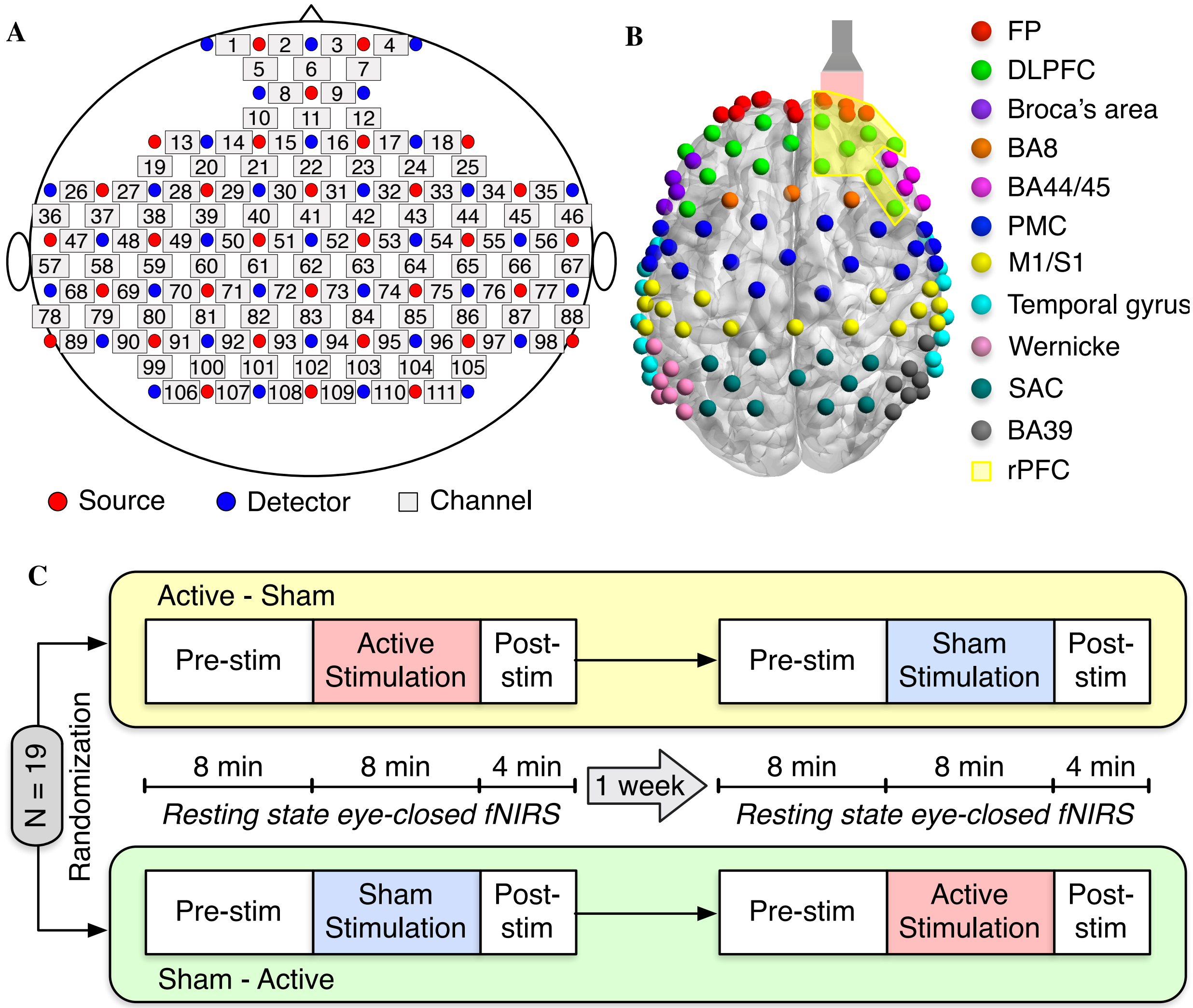

Figure 3.1: Experimental setup and protocol. **(A)** fNIRS source-detector configuration. The source and detector optodes are denoted as the red and blue circles, whereas squares represent the functional channels. **(B)** The distribution of 111 functional channels over different brain cortices: frontopolar area (FP) (red), dorsolateral prefrontal cortex (DLPFC) (green), Broca's area (purple), BA8 (orange), BA44/45 (pink), premotor cortex (PMC) (blue), primary motor and somatosensory cortices (M1/S1) (yellow), temporal gyrus (cyan), Wernicke's area (olive), somatosensory association cortex (SAC) (teal), and BA39 (gray). The flashlight represents the laser beam delivered to the right forehead of the subject. The yellow-shaded area corresponds to the right prefrontal cortex (rPFC). **(C)** Schematic diagram of the experimental protocol. Nineteen subjects were randomly divided into two groups: active-sham or sham-active stimulation. A minimum 1-week waiting period between two visits was required to avoid potential effects from active tPBM.

stimulation, the laser power was set to 0.1 W, and a black cap was placed in front of the laser aperture to further block the light. The reason to keep 0.1 W power was to keep all the electronic components on while the light delivery was zero. The participants would not be aware of the cap since it was put after they closed their eyes. Experimental participants must wear a pair of laser protection goggles throughout the experiment.

Each subject attended two study sessions: active tPBM and sham tPBM. The orders of these two sessions were randomized among nineteen subjects. A minimum 1-week waiting period between two visits was required to avoid any carry-over effects. During the experiment, subjects were instructed to sit comfortably with their eyes closed. The resting-state fNIRS data were recorded for 8 minutes of pre-stimulation, 8 minutes of active/sham stimulation, and 4 minutes of post-stimulation (Figure 3.1C).

3.2.3 Data Preprocessing

Figure 3.2A depicts different steps of preprocessing the resting-state fNIRS data collected in our study. We followed the typical fNIRS data pre-processing pipeline to process our resting-state fNIRS data [79, 149]. The raw voltage data were first converted into optical density data and then into the concentration changes of oxy-hemoglobin (Δ[HbO]) and deoxy-hemoglobin (Δ[HHb]) using the modified Beer-Lambert law [115, 174] with a differential pathlength factor of 6. These two steps were done with the functions from the open-source Homer2 software package [82]. Since Δ[HbO]) and Δ[HHb] may suffer from the systematic drifts due to instrument instability, the linear trend was first estimated using 8-min baseline signals and then subtracted from the whole signals. Subsequently, Δ[HbO] and Δ[HHb] were low-pass filtered using a third-order Butterworth filter with a cut-off frequency of 0.2 Hz to remove physiological noise, such as respiration (0.2-0.5 Hz), heartbeat (1-15 Hz), and other instrument noise [149]. Finally, motion correction using Principle

Component Analysis (PCA) filter [229] was applied to remove motion artifacts. The first two principal components, accounting for the most significant proportion of the variance in the data, were removed from the signals of all channels. Finally, we applied the signal quality index (SQI) algorithm [172] to evaluate the quality of the fNIRS signals. Channels whose SQI was equal to 1, indicating a very low-quality signal, were marked as excluded and would not be considered in the statistical analysis. Of the original 19 participants, two whose fNIRS data had more than 10 rejected channels were excluded, leaving 17 subjects for further analysis. Due to smaller amplitudes and similar inverse patterns of Δ[HHb], we considered only Δ[HbO] for further data analysis.

3.2.4 Data Analysis

3.2.4.1 Mapping Sites of tPBM-induced Significant Increases in Δ[HbO]

As mentioned in Section 4.1, we first considered the whole-head, broad-frequency Δ[HbO] signals and sought to identify cerebral regions responding significantly to tPBM. We applied the CBPT [17, 122, 138, 144] to the whole-head time-resolved Δ[HbO] signals of tPBM and sham sessions. Such an analysis allows us to identify significant spatio-temporal clusters exhibiting hemodynamic responses to tPBM sustained in time and spatial neighbourhood channels. Also, CBPT helps avoid the statistical problem of overly strict correction for multiple comparisons, which multi-channel fNIRS data often encounter.

The principle of permutation-based statistical testing is that observations for different conditions in the null hypothesis are drawn from the same distribution and thus exchangeable. Therefore, if an effect observed in the data is not spurious, it should not be perceived when the data is randomly permuted multiple times. If less than 5% of the permutations show the effect, the null hypothesis is rejected, and the observed effect is considered genuine and thus significant [122]. The CBPT further considers both spatial and temporal adjacency of the observed data based on

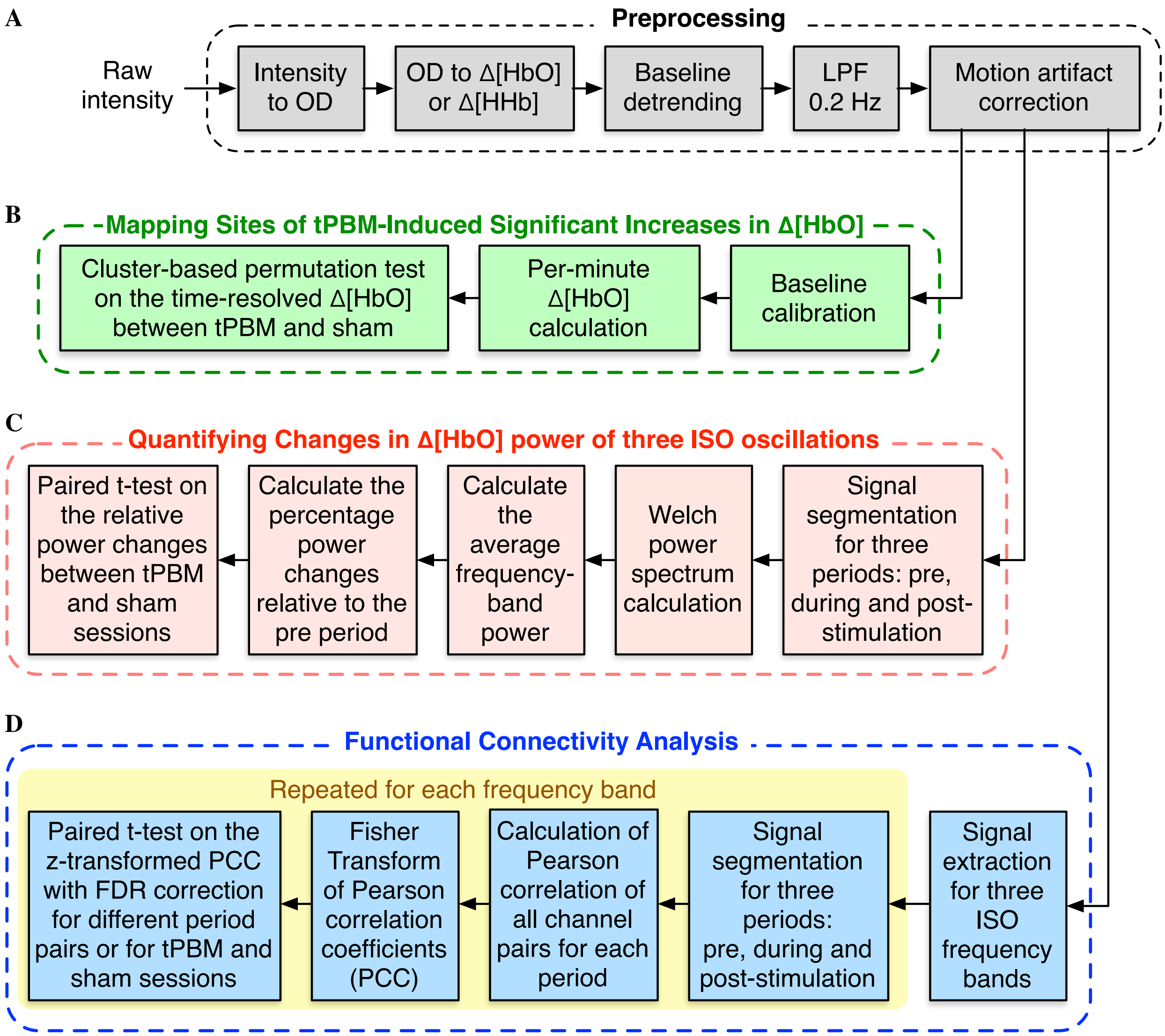

Figure 3.2: Flowchart for fNIRS data analysis. (**A**) fNIRS data preprocessing procedure. (**B**) Processing steps for mapping sites of tPBM-induced significant increases of Δ[HbO]. (**C**) Processing procedure for quantifying changes in Δ[HbO] power of three ISOs. (**D**) Steps for functional connectivity analysis.

the property that observations on neighbouring sites and time points are usually correlated. Once cluster candidates are formed, the cluster-level t-values, estimated as the sum of t-values of all data points belonging to each cluster, are compared to the permutation distribution of maximal cluster statistics. Such a permutation distribution is generated by randomly permuting the data a large number of times and retrieving the maximum cluster statistics (i.e., the maximum of the cluster-level summed t-values) every time. Any clusters whose cluster-level t-values from the actual data are larger than the 95th percentile of the maximum cluster permutation distribution are considered significant [138, 144].

The processing routine to perform the CBPT-based Δ[HbO] time-series data analysis is shown in Figure 3.2B. First, we calculated the average of Δ[HbO] over 1 min prior to the active/sham stimulation and subtracted it from the corresponding Δ[HbO] time-series. The baseline-calibrated Δ[HbO] signals during 8 min of stimulation and 4 min of post-stimulation were then averaged or segmented for every 1 min. CBPT was finally performed on the time-dependent per-minute Δ[HbO] values of all 111 channels using the functions from the Fieldtrip toolbox [138]. The channel neighbours for spatial clustering were defined within a distance of 2.5 cm from the center channel, which resulted in an average of 4.7 neighbours per channel. The critical cluster threshold for considering a data point (a channel-time pair in our case) as a candidate member of a cluster was computed based on the statistical distribution of the permutation data and the cluster alpha of 0.05. The number of randomizations or permutations was set to 2000. The Monte Carlo method was used to calculate the probability of each cluster. Clusters whose p-values were less than the critical $\alpha_{cluster} = 0.05$ were considered significant.

3.2.4.2 Quantification of Changes in Δ[HbO] Power of three Infra-Slow Oscillations (ISO)

The data analysis on CBPT-based Δ[HbO] time-series given in the previous section only investigated the broad-frequency (0-0.2 Hz) hemodynamic changes without considering frequency-specific oscillations. Our interest in this section is to quantify the changes in Δ[HbO] power at three ISO frequency bands, including endogenic (0.003-0.02 Hz), neurogenic (0.02-0.04 Hz), and myogenic (0.04-0.15 Hz) oscillations. Welch method [215] was used to calculate the power spectral density (PSD) for Δ[HbO] time-series of significant channels (channels 3, 4, and 7) found in Section 3.2.4.1.

The processing procedure is shown in Figure 3.2C. First, we segmented Δ[HbO] signals based on three experimental periods, namely, 8 mins of baseline (*pre*), 8 mins of tPBM/sham (*stim*), and 4 mins of post-tPBM/sham (*post*). Let $P^{c}_{\langle seg \rangle}(f)$ be the Welch power spectrum of Δ[HbO] segment named $\langle seg \rangle$ from channel c, where $\langle seg \rangle$ was noted as '*pre*', '*stim*', or '*post*'. The average power of each ISO frequency band $P^{c}_{\langle seg \rangle, \langle fb \rangle}$ was then computed by averaging the frequency-dependent power within the corresponding frequency range of the ISO frequency band $\langle fb \rangle$, including '*e*' for endogenic, '*n*' for neurogenic, and '*m*' for myogenic. Finally, the percentage changes of the power during tPBM/sham and post-tPBM/sham periods to the power during the baseline period were defined as follows:

$$\Delta P^{c}_{\langle seg \rangle, \langle fb \rangle} = \frac{P^{c}_{\langle seg \rangle, \langle fb \rangle} - P^{c}_{pre, \langle fb \rangle}}{P^{c}_{pre, \langle fb \rangle}} \times 100\% \tag{3.1}$$

The percentage changes in power relative to the baseline power were calculated for both tPBM and sham sessions. Paired t-test was finally employed to investigate the effects of tPBM on the relative changes in Δ[HbO] power of three ISO frequency bands.

3.2.4.3 Quantification of Changes in Functional Connectivity of three ISO Frequency Bands

We desired to investigate further the effect of tPBM on brain connectivity by calculating FC for each experimental period: pre-stimulation, during stimulation, and post-stimulation for both study sessions (active and sham tPBM). Unlike our previously published work [201] that computed FC using Δ[HbO] signals from the entire range of hemodynamic fluctuations (0-0.2 Hz), we calculated FC for three ISO frequency bands. The pipeline of the FC analysis is thus depicted in Figure 3.2D. First, the broadband Δ[HbO] time series was first bandpass filtered to extract the signals corresponding to three ISO frequency bands. The time-series data of each ISO were then segmented for three periods, corresponding to the baseline (*pre*), during tPBM/sham (*stim*), and post-tPBM/sham (*post*). Pearson's correlation coefficients (PCC) were calculated for each pair of 111 fNIRS channels [133]. The PCC matrices were finally converted to z-values using Fisher's r-to-z transformation to ensure normality.

Since the tPBM stimulation site was near the right prefrontal cortex (rPFC), only FCs between channels within the rPFC (yellow shaded region shown in Figure 3.1B) to all other channels were considered for further statistical analysis. We were interested in changes in functional connectivity in both cases: (1) over time (pre vs. during vs. post) within each experimental session (active tPBM or sham) and (2) between experimental sessions (tPBM vs. sham). To investigate the effects of tPBM on brain connectivity over time, we compared the z-transformed PCC between each period pair: stimulation vs. pre, post vs. stimulation, post vs. pre. Paired t-test was used to compare the z-transformed PCC of two periods across subjects within the same experimental session (tPBM or sham). False discovery rate (FDR) correction with q-value = 0.05 was employed for multiple comparison correction. This procedure was applied for both tPBM and sham sessions to ensure the significant differences between any period pair were genuinely provoked by tPBM.

For the between experimental sessions comparison (tPBM vs. sham), paired t-tests with FDR correction was also employed to compare the z-transformed PCC between tPBM and sham experiments of each experimental period. This procedure was repeated for all three periods (pre, during, and post-stimulation) and for three ISO frequency bands.

3.2.4.4 Topographical Network Metrics Analysis for three ISO Frequency Bands

Graph theory analysis (GTA) [113, 134, 135] was also employed to investigate tPBM-induced changes in global topographical network metrics for three ISO frequency bands. For each frequency-specific FC matrix obtained in Section 3.2.4.3, we constructed the neighbourhood graph in which fNIRS channels were considered as nodes and FC between two channels were considered as edges.

The neighbourhood graph was then converted into an adjacency matrix by thresholding it with different sparsity levels S ($0.15 < S < 0.5$) to obtain binary networks. Seven global network metrics, including small-world properties (clustering coefficient C_p, characteristic path length L_p, normalized clustering coefficient γ, normalized characteristic path length λ, and small-world σ) and efficiency parameters (local efficiency E_{loc} and global efficiency E_g), were calculated from the binary networks of three periods (pre, during tPBM/sham, and post) of both study sessions (active and sham tPBM). The global network metrics were finally compared between active and sham tPBM sessions using the relative changes to the baseline period (i.e., pre-tPBM/sham). The relative change of a given network metric was calculated as:

$$\Delta M_{\langle p \rangle, \langle fb \rangle} = \frac{M_{\langle p \rangle, \langle fb \rangle} - M_{pre, \langle fb \rangle}}{M_{pre, \langle fb \rangle}} \times 100\% \tag{3.2}$$

where $M_{\langle p \rangle, \langle fb \rangle}$ denotes the network metric M obtained from the FC of period $\langle p \rangle$ at ISO frequency band $\langle fb \rangle$.

3.3 Results

3.3.1 Mapping Sites of tPBM-induced Significant Increases in Δ[HbO] using CBPT

Figure 3.3 depicts the time-resolved (in minute) topographical t-maps and CBPT results when comparing the whole head Δ[HbO] time series of two study sessions (active and sham tPBM). The positive values in the topographical t-map indicate that the Δ[HbO] values of the active tPBM session were higher than those of the sham tPBM session, whereas the negative values denote the opposite. Black dots represent the channels that contributed to significant clusters obtained by the CBPT ($p_{cluster} = 0.05$).

For the first three minutes after starting the stimulation, no significant differences between

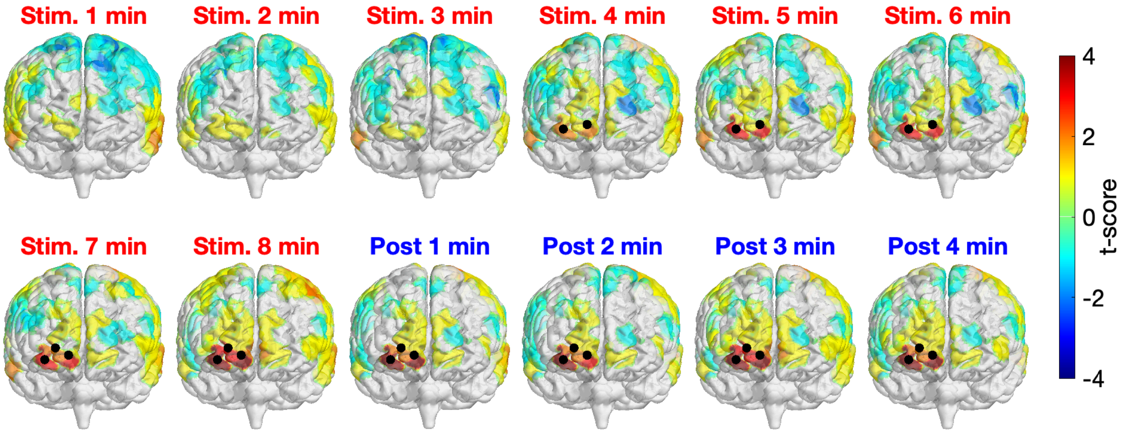

Figure 3.3: Time-resolved topographical t-maps and CBPT results when comparing the whole head Δ[HbO] time series of two study sessions (active and sham tPBM). Black dots indicate the channels that contributed to significant clusters obtained by the CBPT ($p_{cluster} < 0.05$).

active and sham tPBM were detected. Starting from minute 4, CBPT revealed significant differences between active and sham tPBM over the right frontopolar area (channels 3, 4, and then channel 7 starting from minute 7). It is worth noting that the topographical t-maps also show the gradual increase of the t-score values of the channels near the stimulation site (the surface color gradually changed from yellow to orange to bright red and then dark red). Moreover, the increase of Δ[HbO] remained during the 4-min post-stimulation when the stimulation light was off. Therefore, such an increase in Δ[HbO] is expected to truly come from the physiological responses to tPBM. The contamination effect from the laser light would have shown an immediate reduction in Δ[HbO] after the laser ceased.

We also present in Figure 3.4 the time-resolved Δ[HbO] signals of three channels near the stimulation site to better visualize the changes in HbO concentration induced by tPBM. We can notice a gradual increase of Δ[HbO] under the tPBM condition (red curves). As expected, notable differences of Δ[HbO] curves between active and sham tPBM were observed from minute 4 of stimulation. Moreover, the increase of Δ[HbO] remains during the 4-min post-stimulation (minutes

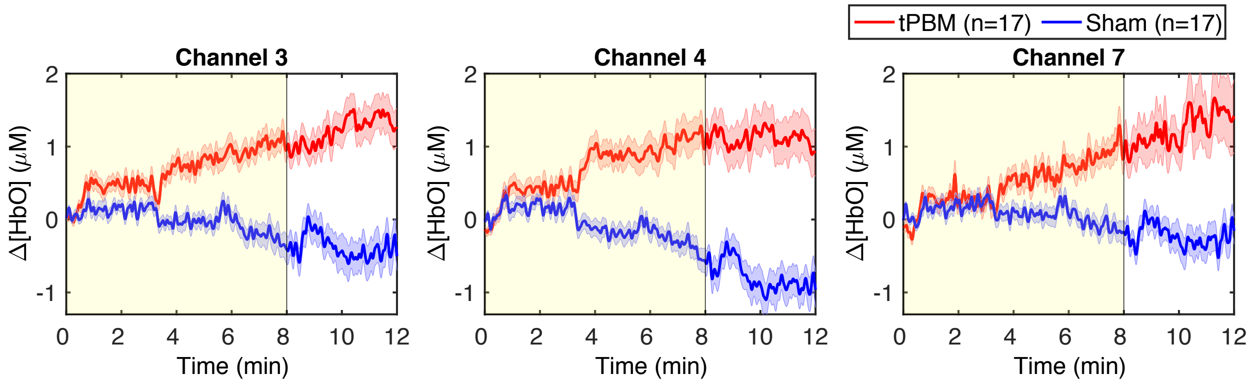

Figure 3.4: Time-resolved Δ[HbO] signals of three channels near the stimulation site: channels 3, 4, and 7. The red and blue curves correspond to the tPBM and sham sessions, respectively. Red and blue shades indicate the standard error of the mean of each group. The yellow shade depicts the stimulation period (8 min).

8 to 12) when the stimulation was off.

3.3.2 Changes in Δ[HbO] Power of three ISO Frequency Bands

To assess tPBM-induced effects on hemodynamic power of three ISO frequency bands, we computed the percentage power changes for both tPBM and sham sessions based on Eq. (3.1). Figure 3.5 depicts the percentage changes of hemodynamic power ΔP of three significant channels detected in Section 3.3.1 for the tPBM/sham stimulation period and the post-tPBM/sham period. Statistical results obtained by paired t-tests between tPBM and sham sessions are marked as '$*$' for $p < 0.05$ and '$**$' for $p < 0.01$. Compared to sham condition, tPBM significantly enhanced ΔP of channel 4 in the endogenic frequency band for both tPBM and post-tPBM periods. Significant increase in relative power changes was also revealed in channel 4 in the neurogenic frequency band during the post-tPBM period.

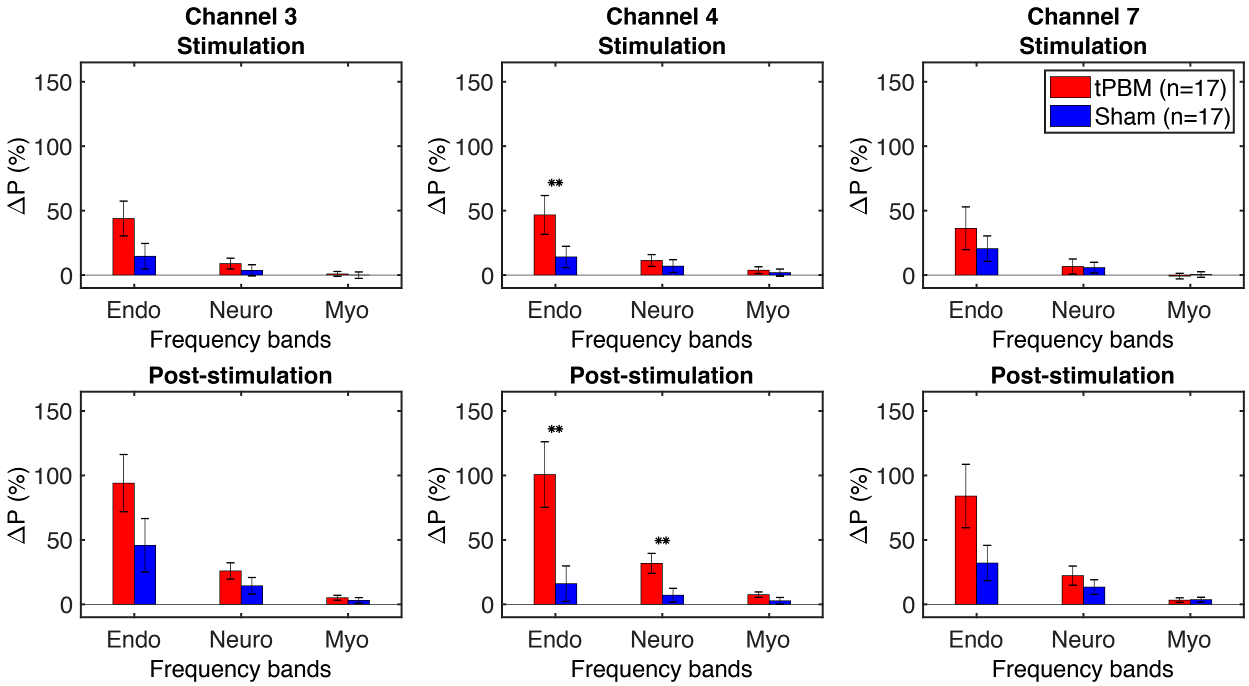

Figure 3.5: Percentage changes of Δ[HbO] power ΔP of three significant channels (3, 4, and 7) for the tPBM/sham stimulation (first row) and post-stimulation (second row) periods. tPBM- and sham-induced ΔP are marked by red and blue bars, respectively. Error bars indicate the standard error of the mean of each group. Statistical results obtained by paired t-tests between tPBM and sham sessions are marked as '∗' for $p < 0.05$ and '∗∗' for $p < 0.01$.

3.3.3 Changes in Functional Connectivity of three ISO Frequency Bands

3.3.3.1 Channel-Wise Analysis of Frequency-Specific FC

As mentioned in Section 3.2.4.3, FC was calculated for three ISO frequency bands. Paired t-tests with FDR correction were first employed to determine significant FC between three pairs of periods, namely, Stim-Pre (during versus pre-stimulation), Post-Stim (post versus during stimulation), and Post-Pre (post versus pre-stimulation) within the same experiment session (active and sham tPBM). Figure 3.6 depicts the t-score maps of FC between three pairs of periods for the endogenic and myogenic bands. For the endogenic frequency band (Figure 3.6A), significant differences in FC were found in the case of active tPBM for the Post-Stim (first row, second column) and Post-Pre stim (first row, third column) pairs ($p < 0.05$, FDR corrected). The connections indicated the stronger FC during post-stimulation than pre or during stimulation. No significant differences in FC were observed for the Stim-Pre pair of the active tPBM experiment (first row, first column). Also, paired t-tests with FDR correction did not reveal any significant FC for all three pairs of periods for the sham tPBM case (second row), which confirmed the genuine effects induced by active tPBM.

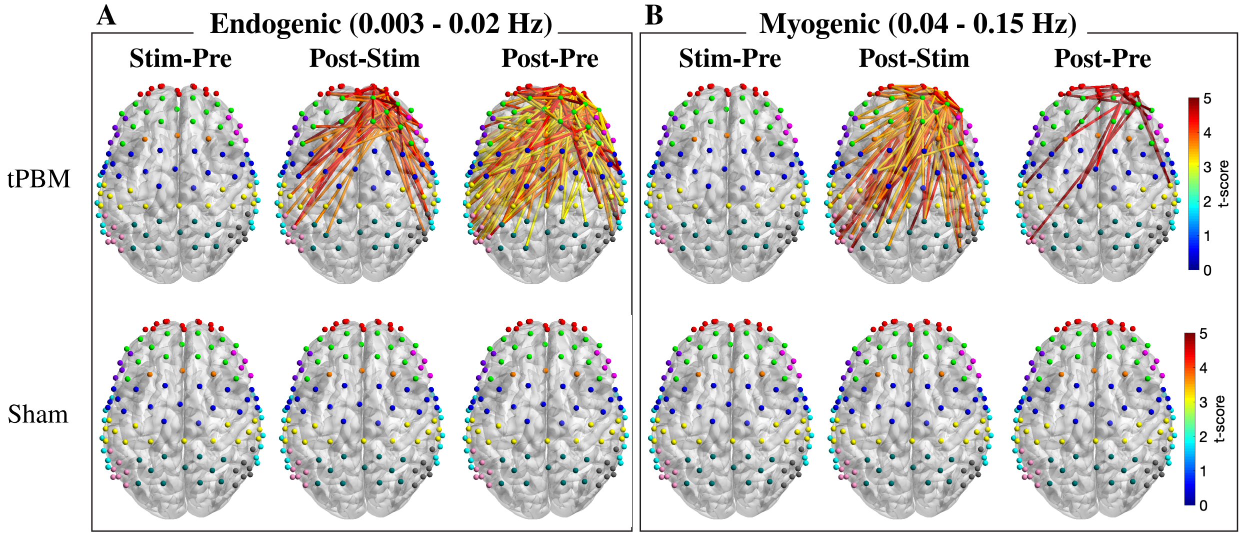

Figure 3.6: T-score maps of significant changes in FC between three pairs of periods for the endogenic and myogenic frequency bands ($p < 0.05$, FDR corrected). Only FC from right PFC to all channels was considered for the statistical analysis. The FC strength was compared between stimulation versus pre-stimulation (Stim-Pre), post- versus during stimulation (Post-Stim), and post- versus pre-stimulation (Post-Pre) for both active (first row) and sham (second row) tPBM.

Specifically, for the Post-Pre pair of the active tPBM experiment (Figure 3.6A), a large number of significant connections ($p < 0.05$, FDR corrected) were observed among channels within the rFP or between rFP and rDLPFC (10 significant connections among channels within the rFP and 8 between rFP and rDLPFC). Other ROI pairs having a high number of significant connections included rDLPFC and lM1/S1 (10), rFP and lDLPFC (7), rDLPFC and rPMC (7), rFP and lPMC (6), rFP and lM1/S1 (5), rFP and BA44/45 (5), rDLPFC and lDLPFC (5), rDLPFC and rDLPFC (6), rDLPFC and lPMC (6), and rDLPFC and Wernicke (5). Thus, in addition to the two regions FP and

DLPFC located close to the excitation region, other ROIs including PMC, M1/S1, and Wernicke also showed significant improvements in FC between them and the rPFC.

Meanwhile, the myogenic band exhibited more and stronger FC for the Post-Stim period pair than Stim-Pre and Post-Pre pairs for the case of active tPBM (first row of Figure 3.6B). Many significant connections were found when comparing FC between Post-Stim. FC during post-stimulation was also enhanced compared with the pre-stimulation phase. Once again, no significant FC was found for the case of sham tPBM for all three pairs of periods (second row of Figure 3.6B).

For the neurogenic band, statistical analysis of FC between three pairs of periods could not reveal any significant changes in connections for both active and sham tPBM experiments. Thus, no report for this frequency band was presented.

Regarding the comparison between tPBM and sham sessions, no significant difference in FC was revealed after paired t-tests with FDR correction for any experimental period (pre, during, or post-stimulation) for all three ISO frequency bands. Thus, we did not report any results for this comparison.

3.3.3.2 Region-Wise Analysis of Frequency-Specific FC

To further understand the changes of FC over different periods, we also calculated the region-wise difference in FC of three period pairs of the active tPBM experiment. The average FC of all connections between two ROIs was first calculated, and the difference in region-wise FC between two periods, including Stim-Pre, Post-Stim, and Post-Pre, was then computed. Topographical maps of the region-wise difference in FC at the endogenic frequency band were depicted in Figures 3.7A-C, exhibiting a gradual enhancement of FC starting from the stimulation phase to the post-stimulation phase compared to pre-stimulation. FC during the stimulation period improved slightly compared to pre-stimulation (Figure 3.7A), which explains why paired t-tests with FDR correction did not reveal any significant connection when comparing these two periods (Figure 3.6A). FC during post-stimulation compared to the stimulation phase was enhanced more than the Stim-Pre period pair, which resulted in several significant connections after applying paired t-tests with FDR correction (Figure 3.6A). The region-wise difference in FC for this period pair (Figure 3.7B) also shows higher values than the Stim-Pre pair. In consequence, we observed higher difference in FC when comparing post and pre-stimulation periods (Figure 3.7C), as well as much more significant connections after paired t-tests with FDR correction as shown in Figure 3.6A.

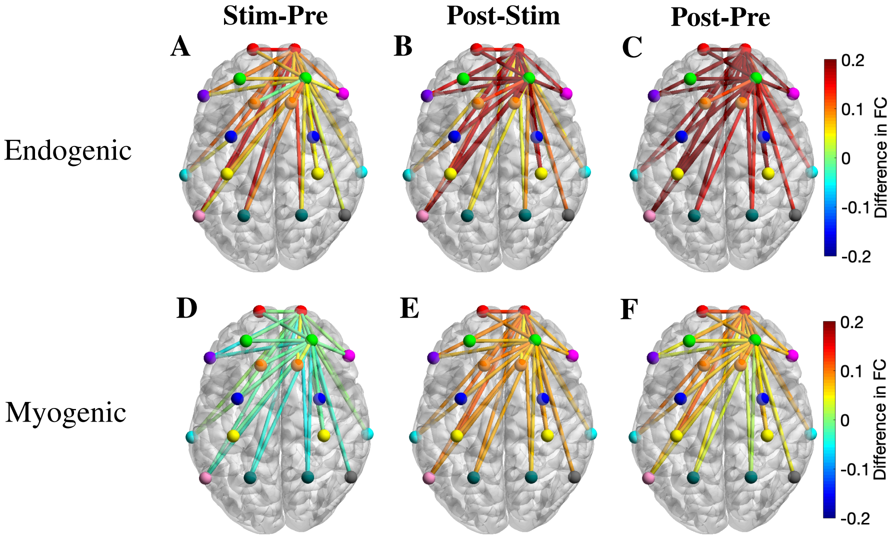

Figure 3.7: Topographical maps of the region-wise difference in FC between three pairs of periods for two frequency bands: (A-C) endogenic and (D-F) myogenic. ROIs include left and right frontopolar area (lFP; rFP) (red), left and right dorsolateral prefrontal cortex (lDLPFC; rDLPFC) (green), Broca's area (purple), left and right BA8 (lBA8; rBA8) (orange), BA44/45 (pink), left and right premotor cortex (lPMC; rPMC) (blue), left and right primary motor and somatosensory cortices (lM1/S1; rM1/S1) (yellow), left and right temporal gyrus (lTemporal; rTemporal) (cyan), Wernicke's area (olive), left and right somatosensory association cortex (lSAC; rSAC) (teal), and BA39 (gray). Only FC from (lFP; rFP) and (lDLPFC; rDLPFC) to all ROIs was plotted.

The region-wise topographical maps of the difference in FC at the myogenic frequency band exhibited a slight decline in whole-head FC during the stimulation period compared to the pre-stimulation (Figure 3.7D). However, such a decline was not significant (i.e., no significant connection was found in Figure 3.6B). During the post-stimulation, global FC was enhanced notably, resulting in a large number of significant connections between channels from rPFC to all other channels observed for the Post-Stim pair of periods. Overall, FC was also improved after tPBM (the Post-Pre pair, Figure 3.6B).

3.3.4 Changes in Global Topographical Network Metrics for three ISO Frequency Bands

As mentioned in Section 3.2.4.4 the relative changes of seven global network metrics were calculated for each ISO frequency band and for during and post-stimulation periods. Then, paired t-tests were used to compare the relative changes of network metrics between tPBM and sham conditions. In this section, we report only the GTA results revealed to be significantly different between these two experimental conditions.

Figure 3.8 shows relative changes of three global topological metrics, namely, global efficiency, local efficiency, and characteristic path length, during the stimulation period at the myogenic frequency band. Briefly, global efficiency (E_g) depicts how information propagates efficiently through the whole network, while local efficiency (E_{loc}) measures the average efficiency of information transfer within a node's neighborhood [27]. Finally, the characteristic path length corresponds to the average shortest path length between all pairs of nodes in the graph [169].

GTA results showed that global and local efficiency were improved thanks to tPBM stimulation. Meanwhile, the characteristic path lengths during tPBM stimulation were significantly shortened than those under the sham treatment. Shorter path lengths indicate that tPBM enhanced network information exchange. As a consequence, both global and local efficiency of the topological network was improved due to the shorter characteristic path length induced by tPBM.

No significant differences were found during the post tPBM/sham period at the myogenic frequency band, as well as during both periods (i.e., during and post tPBM/sham) at endogenic and neurogenic bands. Thus, no report for other periods at other frequency bands was presented.

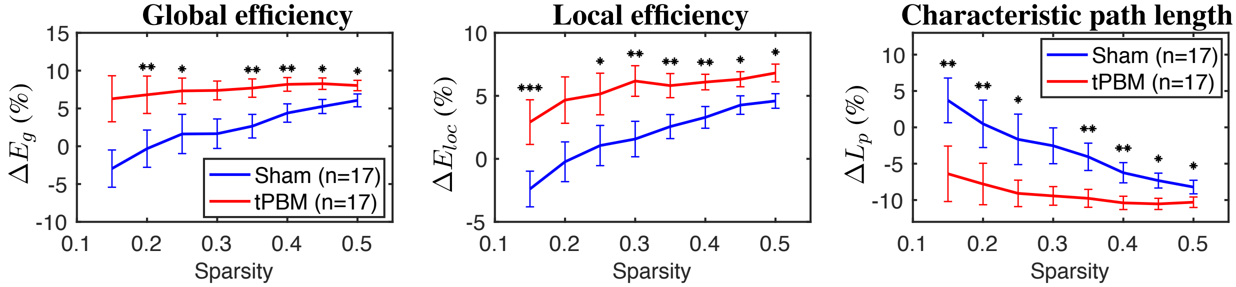

Figure 3.8: The relative changes of three global topological metrics during the stimulation period for the myogenic frequency band (from left to right: global efficiency, local efficiency, and characteristic path length). Significant differences between tPBM and sham conditions are marked by black stars: '$*$' for $p < 0.05$, '$**$' for $p < 0.01$, and '$***$' for $p < 0.001$. Red lines indicate tPBM condition, while blue lines indicate sham. Error bars indicate the standard error of the mean of each case.

3.4 Discussion

3.4.1 tPBM-Induced Increases of Cerebral Δ[HbO] near the Stimulation Site

In our previously published work [201], we considered only eight channels in the prefrontal region and utilized the paired t-test at each of the eight channels without correction for multiple comparisons in statistical analysis. In this study, we re-analysed the signals of all 111 channels and applied a more rigorous statistical analysis, CBPT, to investigate crucial channels/regions possessing significant increases of Δ[HbO] induced by tPBM. This approach revealed significant clusters over the right frontopolar area near the stimulation site. The positive t-score values of the channels contributing to those clusters denoted a substantial increase of Δ[HbO] values during the active tPBM session compared to those of the sham session. Moreover, notable increases in Δ[HbO] occurred 4 mins after starting the laser stimulation and remained through the stimulation and post stimulation.

These findings were consistent with those reported previously [77, 78, 158, 195, 211]. For example, in [211], 1064-nm laser light was delivered to the forehead of healthy subjects and measured with a single-channel bbNIRS system to investigate corresponding changes in Δ[CCO], Δ[HbO], and Δ[HbT]. The authors observed significant increases in Δ[HbO] and Δ[CCO] near the stimulation location. Pruitt et al. [158] repeated the same experimental protocol with two age groups of young (mean of 26.7 years of age) and older subjects (mean of 68.2 years of age). Experimental results also revealed similar net increases in sham-controlled Δ[HbO]. Another study evidenced the augment of Δ[HbO] over the frontal area before and after forehead tPBM measured with a 20-channel fNIRS system [78]. In the meantime, the authors also reported tPBM-evoked improvement of cognitive performance.

It is worth noting that, although the skin temperature at the local stimulation site was slightly increased because of local light absorption [157, 210], the increase of Δ[HbO] observed in this study was not caused by the light-induced thermal effect. As reported in the previous study from our group [210], the changes in hemoglobin concentration induced by the heat stimulation were completely different from those provoked by tPBM. Specifically, thermal stimulation led to a decrease in Δ[HbO] during the stimulation period and a back-to-baseline state within 2 or 3 mins during the post-stimulation period. Other investigations on the tPBM-induced increase in brain temperature through a computational model [20] or magnetic resonance thermometry [45] also confirmed that there was no significant difference in temperature between tPBM and sham conditions. Furthermore, a recent study using EEG to investigate the effects of tPBM and thermal stimulation demonstrated that alterations of EEG power topography were significantly different between the two stimulations [213].

3.4.2 tPBM-Induced Increases in Δ[HbO] Power at Endogenic Oscillation

To the best of our knowledge, all tPBM-related studies utilized only time-domain or time-averaged analysis to investigate significant changes in hemodynamic and metabolic signals induced by tPBM [77, 78, 158, 195, 201, 211]. In this study, we employed a frequency-domain approach by taking the Welch method to investigate or analyze frequency-specific hemodynamic signals. The comparison of changes in frequency-dependent Δ[HbO] power between active tPBM and sham sessions revealed significant increase of Δ[HbO] power in the endogenic frequency band. Such results implied that tPBM impacted hemodynamic activities mainly on the endothelial cells of blood vessels at the endogenic oscillation.

3.4.3 Effects of tPBM on Frequency-Specific FC and Global Network Metrics

Instead of evaluating the effects of tPBM on FC within a broad frequency range (0-0.2 Hz) of Δ[HbO] as reported in [201], we calculated FC at three distinct frequency bands: endogenic (0.003-0.02 Hz), neurogenic (0.02-0.04 Hz), and myogenic (0.04-0.15 Hz), followed by comparisons of frequency-specific FC and global network metrics between three different time periods (i.e., pre, during, post) under either active or sham tPBM condition. To the best of our knowledge, this paper is the first one investigating the effects of tPBM on frequency-specific whole-head FC. Statistical analysis revealed distinct effects of tPBM on FC at different frequency bands.

3.4.3.1 Effects of tPBM on Endogenic Oscillation of Δ[HbO]

The observed significant enhancement in endogenic FC may be the results of changes in cerebral blood flow (CBF) and metabolism in the microvessels induced by tPBM [189]. Several existing studies observed an increase in CBF [77, 156, 199] and metabolism [128, 171] after tPBM. Prior studies suggested that an increase in the nitric oxide (NO) level induced by tPBM is responsible for the improved CBF [94, 109, 116]. Up-to-date research proved that PBM could be considered an exogenous stimulus that provoked an increase in NO production [14, 164]. NO, one of the vasoactive substances produced by the endothelium, significantly influences vascular tone [129]. NO is able to trigger vasodilation by activating guanylate cyclase to form cyclic guanine monophosphate (cGMP), which activates protein kinase G (PKG), resulting in decreased levels of Ca^{2+} concentration. The latter prevents myosin light-chain kinase from phosphorylating the myosin molecule, leading to the relaxation of the smooth muscle cells of blood vessels and lymphatic vessels [35, 129]. This vasodilation improves cerebral circulation and oxygenation, leading to enhanced FC after tPBM compared to pre-stimulation.

Specifically, the post-stimulation period exhibited boosted FC at the endogenic frequency between rPFC and most other regions of interest (ROIs) (Figures 3.6A and 3.7C). FP and DLPFC are associated with working memory, attention, and executive functions, while PMC, M1/S1, and Wernicke are related to motor control and speech fluency. The tPBM-evoked enhancements of FC in these ROIs support prior studies reporting improved executive function [18, 22], reaction time [15, 68, 202], attention [44, 83], and working memory [15, 18].

Furthermore, the strong modulation ability of tPBM on endogenic oscillation within cerebral hemodynamic ISO across the human whole head seen in this study is highly consistent with and well supported by another just-published article of our group [209]. The report was based on dual-channel, bbNIRS measurements taken from a completely different group of participants and performed by different operators. Similarly, tPBM was reported to significantly enhance the spectral amplitude of Δ[HbO] in the endogenic band by 13% near the tPBM site compared to the sham condition [209]. The excellent agreement in observing tPBM-evoked strong modulation in endogenic oscillation between two independent studies strengthens the underlying physiological expectation that tPBM facilitates (either directly or indirectly) an increase in NO, which will trigger alterations in endogenic oscillations and then vasodilation within a period of 1-4 minutes.

3.4.3.2 Effects of tPBM on Myogenic Oscillation of Δ[HbO]

We also observed significant improvement in myogenic FC following active tPBM (Figures 3.6B and 3.7E-F). Oscillations in this frequency band reflect the intrinsic activity of the vascular smooth muscle in response to changes in intravascular pressure [167]. The vascular smooth muscle may relax or contract in response to a decrease or increase of vascular pressure. In fact, the myogenic tone is strongly influenced by the release of vasoactive substances produced by endothelium [129]. As mentioned above, tPBM evokes an increase of NO, which activates guanylate cyclase to form cyclic guanine monophosphate (cGMP), leading to vasodilation [35, 129]. Similar to the endogenic frequency band, the Post-Pre pair of the myogenic frequency band exhibited significant improvement in FC among those ROIs involved closely in working memory, attention, executive functions, and motor control. Moreover, the observation that tPBM enabled to strongly modulate myogenic oscillation within cerebral hemodynamic ISO across the human whole head is also highly consistent with our recent article [209]. Accordingly, tPBM significantly enhanced the spectral amplitude of Δ[HbO] in the myogenic bands by 23% near the tPBM site compared to the sham condition [209].

Putting all the knowledge and recent findings together, our observations could be explained or interpreted as follows: tPBM started a cascade process by (1) first triggering the release of NO (besides photo-oxidation of CCO), (2) causing increases in endogenic oscillation and FC, (3) giving rise to the relaxation of the vascular smooth muscle, and thus (4) resulting in changes in myogenic oscillations as well as increases in myogenic FC. This cascade activity takes time in a few minutes for any significant change to be identifiable by physiological or objective measures, as we documented in our recent publications [208, 209]. Figure 3.9 summarizes two metabolic-primary hemodynamic events induced by tPBM. On the one hand, photo-oxidation of CCO enhances CCO redox metabolism and ATP synthesis, leading to a significant increase of Δ[HbO], as observed in Sections 3.3.1 and 3.3.2 and our previous studies [158, 211]. On the other hand, tPBM activates the release of NO [14, 164], which results in changes in endogenic and myogenic oscillations. Vasodilation caused by the increase of NO leads to an improvement of cerebral blood flow [94, 109, 116].

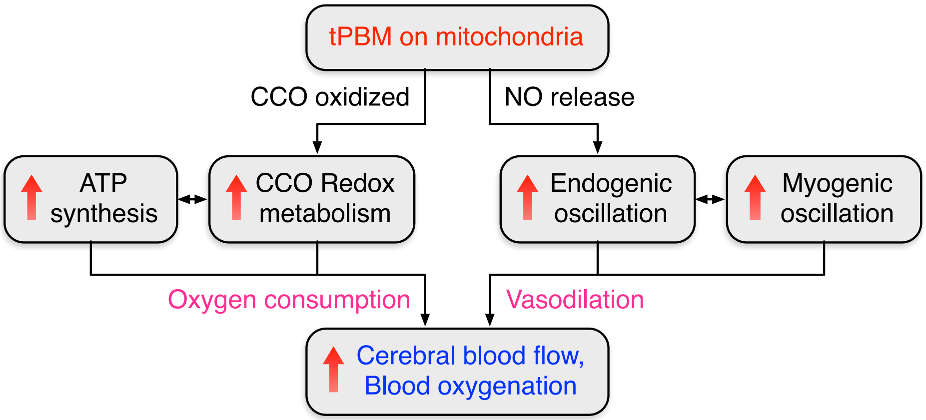

Figure 3.9: Flowchart to summarize two metabolic-primary hemodynamic events induced by tPBM.

Furthermore, GTA also revealed tPBM-evoked significant improvements in characteristic path length (L_p), global (E_g), and local efficiency (E_{loc}) metrics for the myogenic frequency band during the stimulation period (Figure 3.8). The characteristic path length, defined as the average of the shortest path lengths connecting each vertex to all other vertices, indicates how easily information is transported over the entire network [188]. Meanwhile, global efficiency measures the overall ability to transfer and process integrative information among channels or brain regions, and local efficiency indicates how efficiently the nodes communicate to others if one node is removed [74, 169]. Thus, shortened path lengths during the active tPBM session indicate that tPBM enabled to increase the transmitting speed for network information exchange. In the meantime, both global and local efficiencies of the topological network were improved perhaps partially because of shortened characteristic path length induced by tPBM.

3.4.3.3 Effects of tPBM on Neurogenic Oscillation of Δ[HbO]

For the neurogenic oscillation, paired t-tests with FDR correction reported that no significant difference was found in any FC line/edge between Post-Pre comparison or between Post-Stim comparison in either channel-wise or region-wise analysis. This observation implied that tPBM had little effect to alter or perturb the FC at neurogenic frequency range. A possible cause of this insignificant effect of tPBM on neurogenic oscillation is that neurogenic fluctuations reflect activities in large arteries and are independent of the endothelium [189, 190]. Accordingly, we can expect that tPBM would have minimal impact on this ISO component if the NIR light stimulated or modulated mainly the endogenic oscillation via NO release, one of the biological products by tPBM.

3.4.4 Limitations and Future Work

We identified two key weaknesses and proposed future work to overcome them.

3.4.4.1 Understanding inter-individual variability versus inter-experimental variability

In section 3.3.3, we compared changes in functional connectivity in two cases: (1) over time (pre vs. during vs. post) within each experimental session (active tPBM or sham) and (2) between experimental sessions (tPBM vs. sham). In case (1), the comparison was based on a single experiment setup with the main effect of active tPBM or sham over time, where the data deviation resulted from the inter-individual variability. On the other hand, in case (2), the comparison was made between two experimental sessions, in which the experimental setups of the same subject were not perfectly the same. Thus, in this case, the data deviation resulted from both inter-individual and inter-experimental variabilities [104]. Our results demonstrated clearly that inter-individual variability within one single experimental session (active tPBM or sham) was small enough to obtain significant effects of tPBM on endogenic and myogenic FC. On the other hand, the experimental variability between the tPBM and sham experimental sessions seemed too large, which shadowed the significance of tPBM between the two sessions. The experimental variability could be attributed to the complex setup of the whole-head fNIRS across subjects, which led to larger measurement inconsistency between the two sessions. To address this issue, we may reduce the number of channels and mark the probe locations with a 3D digitizer for improving the LABNIRS measurement reproducibility in future studies.

3.4.4.2 Potential contamination of extracranial layers to the interpreted signals

It is known that fNIRS signals measured on the scalp of human subjects include contributions from the extracranial layers (i.e., scalp and skull). To remove such potential contamination, extra optical channels of fNIRS with a short source-detector (S-D) separation (commonly ~0.8-1.2 cm) have been used for systemic noise removal in task-evoked hemodynamic studies [136, 196, 226, 228, 230], where a cortical region is functionally stimulated by a given task. However, most fNIRS-derived FC studies did not consider this confound effect until a recent report demonstrated that resting-state FC analysis with short S-D correction provides better accuracy than without correction [139].

We knowledge another weakness of this study is that the potential contribution from the extracranial layers to the hemodynamic results has not been considered. Under the tPBM scenario, both the superficial and cortical layers of tissue received optical stimulation. Thus, the conventional methods to remove superficial-layer effects are not appropriate in this study. However, even with room for improvement of accuracy, our reported results and conclusions in this study are in good agreement with a recent fMRI-driven report, showing that increases in brain-wide FC of the human brain were observed with connections involving the stimulated hemisphere having a significantly larger increase than those in the contralateral hemisphere [45]. Several independent studies also confirmed that tPBM enables to stimulate electrophysiological oscillation powers and enhance functional connectivity based on whole-head electroencephalogram [18, 59, 232].

In the field of non-invasive neuromodulation, this is the first mechanistic investigation with novel results on the tPBM-induced enhancement on frequency-specific hemodynamic power and FC in healthy humans across the whole head, which are in good agreement with other publications. In future studies, we plan to develop appropriate experimental setups and algorithms that will enable us to remove the confounding factor and thus to confirm/refine the results reported here.

3.5 Conclusions

In this study, we utilized a whole-head fNIRS system concurrently with 1064-nm tPBM delivered on the right prefrontal cortex to investigate the neurophysiological and/or hemodynamic responses to the light stimulation. First, we implemented the cluster-based permutation test on the tPBM-evoked, whole-head Δ[HbO] signals within the broad frequency range (0-0.2 Hz), which facilitated cortical mapping of cerebral regions of significant increases in Δ[HbO] signals over the right frontopolar area near the tPBM site, confirming the findings more rigorously. Next, we focused more on the intrinsic ISO components of the cerebral activity and analyzed different ISO-dependent metrics, including (1) Δ[HbO] spectral powers, (2) frequency-specific FC, and (3) frequency-specific global network metrics. Experimental results revealed that ISO components responded differently to tPBM. Briefly, tPBM significantly increased endogenic Δ[HbO] powers across the entire cortical region and enhanced topographical FC between the frontal stimulation site and the central as well as parietal regions. Furthermore, tPBM improved not only the myogenic FC across frontal-parietal cortical regions significantly but also several global network metrics substantially. Such strong effects of tPBM on both endogenic and myogenic hemodynamics may be attributed to tPBM-evoked NO release that would stimulate endogenic oscillations and vasodilation of blood vessels. These findings were consistent with the results reported recently and met the expectation that myogenic oscillation is highly associated with the endothelial activity. Finally, we proved our hypothesis of this study that tPBM would enhance FC at specific frequency bands (i.e., endogenic and myogenic oscillations), resulting from mitochondrial absorption of light given by tPBM.

Chapter 4

Influence of the Signal-to-Noise Ratio on Variance of Chromophore Concentration Quantification in Broadband Near-Infrared Spectroscopy

Nghi Cong Dung Truong, Sadra Shahdadian, Shu Kang, Xinlong Wang, and Hanli Liu

(This chapter is a manuscript that has been accepted for publication in Frontiers in Photonics)

4.1 Introduction

Near-infrared spectroscopy (NIRS) [21, 23, 160, 176, 179] has been considered an effective and non-invasive tool for functional imaging and diagnostics in medical applications. Besides the conventional NIR window from 650 to 950 nm [205], the advancement of new technology made other NIR windows within the 1000 to 2500 nm wavelength range become possible [7, 180, 207]. These NIR windows have gained much attention recently because of their capacity to obtain greater imaging and sensing depth, and thus capable of investigating both soft tissue constituents (such as with high lipid content or cancers) and hard tissue constituents (such as bones) [179, 187].

In this study, we focus on the conventional NIRS with the wavelength range from 650 to 950 nm, which facilitates quantitative changes of the hemodynamic [24] and metabolic state of various tissue types, such as the breast [33, 88], muscle [52, 212], or brain [158, 185, 195, 205, 209, 211]. In this spectral range, the three main chromophores of interest in most NIRS-based studies are oxyhemoglobin (HbO), deoxyhemoglobin (HHb), and cytochrome-c-oxidase (CCO) [13, 75, 101, 102, 209, 211, 212]. Numerous studies have revealed the potential use of NIRS in a wide range of clinical applications, including neuromonitoring [106, 150], metabolic state observation [48, 72], or cancer detection [33, 88, 132].

The modified Beer-Lambert law [115, 174] is mostly employed as the mathematical fundamental of a NIRS system to quantify changes in chromophore concentrations, namely, changes of oxy-hemoglobin (Δ[HbO]), deoxy-hemoglobin (Δ[HHb]), oxidized cytochrome-c- oxidase (Δ[oxCCO]). Theoretically, the minimum number of wavelengths required for the calculation of chromophore concentration changes must be minimally equal to the number of chromophores. When Δ[oxCCO] is the parameter of interest, however, such an approach is extremely sensitive to the system noise and may lead to inaccurate quantification because of its low concentration in tissue with respect to Δ[HbO] and Δ[HHb]. Thus, an adequate signal-to-noise ratio (SNR) of a NIRS measurement becomes a key determinant to judge or predict accuracy of experimental results of chromophore concentration changes. Broadband NIRS (bbNIRS) [13, 75, 101, 102], which provides a full or broad wavelength range of measurement, is expected to alleviate the influence of system noise and offer more reliable quantification results. Several studies have also been carried out to identify optimal wavelength combinations in order to minimize the measurement redundancy but still ensure the accuracy of the quantification results [9, 216].

Since Δ[HbO], Δ[HHb], and Δ[oxCCO] must be inferred from the optical densities measured at multiple wavelengths, measurement variations caused by the system's thermal or electrical noise, drifts, and disturbance will lead to variability in the respective quantities. To our knowledge, very few studies have addressed such a problem. Most existing works have focused on the effect of extinction coefficients, optical pathlengths, or wavelength combinations on the accuracy of estimated changes of chromophore concentrations. Kim and Liu [97] proved that small variations in hemoglobin extinction coefficients would lead to large variations in quantifications of hemoglobin concentration changes. Funane et al. [57] investigated the relationship between the errors in calculating Δ[HbO] and Δ[HHb] versus different wavelength selections or combinations. Recently, Sudakou et al. [192] presented an error propagation analysis method to estimate the deviations of the recovered tissue constituent concentrations using a time-resolved NIRS.

In this study, we sought to investigate the influence of SNR of a bbNIRS system on quantifications of Δ[HbO], Δ[HHb], and Δ[oxCCO]. Practically, all measured data are not noise-free; they must consist of natural variability or uncertainty from the measurement system. The accuracy of the results derived from these measurements will depend on the measurement errors or SNR [19, 64]. In other words, measurement variances or errors will propagate to the quantified results. Note that the objective of this study was to quantify the SNR-derived variance of Δ[HbO], Δ[HHb], and Δ[oxCCO] caused only by the noise of the bbNIRS instruments/devices. Other parameters, such as the extinction coefficients and the optical pathlengths, are not the concern of variables in this study. Being aware of how much system noise propagates into the calculated chromophore concentration changes is essential when considering a bbNIRS system. Since the system SNR can be calculated easily throughout multiple baseline measurements, we can estimate or predict the SNR-derived variance of Δ[HbO], Δ[HHb], and Δ[oxCCO] based on the results of error propagation analysis. Consequently, one may want to improve the SNR of the bbNIRS system to lessen the uncertainties of calculated chromophore concentration changes by considering warming up the system to reach a stable state, optimizing the light exposure time, or selecting an optimal wavelength range.

Specifically, we performed the error propagation analysis for bbNIRS to calculate variances of Δ[HbO], Δ[HHb], and Δ[oxCCO] induced by the measurement system's noise. We considered only the case where the number of wavelengths is larger than the number of chromophores. Thus, the chromophore concentration changes were estimated by fitting the model to the measured data using the least-squares method [13, 75, 101, 102]. As a consequence, the analytical expressions of the error propagation in estimating Δ[HbO], Δ[HHb], and Δ[oxCCO] were derived directly from the best-fit model. In order to compare the analytical results with experimental results, we first carried out two real bbNIRS experiments, namely, (1) one taken from a solid tissue phantom using two spectrometers concurrently and (2) the other from the human forearm at resting state. Then, a Monte Carlo (MC) simulation framework that permits to replicate or simulate the measurement of a bbNIRS system was conducted. To demonstrate good consistency of influence of SNR on chromophore concentrations among all three cases, the theoretical quantitation of the SNR-derived variances of Δ[HbO], Δ[HHb], and Δ[oxCCO] were compared with the respective variances calculated directly from the measured and simulated data. Finally, we also performed analyses to assess optimal selections and ranges of wavelengths for bbNIRS to minimize variances of Δ[HbO], Δ[HHb], and Δ[oxCCO].

4.2 Methodology

4.2.1 Modified Beer-Lambert Law

It is known that changes in chromophore concentrations are calculated based on the modified Beer-Lambert law [99, 115, 174]:

$$\Delta \mathrm{OD}(\lambda_i) = -\log_{10}\left[\frac{I(\lambda_i)}{I_0(\lambda_i)}\right] = \sum_{k=1}^{N} \epsilon_{\mathrm{C}_k}(\lambda_i) \times \Delta[\mathrm{C}_k] \times L(\lambda_i) \tag{4.1}$$

where $\Delta\mathrm{OD}(\lambda_i)$ is the change in optical density at wavelength λ_i, I_0 and I are the detected light intensities of the baseline and transient conditions, respectively. $\epsilon_{\mathrm{C}_k}(\lambda_i)$ is the extinction coefficient of the k-th chromophore at wavelength λ_i, $\Delta[\mathrm{C}_k]$ is the change of the k-th chromophore concentration, and $L(\lambda_i)$ is the optical pathlength of wavelength λ_i. Such optical pathlength is estimated as $L(\lambda_i) = r \times \mathrm{DPF}(\lambda_i)$, where r is the source-detector separation distance, and $\mathrm{DPF}(\lambda_i)$ is the differential path-length factor, which is introduced to consider light scattering effects in Beer-Lambert's law.

If the number of chromophores and wavelengths are equal, the chromophore concentration changes are calculated by simultaneously solving the number of equations (i.e., Eq. (4.1) with respective parameters). If the wavelength number is larger than the number of chromophores, the chromophore concentration changes are estimated by fitting the model (i.e., Eq. (4.1)) to measured data using the least-squares method [13, 75, 101, 102]. In this study, we consider the general case using multiple wavelengths to estimate Δ[HbO], Δ[HHb], and Δ[oxCCO]. In such a case, the modified Beer-Lambert law, namely, Eq. (4.1), can be rewritten as follows:

$$\begin{bmatrix} \Delta\mathrm{OD}(\lambda_1) \\ \Delta\mathrm{OD}(\lambda_2) \\ \vdots \\ \Delta\mathrm{OD}(\lambda_m) \end{bmatrix} = \begin{bmatrix} L(\lambda_1)\epsilon_{\mathrm{HbO}}(\lambda_1) & L(\lambda_1)\epsilon_{\mathrm{HHb}}(\lambda_1) & L(\lambda_1)\epsilon_{\mathrm{diffCCO}}(\lambda_1) \\ L(\lambda_2)\epsilon_{\mathrm{HbO}}(\lambda_2) & L(\lambda_2)\epsilon_{\mathrm{HHb}}(\lambda_2) & L(\lambda_2)\epsilon_{\mathrm{diffCCO}}(\lambda_2) \\ \vdots & \vdots & \vdots \\ L(\lambda_m)\epsilon_{\mathrm{HbO}}(\lambda_m) & L(\lambda_m)\epsilon_{\mathrm{HHb}}(\lambda_m) & L(\lambda_m)\epsilon_{\mathrm{diffCCO}}(\lambda_m) \end{bmatrix} \begin{bmatrix} \Delta[\mathrm{HbO}] \\ \Delta[\mathrm{HHb}] \\ \Delta[\mathrm{oxCCO}] \end{bmatrix} \tag{4.2}$$

where m is the total number of wavelengths, $\epsilon_{\mathrm{HbO}}(\lambda_i)$, $\epsilon_{\mathrm{HHb}}(\lambda_i)$, and $\epsilon_{\mathrm{diffCCO}}(\lambda_i)$ are the extinction coefficients of HbO, HHb, and oxidized-reduced difference of CCO [11] at wavelength λ_i, respectively.

4.2.2 Error Propagation from Measurement Noise to Δ[HbO], Δ[HHb], and Δ[oxCCO]

For simplification, let $\mathbf{C} = \begin{bmatrix} L(\lambda_1)\epsilon_{\text{HbO}}(\lambda_1) & L(\lambda_1)\epsilon_{\text{HHb}}(\lambda_1) & L(\lambda_1)\epsilon_{\text{diffCCO}}(\lambda_1) \\ L(\lambda_2)\epsilon_{\text{HbO}}(\lambda_2) & L(\lambda_2)\epsilon_{\text{HHb}}(\lambda_2) & L(\lambda_2)\epsilon_{\text{diffCCO}}(\lambda_2) \\ \vdots & \vdots & \vdots \\ L(\lambda_m)\epsilon_{\text{HbO}}(\lambda_m) & L(\lambda_m)\epsilon_{\text{HHb}}(\lambda_m) & L(\lambda_m)\epsilon_{\text{diffCCO}}(\lambda_m) \end{bmatrix}$,
$\mathbf{y} = \begin{bmatrix} \Delta\text{OD}(\lambda_1) \\ \Delta\text{OD}(\lambda_2) \\ \vdots \\ \Delta\text{OD}(\lambda_m) \end{bmatrix}$, and $\mathbf{a} = \begin{bmatrix} \Delta[\text{HbO}] \\ \Delta[\text{HHb}] \\ \Delta[\text{oxCCO}] \end{bmatrix}$. Equation (4.2) is equivalent to:

$$\mathbf{y} = \mathbf{Ca} \tag{4.3}$$

Δ[HbO], Δ[HHb] and Δ[oxCCO] in equation (4.2) are typically estimated using the least-squares fitting method. The principle is to fit the results from the linear model $\hat{\mathbf{y}} = \mathbf{Ca}$ to the measured data $\mathbf{y} = [\Delta\text{OD}(\lambda_1) \cdots \Delta\text{OD}(\lambda_m)]^T$ as closely as possible. Such a best-fit minimizes the chi-squared optimization function defined as follows:

$$\begin{aligned} \chi^2(\mathbf{a}) &= \sum_{i=1}^{m} \frac{[\hat{y}_i - y_i]^2}{\sigma_{y_i}^2} = [\mathbf{y} - \mathbf{y}]^T \mathbf{V}_{\mathbf{y}}^{-1} [\mathbf{y} - \mathbf{y}] = \{\mathbf{Ca} - \mathbf{y}\}^T \mathbf{V}_{\mathbf{y}}^{-1} \{\mathbf{Ca} - \mathbf{y}\} \\ &= \mathbf{a}^T \mathbf{C}^T \mathbf{V}_{\mathbf{y}}^{-1} \mathbf{Ca} - 2\mathbf{a}^T \mathbf{C}^T \mathbf{V}_{\mathbf{y}}^{-1} \mathbf{y} + \mathbf{y}^T \mathbf{V}_{\mathbf{y}}^{-1} \mathbf{y} \end{aligned} \tag{4.4}$$

where $\mathbf{V}_{\mathbf{y}} = \begin{bmatrix} \sigma_{y_1}^2 & 0 & \cdots & 0 \\ 0 & \sigma_{y_2}^2 & \cdots & 0 \\ \vdots & \vdots & \ddots & \vdots \\ 0 & 0 & \cdots & \sigma_{y_m}^2 \end{bmatrix}$ is the diagonal matrix of variances of $\mathbf{y}$ and $\sigma_{y_i}^2$ is the variance of the measurement y_i.

The χ^2 optimization function is minimized with respect to the parameters $\mathbf{a}$ by solving the equation of $\left.\frac{\partial \chi^2}{\partial \mathbf{a}}\right|_{\mathbf{a}=\hat{\mathbf{a}}} = 0$, which leads to the linear least-square estimate of the parameters $\mathbf{a}$ as follows:

$$\hat{\mathbf{a}} = [\mathbf{C}^T \mathbf{V}_{\mathbf{y}}^{-1} \mathbf{C}]^{-1} \mathbf{C}^T \mathbf{V}_{\mathbf{y}}^{-1} \mathbf{y} \tag{4.5}$$

Note that the linear least square estimate of Δ[HbO], Δ[HHb] and Δ[oxCCO] defined in equation (4.5) is a function of the measured ΔOD, the ΔOD covariance matrix, the extinction coefficients, and the optical pathlength. As mentioned above, we consider the error propagation caused only by the noise from instruments. Thus, matrix **C**, which includes the extinction coefficients and the optical pathlengths at all wavelengths, is considered a constant matrix. The covariance matrix of the estimates of Δ[HbO], Δ[HHb] and Δ[oxCCO] is calculated as follows:

$$\mathbf{V}_{\hat{\mathbf{a}}} = \left[\frac{\partial \hat{\mathbf{a}}}{\partial \mathbf{y}}\right] \mathbf{V}_{\mathbf{y}} \left[\frac{\partial \hat{\mathbf{a}}}{\partial \mathbf{y}}\right]^T = [\mathbf{C}^T \mathbf{V}_{\mathbf{y}}^{-1} \mathbf{C}]^{-1} \tag{4.6}$$

By substituting the matrices **C** and $\mathbf{V}_{\mathbf{y}}$ in equation (4.6) with the original definitions, the covariance matrix of the estimated Δ[HbO], Δ[HHb] and Δ[oxCCO] can be rewritten as:

$$\mathbf{V}_{\hat{\mathbf{a}}} = \begin{bmatrix} \sum\limits_{i=1}^{m} \frac{L^2(\lambda_i)\epsilon_{\mathrm{HbO}}^2(\lambda_i)}{\sigma_{\Delta OD(\lambda_i)}^2} & \sum\limits_{i=1}^{m} \frac{L^2(\lambda_i)\epsilon_{\mathrm{HbO}}(\lambda_i)\epsilon_{\mathrm{HHb}}(\lambda_i)}{\sigma_{\Delta OD(\lambda_i)}^2} & \sum\limits_{i=1}^{m} \frac{L^2(\lambda_i)\epsilon_{\mathrm{HbO}}(\lambda_i)\epsilon_{\mathrm{diffCCO}}(\lambda_i)}{\sigma_{\Delta OD(\lambda_i)}^2} \\ \sum\limits_{i=1}^{m} \frac{L^2(\lambda_i)\epsilon_{\mathrm{HbO}}(\lambda_i)\epsilon_{\mathrm{HHb}}(\lambda_i)}{\sigma_{\Delta OD(\lambda_i)}^2} & \sum\limits_{i=1}^{m} \frac{L^2(\lambda_i)\epsilon_{\mathrm{HHb}}^2(\lambda_i)}{\sigma_{\Delta OD(\lambda_i)}^2} & \sum\limits_{i=1}^{m} \frac{L^2(\lambda_i)\epsilon_{\mathrm{HHb}}(\lambda_i)\epsilon_{\mathrm{diffCCO}}(\lambda_i)}{\sigma_{\Delta OD(\lambda_i)}^2} \\ \sum\limits_{i=1}^{m} \frac{L^2(\lambda_i)\epsilon_{\mathrm{HbO}}(\lambda_i)\epsilon_{\mathrm{diffCCO}}(\lambda_i)}{\sigma_{\Delta OD(\lambda_i)}^2} & \sum\limits_{i=1}^{m} \frac{L^2(\lambda_i)\epsilon_{\mathrm{HHb}}(\lambda_i)\epsilon_{\mathrm{diffCCO}}(\lambda_i)}{\sigma_{\Delta OD(\lambda_i)}^2} & \sum\limits_{i=1}^{m} \frac{L^2(\lambda_i)\epsilon_{\mathrm{diffCCO}}^2(\lambda_i)}{\sigma_{\Delta OD(\lambda_i)}^2} \end{bmatrix}^{-1} \tag{4.7}$$

For simplification, let $\xi_{\mathrm{HbO}}(\lambda_i) = L(\lambda_i)\epsilon_{\mathrm{HbO}}(\lambda_i)$, $\xi_{\mathrm{HHb}}(\lambda_i) = L(\lambda_i)\epsilon_{\mathrm{HHb}}(\lambda_i)$, and $\xi_{\mathrm{diffCCO}}(\lambda_i) =$

$L(\lambda_i)\epsilon_{\text{diffCCO}}(\lambda_i)$, the covariance matrix $\mathbf{V}_{\hat{\mathbf{a}}}$ can be simplified as follows:

$$\mathbf{V}_{\hat{\mathbf{a}}} = \begin{bmatrix} \sum_{i=1}^{m} \frac{\xi_{\text{HbO}}^2(\lambda_i)}{\sigma^2_{\Delta OD(\lambda_i)}} & \sum_{i=1}^{m} \frac{\xi_{\text{HbO}}(\lambda_i)\xi_{\text{HHb}}(\lambda_i)}{\sigma^2_{\Delta OD(\lambda_i)}} & \sum_{i=1}^{m} \frac{\xi_{\text{HbO}}(\lambda_i)\xi_{\text{diffCCO}}(\lambda_i)}{\sigma^2_{\Delta OD(\lambda_i)}} \\ \sum_{i=1}^{m} \frac{\xi_{\text{HbO}}(\lambda_i)\xi_{\text{HHb}}(\lambda_i)}{\sigma^2_{\Delta OD(\lambda_i)}} & \sum_{i=1}^{m} \frac{\xi_{\text{HHb}}^2(\lambda_i)}{\sigma^2_{\Delta OD(\lambda_i)}} & \sum_{i=1}^{m} \frac{\xi_{\text{HHb}}(\lambda_i)\xi_{\text{diffCCO}}(\lambda_i)}{\sigma^2_{\Delta OD(\lambda_i)}} \\ \sum_{i=1}^{m} \frac{\xi_{\text{HbO}}(\lambda_i)\xi_{\text{diffCCO}}(\lambda_i)}{\sigma^2_{\Delta OD(\lambda_i)}} & \sum_{i=1}^{m} \frac{\xi_{\text{HHb}}(\lambda_i)\xi_{\text{diffCCO}}(\lambda_i)}{\sigma^2_{\Delta OD(\lambda_i)}} & \sum_{i=1}^{m} \frac{\xi_{\text{diffCCO}}^2(\lambda_i)}{\sigma^2_{\Delta OD(\lambda_i)}} \end{bmatrix}^{-1} \tag{4.8}$$

This covariance matrix is known as the error propagation matrix, which indicates how measurement errors in ΔOD, described by $\sigma^2_{\Delta OD(\lambda_i)}$, propagate to the estimated Δ[HbO], Δ[HHb] and Δ[oxCCO]. Based on the definition of $\Delta\text{OD}(\lambda_i)$ in Eq. (4.1) (i.e., $\Delta\text{OD}(\lambda_i) = -\log_{10}\left[\frac{I(\lambda_i)}{I_0(\lambda_i)}\right]$), the variance of ΔOD is computed as:

$$\sigma^2_{\Delta\text{OD}(\lambda_i)} = \frac{1}{(\ln 10)^2}\left(\frac{\sigma^2_{I_0(\lambda_i)}}{[I_0(\lambda_i)]^2} + \frac{\sigma^2_{I(\lambda_i)}}{[I(\lambda_i)]^2}\right) \tag{4.9}$$

If multiple measurements are repeated for both baseline and transient instant, the detected light intensities I_0 and I can be replaced by the mean values of all measurements' detected light intensities. Mathematically, the fraction $\bar{I}^2/\sigma_I^2$ is equivalent to the SNR of the measurement system. Furthermore, assuming that the measurement system has consistent SNR for both baseline and transient instant measurements, Eq. (4.9) can be rewritten as:

$$\sigma^2_{\Delta\text{OD}(\lambda_i)} = \frac{1}{(\ln 10)^2}\frac{2}{\text{SNR}(\lambda_i)} \tag{4.10}$$

Substituting Eq. (4.10) into Eq. (4.8), we obtain the error propagation matrix calculated from the SNR of the measurement system.

$$\mathbf{V}_{\hat{\mathbf{a}}} = \frac{2}{(\ln 10)^2} \begin{bmatrix} \sum_{i=1}^{m} \xi_{\mathrm{HbO}}^2(\lambda_i)\mathrm{SNR}(\lambda_i) & \sum_{i=1}^{m} \xi_{\mathrm{HbO}}(\lambda_i)\xi_{\mathrm{HHb}}(\lambda_i)\mathrm{SNR}(\lambda_i) & \sum_{i=1}^{m} \xi_{\mathrm{HbO}}(\lambda_i)\xi_{\mathrm{diffCCO}}(\lambda_i)\mathrm{SNR}(\lambda_i) \\ \sum_{i=1}^{m} \xi_{\mathrm{HbO}}(\lambda_i)\xi_{\mathrm{HHb}}(\lambda_i)\mathrm{SNR}(\lambda_i) & \sum_{i=1}^{m} \xi_{\mathrm{HHb}}^2(\lambda_i)\mathrm{SNR}(\lambda_i) & \sum_{i=1}^{m} \xi_{\mathrm{HHb}}(\lambda_i)\xi_{\mathrm{diffCCO}}(\lambda_i)\mathrm{SNR}(\lambda_i) \\ \sum_{i=1}^{m} \xi_{\mathrm{HbO}}(\lambda_i)\xi_{\mathrm{diffCCO}}(\lambda_i)\mathrm{SNR}(\lambda_i) & \sum_{i=1}^{m} \xi_{\mathrm{HHb}}(\lambda_i)\xi_{\mathrm{diffCCO}}(\lambda_i)\mathrm{SNR}(\lambda_i) & \sum_{i=1}^{m} \xi_{\mathrm{diffCCO}}^2(\lambda_i)\mathrm{SNR}(\lambda_i) \end{bmatrix}^{-1} \tag{4.11}$$

The square root of the diagonal of this covariance matrix corresponds to the standard deviation of Δ[HbO], Δ[HHb] and Δ[oxCCO], which indicates the uncertainties of the estimated chromophore concentration changes caused by the measurement system noise. We note the standard deviation of the chromophore concentration changes derived by the proposed error propagation analysis as $\sigma^T_{\Delta[\mathrm{C}_k]}$, where $[\mathrm{C}_k]$ denotes the chromophore concentration that includes [HbO], [HHb] and [oxCCO]. The superscript T indicates that $\sigma^T_{\Delta[\mathrm{C}_k]}$ was derived by the theoretical analysis (Eq. (4.11)). In the later part, we would also calculate the standard deviation of $\Delta[\mathrm{C}_k]$ from the measurement or simulation data and denote it as $\sigma^M_{\Delta[\mathrm{C}_k]}$ to distinguish it from $\sigma^T_{\Delta[\mathrm{C}_k]}$ estimated from the error propagation analysis.

We also sought to expand the matrix inverse in Eq. (4.11). For simplification, assuming that

SNR is a constant for all wavelength. Eq. (4.11) can be rewritten as:

$$\mathbf{V}_{\hat{\mathbf{a}}} = \frac{2}{(\ln 10)^2\,\mathrm{SNR}} \begin{bmatrix} \sum_{i=1}^{m} \xi^2_{\mathrm{HbO}}(\lambda_i) & \sum_{i=1}^{m} \xi_{\mathrm{HbO}}(\lambda_i)\xi_{\mathrm{HHb}}(\lambda_i) & \sum_{i=1}^{m} \xi_{\mathrm{HbO}}(\lambda_i)\xi_{\mathrm{diffCCO}}(\lambda_i) \\ \sum_{i=1}^{m} \xi_{\mathrm{HbO}}(\lambda_i)\xi_{\mathrm{HHb}}(\lambda_i) & \sum_{i=1}^{m} \xi^2_{\mathrm{HHb}}(\lambda_i) & \sum_{i=1}^{m} \xi_{\mathrm{HHb}}(\lambda_i)\xi_{\mathrm{diffCCO}}(\lambda_i) \\ \sum_{i=1}^{m} \xi_{\mathrm{HbO}}(\lambda_i)\xi_{\mathrm{diffCCO}}(\lambda_i) & \sum_{i=1}^{m} \xi_{\mathrm{HHb}}(\lambda_i)\xi_{\mathrm{diffCCO}}(\lambda_i) & \sum_{i=1}^{m} \xi^2_{\mathrm{diffCCO}}(\lambda_i) \end{bmatrix}^{-1} \tag{4.12}$$

By expanding the matrix inverse, $\mathbf{V}_{\hat{\mathbf{a}}}$ can be expressed as $\mathbf{V}_{\hat{\mathbf{a}}} = \frac{2}{(\ln 10)^2\,\mathrm{SNR}} \cdot \frac{1}{DET} \cdot B$, where

$$\begin{aligned} DET \;=\; & \sum_{i=1}^{m} \xi^2_{\mathrm{HbO}}(\lambda_i) \left[\sum_{i=1}^{m} \xi^2_{\mathrm{HHb}}(\lambda_i) \sum_{i=1}^{m} \xi^2_{\mathrm{diffCCO}}(\lambda_i) - \left(\sum_{i=1}^{m} \xi_{\mathrm{HHb}}(\lambda_i)\xi_{\mathrm{diffCCO}}(\lambda_i) \right)^2 \right] \\ & - \sum_{i=1}^{m} \xi_{\mathrm{HbO}}(\lambda_i)\xi_{\mathrm{HHb}}(\lambda_i) \left[\sum_{i=1}^{m} \xi_{\mathrm{HbO}}(\lambda_i)\xi_{\mathrm{HHb}}(\lambda_i) \sum_{i=1}^{m} \xi^2_{\mathrm{diffCCO}}(\lambda_i) - \sum_{i=1}^{m} \xi_{\mathrm{HbO}}(\lambda_i)\xi_{\mathrm{diffCCO}}(\lambda_i) \sum_{i=1}^{m} \xi_{\mathrm{HHb}}(\lambda_i)\xi_{\mathrm{diffCCO}}(\lambda_i) \right] \\ & + \sum_{i=1}^{m} \xi_{\mathrm{HbO}}(\lambda_i)\xi_{\mathrm{diffCCO}}(\lambda_i) \left[\sum_{i=1}^{m} \xi_{\mathrm{HbO}}(\lambda_i)\xi_{\mathrm{HHb}}(\lambda_i) \sum_{i=1}^{m} \xi_{\mathrm{HHb}}(\lambda_i)\xi_{\mathrm{diffCCO}}(\lambda_i) - \sum_{i=1}^{m} \xi_{\mathrm{HbO}}(\lambda_i)\xi_{\mathrm{diffCCO}}(\lambda_i) \sum_{i=1}^{m} \xi^2_{\mathrm{HHb}}(\lambda_i) \right] \end{aligned} \tag{4.13}$$

and

$$\mathrm{diag}\,(B) = \begin{bmatrix} \sum_{i=1}^{m} \xi^2_{\mathrm{HHb}}(\lambda_i) \sum_{i=1}^{m} \xi^2_{\mathrm{diffCCO}}(\lambda_i) - \left(\sum_{i=1}^{m} \xi_{\mathrm{HHb}}(\lambda_i)\xi_{\mathrm{diffCCO}}(\lambda_i) \right)^2 \\ \sum_{i=1}^{m} \xi^2_{\mathrm{HbO}}(\lambda_i) \sum_{i=1}^{m} \xi^2_{\mathrm{diffCCO}}(\lambda_i) - \left(\sum_{i=1}^{m} \xi_{\mathrm{HbO}}(\lambda_i)\xi_{\mathrm{diffCCO}}(\lambda_i) \right)^2 \\ \sum_{i=1}^{m} \xi^2_{\mathrm{HbO}}(\lambda_i) \sum_{i=1}^{m} \xi^2_{\mathrm{HHb}}(\lambda_i) - \left(\sum_{i=1}^{m} \xi_{\mathrm{HbO}}(\lambda_i)\xi_{\mathrm{HHb}}(\lambda_i) \right)^2 \end{bmatrix} \tag{4.14}$$

Finally, the variances of Δ[HbO], Δ[HHb] and Δ[oxCCO] are calculated as:

$$[\sigma^T_{\Delta[\text{HbO}]}]^2 = \frac{2}{(\ln 10)^2\,\text{SNR}}\frac{1}{DET}\left[\sum_{i=1}^{m}\xi^2_{\text{HHb}}(\lambda_i)\sum_{i=1}^{m}\xi^2_{\text{diffCCO}}(\lambda_i) - \left(\sum_{i=1}^{m}\xi_{\text{HHb}}(\lambda_i)\xi_{\text{diffCCO}}(\lambda_i)\right)^2\right] \tag{4.15}$$

$$[\sigma^T_{\Delta[\text{HHb}]}]^2 = \frac{2}{(\ln 10)^2\,\text{SNR}}\frac{1}{DET}\left[\sum_{i=1}^{m}\xi^2_{\text{HbO}}(\lambda_i)\sum_{i=1}^{m}\xi^2_{\text{diffCCO}}(\lambda_i) - \left(\sum_{i=1}^{m}\xi_{\text{HbO}}(\lambda_i)\xi_{\text{diffCCO}}(\lambda_i)\right)^2\right] \tag{4.16}$$

$$[\sigma^T_{\Delta[\text{diffCCO}]}]^2 = \frac{2}{(\ln 10)^2\,\text{SNR}}\frac{1}{DET}\left[\sum_{i=1}^{m}\xi^2_{\text{HbO}}(\lambda_i)\sum_{i=1}^{m}\xi^2_{\text{HHb}}(\lambda_i) - \left(\sum_{i=1}^{m}\xi_{\text{HbO}}(\lambda_i)\xi_{\text{HHb}}(\lambda_i)\right)^2\right] \tag{4.17}$$

4.2.3 Actual Measurements from a Solid Phantom and the Human Arm Using bbNIRS

In order to evaluate how well the derived error propagation calculations matched with the real bbNIRS data, we first conducted actual measurements from a solid phantom using two separate bbNIRS spectrometers combined with one light source, as shown in Figure 4.1A. The two spectrometers utilized (1) a two-dimensional CCD spectrograph (Teledyne Princeton Instrument, 3660 Quakerbridge Road Trenton, NJ 08619 USA) and (2) a back-thinned cool-down CCD spectrometer (QE-Pro, Ocean Optics Inc). A tungsten halogen lamp (Model 3900, Illumination Technologies Inc., East Syracuse, NY) covering 400-1500 nm light was used as the light source. We used the solid phantom provided by ISS (ISS Inc., Champaign, IL, USA) with the absorption coefficient μ_a of 0.155 cm^{-1} at 690 nm and 0.15 cm^{-1} at 830 nm. Three fiber bundles were used, one for the light delivery and two for light collection from the solid phantom. The distance between each detection bundle to the source bundle was 3 cm. The bbNIRS data were collected concurrently by these two spectrometers to ensure the identical environmental condition. The exposure time of both spectrometers was set to 1 sec, and the data were collected continuously over 30 min, resulting in a total of 1800 data points for each spectrometer. We repeated the measurements seven times on different days to ensure the arbitrary nature of the data collection.

The second experiment was conducted on the human forearm under the resting state with no stimulation. The experimental protocol was approved by the Institutional Review Board (IRB) of the University of Texas at Arlington. Two healthy adults participated in this experiment. Each subject attended eight measurement sessions on different days, which led to $n = 16$ measurements. Informed consent was acquired prior to all measurements.

The experimental setup was illustrated in Figure 4.1B. The bbNIRS system consisted of a tungsten halogen lamp (Model 3900, Illumination Technologies Inc., East Syracuse, NY) and a CCD spectrometer (QE-Pro, Ocean Optics Inc), both of which were used in the phantom measurements. A flexible probe holder was used to firmly hold the two optical fiber bundles on the subject's forearm. An optical shutter was also employed to switch on the light only during the exposure time to minimize the tissue heating effect from the broadband light source. An experiment lasted 15 min with a 5-sec single light-exposure/data-acquisition time per minute, giving rise to 16 spectra per measurement.

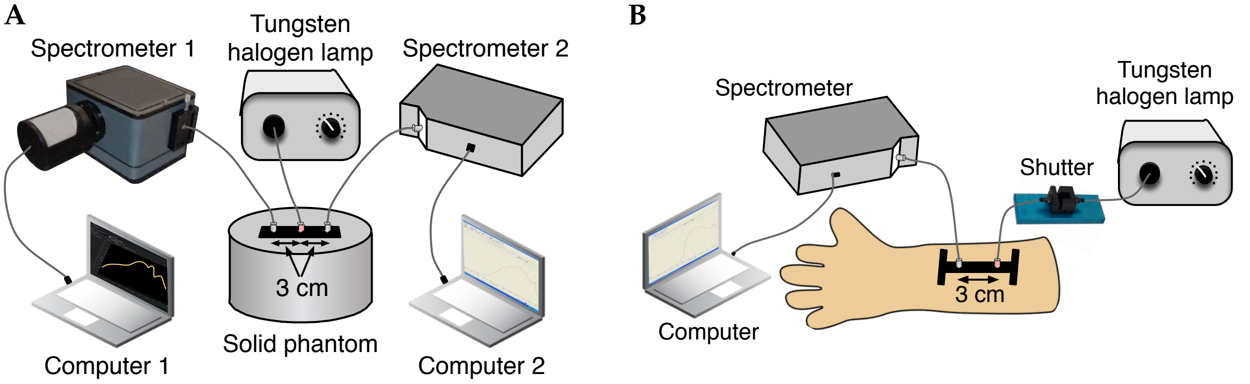

Figure 4.1: Experimental setup for the bbNIRS measurement taken from (A) a tissue phantom and (B) the human forearm. (**A**) Light source-detector configuration for the phantom measurement. (**B**) Light source-detector configuration for the human arm measurement.

4.2.4 Monte Carlo Simulations

We also conducted a Monte Carlo (MC) framework that simulated bbNIRS data of the hemodynamic and metabolic states of the exposed tissue. Two physiological conditions were defined within the MC simulation: (1) a baseline state corresponding to the normal resting state of the tissue and (2) a stimulated state where oxygenation and metabolism improved notably. We employed MCmatlab [123], an open-source MC program for light propagation in three-dimensional (3-D) media.

Specifically, a ($600 \times 600 \times 300$) voxel model corresponding to a ($4 \times 4 \times 2$ cm) 3-D volume was first defined as the simulation geometry. The medium that replicates general tissue was considered to be made of water, fat, blood with different oxygen saturation levels, and concentrations of oxCCO and reduced CCO (redCCO). The composition and the optical properties of the medium were defined based on the properties of biological tissues reported in [84, 85]. The scattering coefficient $\mu_s(\lambda)$ was considered to be dependent only on the wavelength λ, while the absorption coefficient $\mu_a(\lambda)$ was estimated as the sum of absorption coefficients of all major chromophores composing the medium [11, 85]. Table 4.1 summarizes the simulation medium composition of two physiological conditions, while Figure 4.2 depicts the corresponding absorption coefficient $\mu_a(\lambda)$ (Figure 4.2A) and the scattering coefficient $\mu_s(\lambda)$ (Figure 4.2B). The Henyey-Greenstein scattering anisotropy factor g was set to 0.9.

Table 4.1: Summary of the simulation medium composition of two physiological conditions.

	Medium composition							
	Water (%)	Fat (%)	Blood (%)	Oxygen saturation of hemoglobin (%)	[HbO] (μM)	[HHb] (μM)	[oxCCO] (μM)	[redCCO] (μM)
Baseline condition	75	10	1	70	16.3	6.9	0.1	0.4
Stimulated condition	75	10	1	85	19.8	3.4	0.4	0.1

Note that the concentrations of HbO and HHb were estimated from the predefined percentages of blood and oxygen saturation of hemoglobin, with an average concentration of hemoglobin in blood equal to 150 g/liter.

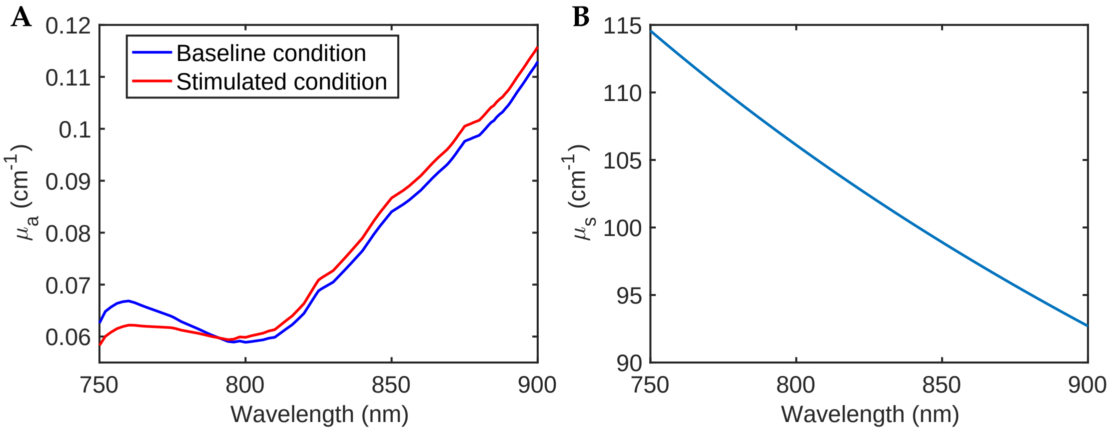

Figure 4.2: (**A**) Absorption coefficient $\mu_a(\lambda)$ for two physiological conditions and (**B**) Scattering coefficient $\mu_s(\lambda)$ used in MC simulation.

A light source and a detector of 2 cm distance were also defined and placed on the top surface of the 3D voxel model. MC simulation was repeated for different wavelengths within the NIRS range from 780 to 900 nm with 1-nm wavelength resolution, leading to a total of 121 wavelengths, for two physiological conditions. For each MC simulation execution, 50 million (i.e., 5×10^7) photon packets were launched from the light source. The number of photons reaching the detector and their partial pathlengths were recorded for later use when calculating the changes in chromophore concentrations. We repeated the MC simulation 20 times for each wavelength and for each physiological condition. The recorded data were further permuted within each wavelength and each condition 50 times. Gaussian noise was also added to enrich the simulated data. Thus, the whole simulation framework can be considered to generate bbNIRS data of 50 measurements. Each consisted of 20 spectra for each condition, namely, I_0 for the baseline condition and I for the stimulated state.

4.2.5 Comparison of Measurement or Simulation versus Theoretical Results of $\sigma_{\Delta[\mathbf{HbO}]}$, $\sigma_{\Delta[\mathbf{HHb}]}$ and $\sigma_{\Delta[\mathbf{oxCCO}]}$

We sought to compare $\sigma^T_{\Delta[\text{HbO}]}$, $\sigma^T_{\Delta[\text{HHb}]}$ and $\sigma^T_{\Delta[\text{oxCCO}]}$ obtained by the analytical computations versus those by the bbNIRS measurement or MC simulation data, namely, $\sigma^M_{\Delta[\text{HbO}]}$, $\sigma^M_{\Delta[\text{HHb}]}$ and $\sigma^M_{\Delta[\text{oxCCO}]}$. The comparison procedure is depicted in Figure 4.3. On the one hand, we first calculated Δ[HbO], Δ[HHb], and Δ[oxCCO] from the detected spectra by fitting the modified Beer-Lambert law. Consequently, the standard deviation of measured Δ[HbO], Δ[HHb], and Δ[oxCCO], namely, $\sigma^M_{\Delta[\text{HbO}]}$, $\sigma^M_{\Delta[\text{HHb}]}$ and $\sigma^M_{\Delta[\text{oxCCO}]}$, were then computed. On the other hand, the SNR of the bbNIRS measurements was estimated as SNR $= \bar{I}^2/\sigma_I^2$, where $\bar{I}$ is the mean spectral intensity and σ_I^2 is the variance of spectra. The SNR curve was then substituted into Eq. (4.11) to compute $\sigma^T_{\Delta[\text{HbO}]}$, $\sigma^T_{\Delta[\text{HHb}]}$ and $\sigma^T_{\Delta[\text{oxCCO}]}$ from the theoretical analysis, namely, error propagation (EP) caused by system SNR. These steps were repeated for multiple measurements. The measured $\sigma^M_{\Delta[\text{HbO}]}$, $\sigma^M_{\Delta[\text{HHb}]}$ and $\sigma^M_{\Delta[\text{oxCCO}]}$ and the EP by system SNR $\sigma^T_{\Delta[\text{HbO}]}$, $\sigma^T_{\Delta[\text{HHb}]}$ and $\sigma^T_{\Delta[\text{oxCCO}]}$ were finally compared to verify/confirm the accuracy of the quantitative analysis.

4.3 Results

4.3.1 Standard deviation of Δ[HbO], Δ[HHb] and Δ[oxCCO] Derived from Error Propagation Analysis and Actual Measurement Data

Figure 4.4 presents comparative results of $\sigma^M_{\Delta[\text{HbO}]}$, $\sigma^M_{\Delta[\text{HHb}]}$ and $\sigma^M_{\Delta[\text{oxCCO}]}$ obtained from the measurement data and $\sigma^T_{\Delta[\text{HbO}]}$, $\sigma^T_{\Delta[\text{HHb}]}$ and $\sigma^T_{\Delta[\text{oxCCO}]}$ from the theoretical analysis (Eq. (4.11)). Specifically, the mean and standard deviation spectra of SNR estimated from the detected optical spectra of multiple measurements are depicted in Figures 4.4(A)-4.4(C), taken from (A) spectrometer 1 in the phantom measurement, (B) spectrometer 2 also in the concurrent phantom experiment,

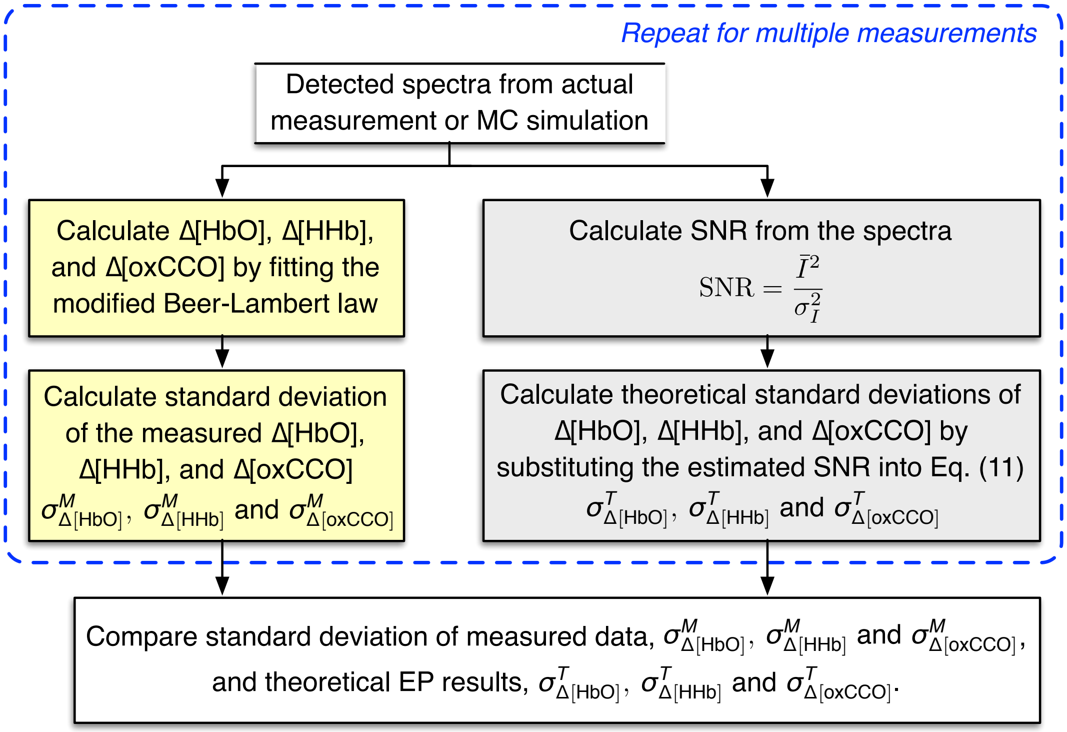

Figure 4.3: Procedure for comparing $\sigma^M_{\Delta[\mathrm{HbO}]}$, $\sigma^M_{\Delta[\mathrm{HHb}]}$ and $\sigma^M_{\Delta[\mathrm{oxCCO}]}$ obtained from the bbNIRS measurement or MC-simulation data (yellow-shaded steps) and the theoretical EP $\sigma^T_{\Delta[\mathrm{HbO}]}$, $\sigma^T_{\Delta[\mathrm{HHb}]}$ and $\sigma^T_{\Delta[\mathrm{oxCCO}]}$ calculated using system SNR (gray-shaded steps).

and (C) the human forearm measurement, respectively. Consequently, Figures 4.4(D)-4.4(F) show $\sigma^M_{\Delta[\mathrm{HbO}]}$, $\sigma^M_{\Delta[\mathrm{HHb}]}$ and $\sigma^M_{\Delta[\mathrm{oxCCO}]}$ computed/derived from the measured optical spectra (red bars) versus $\sigma^T_{\Delta[\mathrm{HbO}]}$, $\sigma^T_{\Delta[\mathrm{HHb}]}$ and $\sigma^T_{\Delta[\mathrm{oxCCO}]}$ by theoretically derived EP (blue bars).

As seen in Figures 4.4(A) to 4.4(C), the spectral shapes of SNR appeared to be different from one another. This observation is understandable since each of them was obtained from a specific bbNIRS system. Specifically, SNR spectra in Figures 4.4(A) and 4.4(B) were derived from the data collected concurrently by two spectrometers under the same experimental conditions, and the differences in the spectral sensitivity of these two spectrometers led to distinctive SNR spectral shapes. The bbNIRS data from the human arm experiment (Figure 4.4(C)) were acquired by the same QE-Pro spectrometer as in the solid phantom/spectrometer 2 case (Figure 4.4(B)). However, different exposure times for data acquisition (5 sec vs. 1 sec) resulted in un-identical SNR spectra.

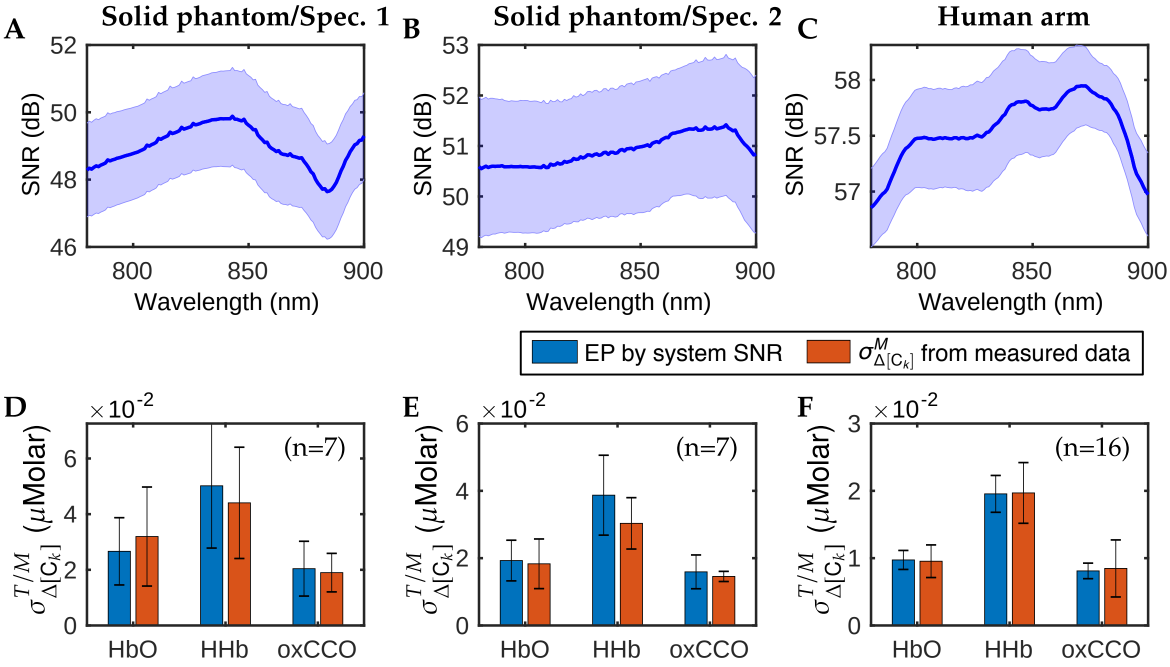

Figure 4.4: The top row depicts the mean and standard deviation of SNR spectra from (**A**) the solid phantom measurement with spectrometer 1, (**B**) the solid phantom measurement with spectrometer 2, and (**C**) the human forearm measurement. The bottom row shows the $\sigma^T_{\Delta[\mathrm{HbO}]}$, $\sigma^T_{\Delta[\mathrm{HHb}]}$ and $\sigma^T_{\Delta[\mathrm{oxCCO}]}$ obtained from the error propagation analysis (blue bars) and $\sigma^M_{\Delta[\mathrm{HbO}]}$, $\sigma^M_{\Delta[\mathrm{HHb}]}$ and $\sigma^M_{\Delta[\mathrm{oxCCO}]}$ from the measurement data (red bars). Error bars indicate the standard error of the mean of each group.

Despite the variations of SNR spectra, no significant differences were found between measured $\sigma^M_{\Delta[\mathrm{HbO}]}$, $\sigma^M_{\Delta[\mathrm{HHb}]}$ and $\sigma^M_{\Delta[\mathrm{oxCCO}]}$ versus $\sigma^T_{\Delta[\mathrm{HbO}]}$, $\sigma^T_{\Delta[\mathrm{HHb}]}$ and $\sigma^T_{\Delta[\mathrm{oxCCO}]}$ calculated directly from the EP analysis (Eq. (4.11)) in all the cases. Specifically, the human forearm measurement led to a high SNR range (i.e., 57-58 dB) (Figure 4.4(C)) and low $\sigma^{M/T}_{\Delta[\mathrm{HbO}]}$, $\sigma^{M/T}_{\Delta[\mathrm{HHb}]}$ and $\sigma^{M/T}_{\Delta[\mathrm{oxCCO}]}$ (Figure 4.4(F)) because of a prolonged exposure time for data acquisition (5 sec). The same spectrometer was used in the solid phantom measurement, but a shorter exposure time of 1 sec resulted in a reduced SNR range of the measured data (Figure 4.4(B)). The measured data from both spectrometers in the solid phantom measurement led to higher $\sigma^{M/T}_{\Delta[\mathrm{HbO}]}$, $\sigma^{M/T}_{\Delta[\mathrm{HHb}]}$ and $\sigma^{M/T}_{\Delta[\mathrm{oxCCO}]}$ compared to the human arm measurement.

4.3.2 Standard deviation of Δ[HbO], Δ[HHb] and Δ[oxCCO] Derived from Error Propagation Analysis and MC Simulation Data

We also compared the uncertainties of Δ[HbO], Δ[HHb] and Δ[oxCCO] obtained from the MC simulation and EP results derived from the corresponding SNR. Figure 4.5(A) depicts the mean and standard deviation spectra of SNR of the MC simulation, while Figure 4.5(B) presents the comparative results of $\sigma^T_{\Delta[\mathrm{HbO}]}$, $\sigma^T_{\Delta[\mathrm{HHb}]}$ and $\sigma^T_{\Delta[\mathrm{oxCCO}]}$ derived from the proposed EP calculation (blue bars) and $\sigma^M_{\Delta[\mathrm{HbO}]}$, $\sigma^M_{\Delta[\mathrm{HHb}]}$ and $\sigma^M_{\Delta[\mathrm{oxCCO}]}$ computed from the MC simulation data (red bars). One more time, no significant difference was found in the standard deviation of chromophore concentration changes calculated from the MC simulation data and from the EP analysis. The SNR of the MC simulation (Figure 4.5(A)) was lower than those of the real measurements (Figures 4.4(A-C) due to the MC simulation settings. Nevertheless, it could be improved by having a larger tissue volume and a larger number of photons. Generally, the higher the average SNR of the measurement system, the lower the error propagates to the calculated changes in chromophore concentration.

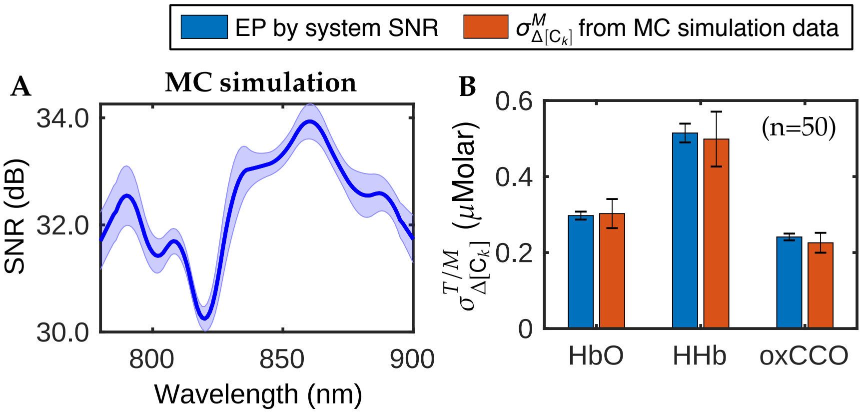

Figure 4.5: (**A**) Mean and standard deviation of SNR spectra from MC simulation data and (**B**) Comparison of $\sigma^T_{\Delta[\mathrm{HbO}]}$, $\sigma^T_{\Delta[\mathrm{HHb}]}$ and $\sigma^T_{\Delta[\mathrm{oxCCO}]}$ obtained from the error propagation analysis (blue bars) and $\sigma^M_{\Delta[\mathrm{HbO}]}$, $\sigma^M_{\Delta[\mathrm{HHb}]}$ and $\sigma^M_{\Delta[\mathrm{oxCCO}]}$ from the MC simulation data (red bars). Error bars indicate the standard error of the mean of each group.

These results confirmed that the analytically derived expressions of $\sigma^T_{\Delta[\mathrm{HbO}]}$, $\sigma^T_{\Delta[\mathrm{HHb}]}$ and $\sigma^T_{\Delta[\mathrm{oxCCO}]}$ matched well with those obtained from true experiments and MC simulations. Thus, the theoretical analysis of EP (i.e., Eq. (4.11)) can be used as a quick reference or prediction to estimate measurement errors or accuracy of Δ[HbO], Δ[HHb] and Δ[oxCCO] given an SNR of a bbNIRS system. In the following two sub-sections, we applied the EP analysis to examine the influence of wavelength selection and spectral range of bbNIRS on the variance of chromophore concentration changes. Note that the values of the optical pathlength $L(\lambda_i) = r \times \mathrm{DPF}(\lambda_i)$ can be estimated by diffusion theory, as given in refs. [143, 178].

4.3.3 Influence of Selection of Wavelengths on $\sigma^T_{\Delta[\mathrm{HbO}]}$, $\sigma^T_{\Delta[\mathrm{HHb}]}$ and $\sigma^T_{\Delta[\mathrm{oxCCO}]}$

We further illustrated how wavelength selections would affect the SNR-derived $\sigma^T_{\Delta[\mathrm{HbO}]}$, $\sigma^T_{\Delta[\mathrm{HHb}]}$ and $\sigma^T_{\Delta[\mathrm{oxCCO}]}$. Theoretically, to quantify values of Δ[HbO], Δ[HHb] and Δ[oxCCO], at least three wavelengths are required for NIRS measurements. However, because of the spectrally smooth feature of CCO, it is rather challenging to accurately quantify Δ[oxCCO]. A small number of wavelengths typically leads to inaccurate quantification of Δ[HbO], Δ[HHb] and Δ[oxCCO]. To address this problem, broadband spectroscopy with a full wavelength range of measurement has been suggested and utilized in recent studies, such as 740-900 nm in studies of [75, 101, 102, 212], 770-905 nm in publications of [12, 13], and 780-900 nm in reports of [60, 75, 101, 102]. Since a large number of wavelengths required in bbNIRS can be an obstacle for development of a compact or portable system [37], various studies made efforts to find an optimal set of wavelengths to minimize the number of required wavelengths while keeping satisfactory accuracy for the quantifications [9]. Bale et al. [11] reviewed existing clinical NIRS systems and summarized different broadband ranges or wavelength combinations used in these systems. We followed this review paper and selected/updated some representative wavelength ranges or wavelength combinations to illustrate how wavelength selections affect the accuracy of the calculated chromophore concentration changes. Table 4.2 summarizes different ranges of wavelengths or optimal wavelength sets that have been in the literature to estimate Δ[HbO], Δ[HHb] and Δ[oxCCO]. Note that Sudakou et al. [192] performed a Monte Carlo study to estimate Δ[CCO] uncertainty using 16 consecutive wavelengths separated by an equal interval of 12.5 nm with a moving spectral window covering from 650 nm to 950 nm. However, such a study focused on the time-resolved NIRS and utilized a 3-layer model (scalp, skull, and brain). Consequently, the error propagation analysis included the moment method for analyzing time-resolved statistical uncertainty and multilayer considerations. Thus, the variance of Δ[CCO] and respective analysis by Sudakou et al. were distinct from this work and thus excluded in Table 4.2 for comparison.

Figure 4.6 depicts $\sigma^T_{\Delta[\mathrm{HbO}]}$, $\sigma^T_{\Delta[\mathrm{HHb}]}$ and $\sigma^T_{\Delta[\mathrm{oxCCO}]}$ calculated using the EP analytical expression (i.e., Eq. (4.11)) for different broadband wavelength ranges (Figure 4.6A) or different wavelength combinations (Figure 4.6B). Selections of the ranges or combinations were based on the exact values given in Table 4.2. In these calculations, we temporally assumed a constant SNR value across all wavelengths and performed the EP calculation for different SNR values varying from 20 to 60 dB (equivalently, noise level (NL) being from 10% to 0.1%). As shown in Fig. 4.6(A), the broadest bandwidth of 720-920 nm (with 201 wavelengths) led to the smallest $\sigma^T_{\Delta[\mathrm{HbO}]}$, $\sigma^T_{\Delta[\mathrm{HHb}]}$ and $\sigma^T_{\Delta[\mathrm{oxCCO}]}$, while the narrowest range of 780-900 nm (with 121 wavelengths) resulted in the largest EP in respective concentrations, especially for the case of Δ[HHb]. In the case of using a limited number of wavelengths, calculated $\sigma^T_{\Delta[\mathrm{HbO}]}$, $\sigma^T_{\Delta[\mathrm{HHb}]}$ and $\sigma^T_{\Delta[\mathrm{oxCCO}]}$ increased noticeably, even by visual comparison between Figs. 4.6(A) and 4.6(B). For instance, at an SNR of 40 dB, EP varied from 0.08-0.12 μM for Δ[HbO] and from 0.05-0.1 μM for Δ[oxCCO] when using all wavelengths of bbNIRS, while the EP increased by at least four times when using a limited number of wavelengths; namely, EP varied from 0.25 to 0.64 μM for Δ[HbO] and from 0.2 to 0.5 μM for Δ[oxCCO]. In most

Table 4.2: Summary of different ranges of wavelengths or optimal wavelength combination sets.

Refs	Wavelength range or wavelength combination	Number of wave-lengths
[216]	720-920	201
[75, 101, 102]	740-900	161
[12, 13]	770-905	136
[60, 75, 101, 102]	780-900	121
[216]	720-920, 20 nm resolution	11
[60]	780-900, 5 nm resolution	25
[9, 60]	784, 800, 818, 835, 851, 868, 881, 894	8
[37]	778, 808, 814, 841, 847, 879, 888, 898	8
[216]	784, 809, 849, 889	4

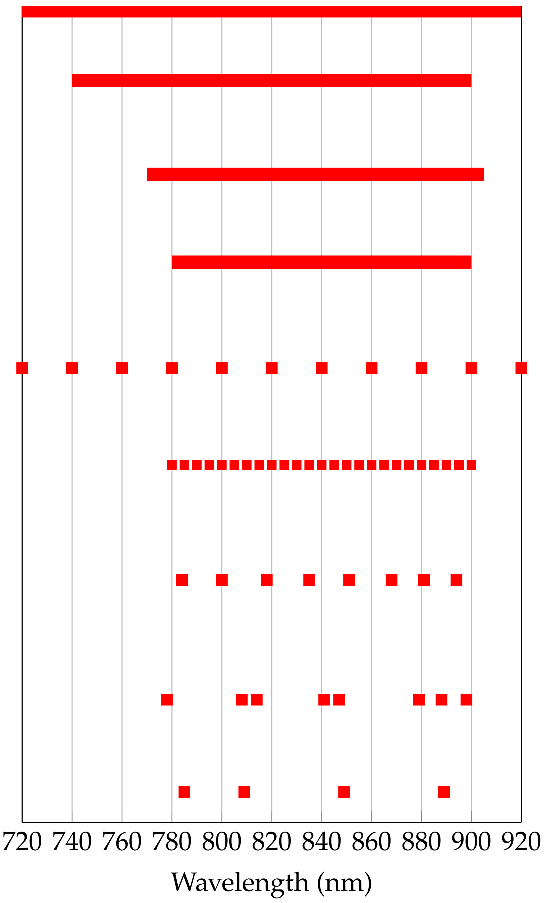

cases, the more wavelengths used to calculate concentration changes of each chromophore, the smaller error propagation in the results. For the case that the same number of wavelengths was used (e.g., 8 wavelengths used in [9, 60] or in [37]), the distinct wavelength combinations led to different error propagation results. For instance, these two sets of 8 wavelengths led to approximate $\sigma^T_{\Delta[\mathrm{HbO}]}$ value but distinct $\sigma^T_{\Delta[\mathrm{HHb}]}$ and $\sigma^T_{\Delta[\mathrm{oxCCO}]}$ (green and pink curves in Figure 4.6B).

Note that the results presented here should be considered as approximate references to roughly estimate $\sigma^T_{\Delta[\mathrm{HbO}]}$, $\sigma^T_{\Delta[\mathrm{HHb}]}$ and $\sigma^T_{\Delta[\mathrm{oxCCO}]}$ measured from a bbNIRS system with an approximate SNR

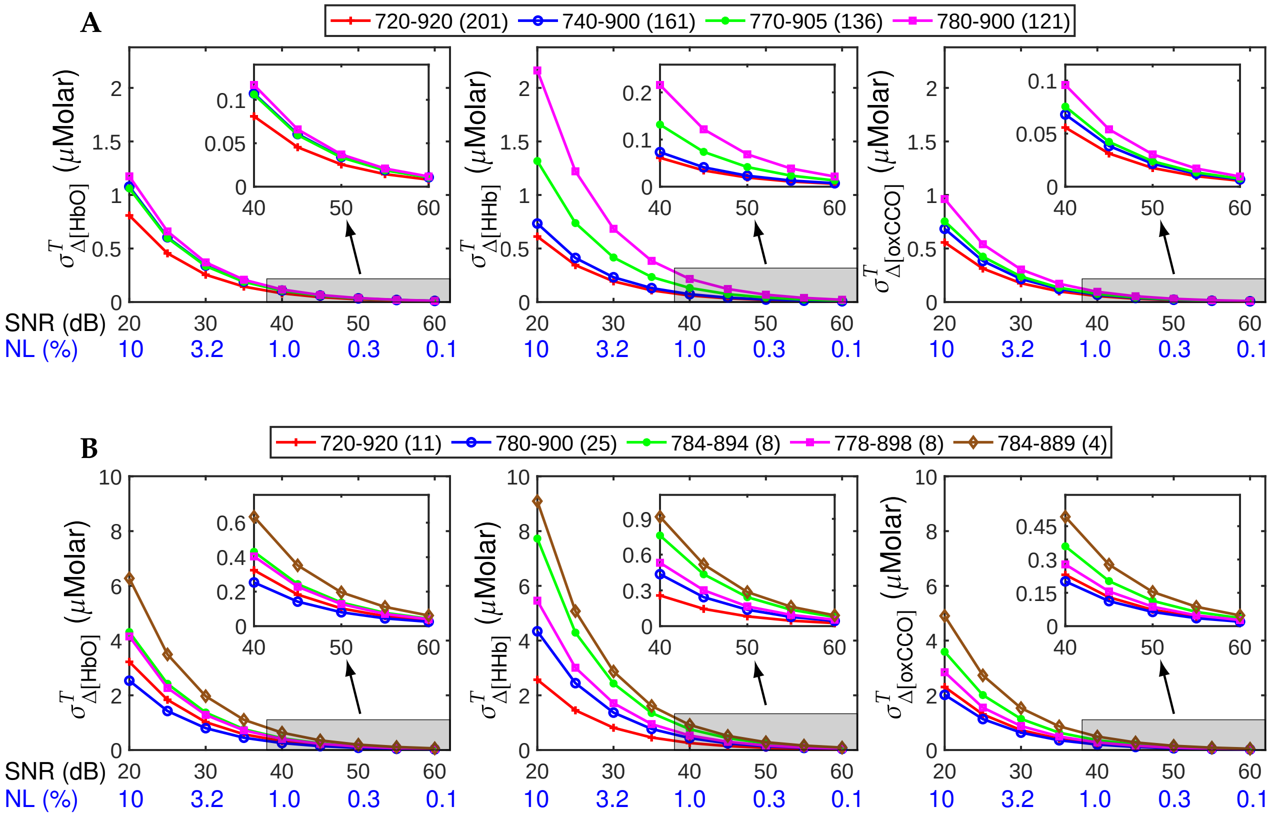

Figure 4.6: Influence of different spectral ranges of wavelengths or wavelength combinations on $\sigma^T_{\Delta[\mathrm{HbO}]}$, $\sigma^T_{\Delta[\mathrm{HHb}]}$ and $\sigma^T_{\Delta[\mathrm{oxCCO}]}$ for a bbNIRS system. (**A**) $\sigma^T_{\Delta[\mathrm{HbO}]}$, $\sigma^T_{\Delta[\mathrm{HHb}]}$ and $\sigma^T_{\Delta[\mathrm{oxCCO}]}$ obtained by using a broad range of bandwidths. The numbers in the legend labels correspond to the spectral bandwidth, while the number within the parenthesis is the total number of wavelengths used to compute $\sigma^T_{\Delta[\mathrm{HbO}]}$, $\sigma^T_{\Delta[\mathrm{HHb}]}$ and $\sigma^T_{\Delta[\mathrm{oxCCO}]}$. (**B**) $\sigma^T_{\Delta[\mathrm{HbO}]}$, $\sigma^T_{\Delta[\mathrm{HHb}]}$ and $\sigma^T_{\Delta[\mathrm{oxCCO}]}$ obtained by using different wavelength combinations. The numbers of the legend labels correspond to the minimum and maximum wavelength values; the numbers in the parentheses are the total number of wavelengths used to compute $\sigma^T_{\Delta[\mathrm{HbO}]}$, $\sigma^T_{\Delta[\mathrm{HHb}]}$ and $\sigma^T_{\Delta[\mathrm{oxCCO}]}$.

varying within the given range. For a specific bbNIRS system with a known SNR spectrum, more precise estimations of error propagation in calculating chromophore concentration changes can be carried out by substituting the system's SNR spectrum into Eq. (4.11) according to the respective wavelength ranges or wavelength combinations.

4.3.4 Influence of Spectral Bandwidth in bbNIRS on $\sigma^T_{\Delta[\mathrm{HbO}]}$, $\sigma^T_{\Delta[\mathrm{HHb}]}$ and $\sigma^T_{\Delta[\mathrm{oxCCO}]}$

As revealed in Fig. 4.6, using a broader wavelength range in bbNIRS led to significantly smaller $\sigma^T_{\Delta[\mathrm{HbO}]}$, $\sigma^T_{\Delta[\mathrm{HHb}]}$ and $\sigma^T_{\Delta[\mathrm{oxCCO}]}$. However, to our knowledge, no study has reported the spectral-bandwidth dependence of variance in calculating chromophore concentration changes. In the following, we demonstrate how selections of spectral ranges would impact the variances of Δ[HbO], Δ[HHb] and Δ[oxCCO] based on the derived Eq. (4.11).

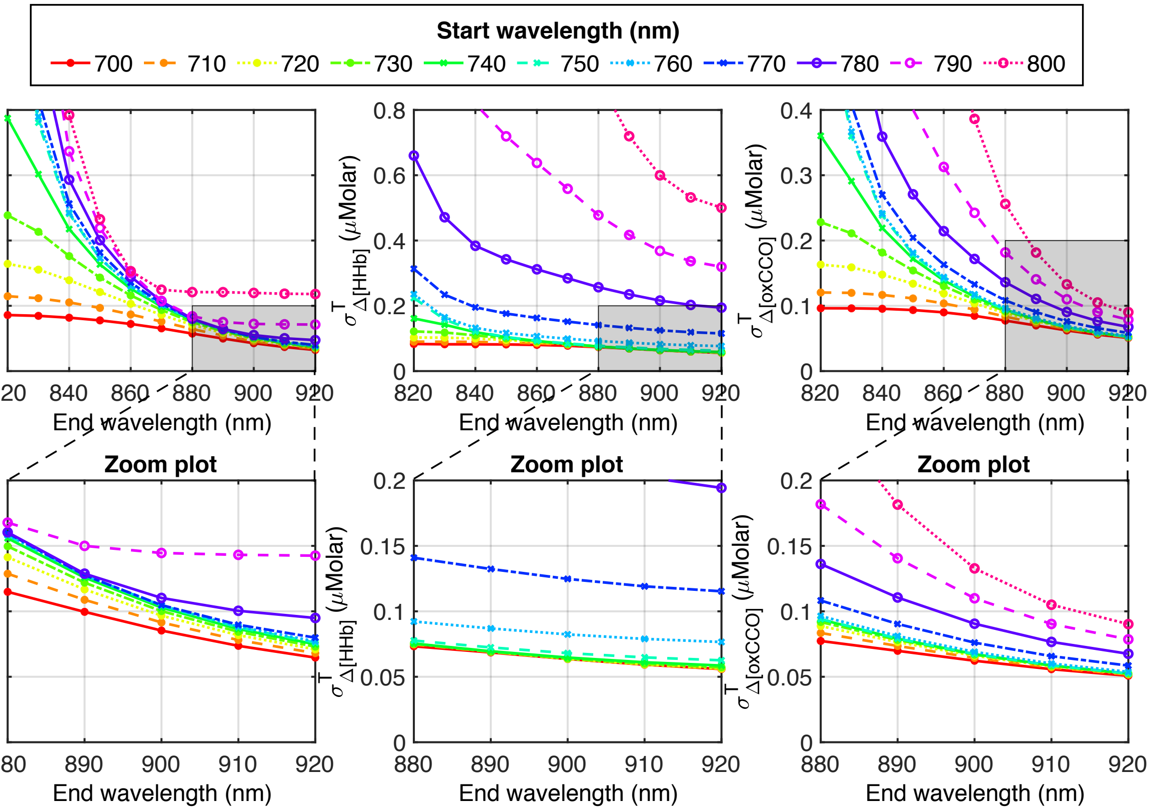

Figure 4.7: Top row: Dependance of $\sigma^T_{\Delta[\mathrm{HbO}]}$, $\sigma^T_{\Delta[\mathrm{HHb}]}$ and $\sigma^T_{\Delta[\mathrm{oxCCO}]}$, obtained by the derived EP expressions, on different spectral ranges with a spectral SNR of 40 dB. Each curve corresponds to a start wavelength of the bbNIRS spectral range as marked in the top legend, while the x-axis corresponds to the end wavelength of the bbNIRS spectral range. Bottom row: Respective zoomed plots of the gray areas shown in the top row.

As an example, three panels of Fig. 4.7 depict $\sigma^T_{\Delta[\mathrm{HbO}]}$, $\sigma^T_{\Delta[\mathrm{HHb}]}$ and $\sigma^T_{\Delta[\mathrm{oxCCO}]}$ with different spectral ranges at the SNR of 40 dB (for simplicity). Each curve in each panel plots EP dependence on spectral ranges with a starting wavelength of λ_i and an ending wavelength of λ_j, where λ_i varies from 700 nm to 800 nm in a step of 10 nm (as noted on top of the figures), and λ_j corresponds to the x-axis from 820 nm to 920 nm in each panel, also in a step of 10 nm. For instance, the red curves represent $\sigma^T_{\Delta[\mathrm{HbO}]}$, $\sigma^T_{\Delta[\mathrm{HHb}]}$ and $\sigma^T_{\Delta[\mathrm{oxCCO}]}$ obtained with spectral ranges of 700-820 nm, 700-830 nm,

. . . , and finally 700-920 nm. Similarly, the orange curves depict EP of respective concentration changes within wavelength ranges of 710-820 nm, 710-830 nm, . . . , 710-920 nm.

The three zoomed panels in Fig. 4.7 provide more detailed information. Specifically, $\sigma^T_{\Delta[\mathrm{HbO}]}$ varied around or below 0.15 μM if the starting λ_i was shorter than 780 nm and the ending λ_j equal to or longer than 880 nm. Meanwhile, both $\sigma^T_{\Delta[\mathrm{HHb}]}$ and $\sigma^T_{\Delta[\mathrm{oxCCO}]}$ had a large reduction if the start λ_i was shorter than 760 nm. Overall, the spectral range of 760-890 nm can be considered as an optimal range to minimize variances of calculated Δ[HbO], Δ[HHb] and Δ[oxCCO] in bbNIRS. Wider spectral ranges still can reduce $\sigma^T_{\Delta[\mathrm{HbO}]}$, $\sigma^T_{\Delta[\mathrm{HHb}]}$ and $\sigma^T_{\Delta[\mathrm{oxCCO}]}$, but the improvement may be non-significant.

4.4 Discussions

Accurate quantifications of Δ[HbO], Δ[HHb] and Δ[oxCCO] are of importance in most NIRS-based studies since they characterize and reflect hemodynamic and metabolic activities of the tissue under specific physiology. Since the values of Δ[HbO], Δ[HHb] and Δ[oxCCO] are deduced from measured optical densities at multiple wavelengths, the accuracy of the calculated results is inherently affected by the measurement variances or SNR of the hardware. Previous studies included analyses on the uncertainties of Δ[HbO], Δ[HHb] and Δ[oxCCO] caused by variances of extinction coefficients [97] or different wavelength combinations [32, 57, 192]. However, literature shows few publications that quantify the influence of SNR on variances of Δ[HbO], Δ[HHb] and Δ[oxCCO] derived from bbNIRS.

In this study, we performed the error propagation analysis to derive analytical variances of Δ[HbO], Δ[HHb] and Δ[oxCCO] caused by uncertainties of the bbNIRS measurement system. The derivation of EP of respective concentration changes was achieved by fitting the measured data using the least-squares method [225]. The analytical expressions and experimental/MC-simulation results were compared and confirmed statistically non-significant difference between the theoretical and measurement-based variances of chromophore concentration changes. Experimental results also indicated that the larger the SNR of a bbNIRS system, the smaller the quantified $\sigma^T_{\Delta[\mathrm{HbO}]}$, $\sigma^T_{\Delta[\mathrm{HHb}]}$ and $\sigma^T_{\Delta[\mathrm{oxCCO}]}$ (Figure 4.4(D-F)). Note that in both actual experiments presented in Sections 4.2.3 and 4.3.1, we tried to enhance the SNR of the bbNIRS system by warming up the system to reach a stable state before acquiring the data. For a new or self-designed bbNIRS system, the thermal and electrical fluctuations of the system over time should be first investigated to ensure the required warm-up time to reach the desired system stability.

In the case of bbNIRS, a large number of wavelengths with different spectral ranges or bandwidths have been considered when calculating the chromophore concentration changes [12, 13, 60, 75, 101, 102, 212], as summarized in Table 4.2. The results from our analysis clearly demonstrated that $\sigma^T_{\Delta[\mathrm{HbO}]}$, $\sigma^T_{\Delta[\mathrm{HHb}]}$ and $\sigma^T_{\Delta[\mathrm{oxCCO}]}$ were relatively small, varying from 0.07 μM to 0.1 μM for the wavelength range of 720-900 nm at an SNR of 40 dB. The bandwidth of the spectral ranges of bbNIRS also affect the variance of calculated Δ[HbO], Δ[HHb] and Δ[oxCCO]. Accordingly, Fig. 4.7 may serve as a useful guide or predictor to select an optimal spectral range/bandwidth for accurate determination of changes in chromophore concentrations by a bbNIRS measurement device.

It is worth noting that although the results presented in Figures 4.6 and 4.7 were calculated using a constant SNR value, this does not imply that the derived EP calculation cannot be applied to a real bbNIRS system where SNR has a spectral feature depending on the wavelength. We presented Figures 4.6 and 4.7 for the purpose of giving the reader an approximated amount/order of $\sigma^T_{\Delta[\mathrm{HbO}]}$, $\sigma^T_{\Delta[\mathrm{HHb}]}$ and $\sigma^T_{\Delta[\mathrm{oxCCO}]}$ caused by a certain SNR level. For instance, in our previous studies on the effects of transcranial photobiomodulation (tPBM) [158, 211], we employed the same bbNIRS system as that used in this study for the human arm measurement (Figures 4.4(C) and 4.4(G)). As seen in these two figures, SNRs in the wavelength range of 780-900 nm would be around 57-58 dB. With such a high SNR level, the respective EP were estimated or predicted to be about 0.01 μM for Δ[HbO], 0.02 μM for Δ[HHb], and less than 0.01 μM for Δ[oxCCO]. Meanwhile, the changes in [HbO] and [CCO] concentration induced by tPBM were about 5 μM and 0.6 μM, respectively [158, 211]. Compared to these actual measured values of Δ[HbO] and Δ[oxCCO], the EP caused by the measurement SNR were minimal. In particular, it is more critical to be able to estimate or predict $\sigma^T_{\Delta[\text{oxCCO}]}$ values and consequently to design optimal wavelength range, spectral bandwidth, and light exposure time. In this way, the weaker signal from less concentrated Δ[oxCCO] in tissue can be still correctly determined without being shadowed or overwhelmed by much stronger signals from Δ[HbO] and Δ[HHb].

Some efforts have also been carried out to select a limited number of wavelengths to lessen the complexity of the spectral hardware or system but still ensure the calculation or quantification accuracy [9, 32, 42, 216]. One objective of such studies was to design wearable NIRS systems [37, 219]. However, based on the results of error propagation analysis obtained in Section 4.3.1, limiting the wavelength number would lead to more uncertainties in the calculated Δ[HbO], Δ[HHb] and Δ[oxCCO]. For instance, at an SNR of 40 dB, $\sigma_{\Delta[\text{HbO}]}$, $\sigma_{\Delta[\text{HHb}]}$ and $\sigma_{\Delta[\text{oxCCO}]}$ varied from 0.2 μM to 0.9 μM if a limited number of wavelengths was used (Figure 4.6B), compared to 0.07 μM to 0.1 μM for the full bandwidth of 720-920 nm (Figure 4.6A, red curve). Moreover, distinct wavelength combinations led to different error propagation results. Thus, one may want to estimate the SNR-derived variance of Δ[HbO], Δ[HHb] and Δ[oxCCO] using different available wavelength combinations before deciding the optimal set that leads to minimal error propagation. Additional data processing or fitting steps, such as the genetic algorithm [9], may be added to help improve the quantification accuracy. If such a step is taken, further error analysis should be carried out to consider the contribution of additional steps in the EP calculation.

Last, to better understand the scientific reasoning why the variance of chromophore concentration changes depends on the spectral range and wavelength selection, we performed a mathematical expansion of the EP matrix inverse (eq. 11), as given in Appendix. The final results demonstrate that the variance for each of Δ[HbO], Δ[HHb], and Δ[oxCCO] is computed from the extinction coefficients of all three chromophores at given multiple wavelengths. Since these expressions are highly wavelength dependent and extinction coefficient nested, it is impossible to directly infer an optimal spectral bandwidth or wavelength combination that can lead to minimal error propagation. However, the knowledge learned from these equations is that the device-driven errors for Δ[HbO], Δ[HHb], and Δ[oxCCO] in a bbNIRS system depend closely on the extinction coefficient spectra of the three chromophores. Also, it might be theoretically possible to optimally select wavelengths by maximizing Eq. (4.13) and minimizing Eqs. (4.15)-(4.17) simultaneously for a given bandwidth. However, the latter point is beyond the scope of this work and needs to be investigated in future studies.

4.5 Conclusions

This study investigated the influence of SNR on variance of Δ[HbO], Δ[HHb] and Δ[oxCCO] measured by a bbNIRS device or system. Since all measured data contain inevitable uncertainties caused by thermal or electrical fluctuations or disturbance of the devices, such uncertainties or errors must impact the accuracy of the calculated Δ[HbO], Δ[HHb] and Δ[oxCCO]. Based on error propagation analysis, we derived analytical expressions of EP for all three chromophore concentrations depending on the SNR spectral curve of the bbNIRS measurement system. To compare the quantitative results and those obtained from actual bbNIRS measurements, we performed two sets of experiments on a solid tissue phantom and the human forearm using two bbNIRS systems. We also introduced an MC framework mimicking a set of bbNIRS measurements with two predefined physiological states of tissue. Both experimental and MC simulation results statistically confirmed and supported the analytical expression of the variance or EP of Δ[HbO], Δ[HHb], and Δ[oxCCO] derived in this work. Further analyses were further performed to demonstrate effects of the wavelength selection, spectral range and bandwidth, as well as spectral locations on the accuracy of the computed Δ[HbO], Δ[HHb], and Δ[oxCCO]. The presented work or results can be a helpful reference to guide optimal selections of wavelength ranges and different wavelength combinations for minimal variances of Δ[HbO], Δ[HHb], and Δ[oxCCO] in an actual bbNIRS system.

Chapter 5

Conclusions

5.1 Summary of the dissertation

The first objective of my dissertation was to investigate the neural mechanisms underlying the decision-making process, particularly under the NP context. NP-based decision-making tasks with two challenge levels were designed to assess the modulation and correlation of the task difficulty on subjects' decision-making engagement. The CorrCA method was employed to identify combinations of EEG channels that maximized the correlation across subjects or trials. The ISC and ITC values, which were considered as the attentional state marker, were computed for different task periods at the two difficulty levels. The frequency-specific powers of the CorrCA-derived projection components were also calculated. Finally, eLORETA was used to translate the forward models obtained by the ISC and ITC analyses to the potential primary sources on the human cortex. Experimental results and statistical analysis revealed strong and significant correlations in EEG signals among multiple subjects and trials during the difficult decision-making (LM) task than the easier (HM) task. Also, the NP decision-making and feedback desynchronized the normalized alpha and beta powers of the EEG, reflecting the engagement state of subjects. Source localization results also revealed several cortical/brain areas during the decision-making process, including DLPFC, aPFC, OFC, PCC, and SAC. These potential sources of neural activities were consistent with results presented in previous studies on decision-making, especially the decision-making under the business context.

The second objective was to investigate the neurophysiological and/or hemodynamic responses to the light stimulation by analyzing previously collected tPBM-fNIRS dataset. First, the cluster-based permutation test was implemented on the tPBM-evoked, whole-head Δ[HbO] signals within the broad frequency range (0-0.2 Hz), which facilitated cortical mapping of cerebral regions of significant increases in Δ[HbO] signals over the right frontopolar area near the tPBM site, confirming the findings more rigorously. Next, I focused more on the intrinsic ISO components of the cerebral activity and analyzed different ISO-dependent metrics, including (1) Δ[HbO] spectral powers, (2) frequency-specific FC, and (3) frequency-specific global network metrics. Experimental results revealed that ISO components responded differently to tPBM. Briefly, tPBM significantly increased endogenic Δ[HbO] powers across the entire cortical region and enhanced topographical FC between the frontal stimulation site and the central as well as parietal regions. Furthermore, tPBM improved not only the myogenic FC across frontal-parietal cortical regions significantly but also several global network metrics substantially. Such strong effects of tPBM on both endogenic and myogenic hemodynamics may be attributed to tPBM-evoked NO release that would stimulate endogenic oscillations and vasodilation of blood vessels. These findings met the expectation that myogenic oscillation is highly associated with the endothelial activity.

The third objective of my dissertation was to investigate the influence of SNR on variance of Δ[HbO], Δ[HHb] and Δ[oxCCO] measured by a bbNIRS system. Since all measured data contain inevitable uncertainties caused by thermal or electrical fluctuations or disturbance of the devices, such uncertainties or errors must impact the accuracy of the calculated Δ[HbO], Δ[HHb] and Δ[oxCCO]. Based on error propagation analysis, I derived analytical expressions of EP for all three chromophore concentrations depending on the SNR spectral curve of the bbNIRS measurement system. To compare the quantitative results and those obtained from actual bbNIRS measurements, two datasets obtained by experiments on a solid tissue phantom and the human forearm using two bbNIRS systems were collected. I also introduced an MC framework mimicking a set of bbNIRS measurements with two predefined physiological states of tissue. Both experimental and MC simulation results statistically confirmed and supported the analytical expression of the variance or EP of Δ[HbO], Δ[HHb], and Δ[oxCCO] derived in this work. Further analyses were performed to demonstrate effects of the wavelength selection, spectral range and bandwidth, as well as spectral locations on the accuracy of the computed Δ[HbO], Δ[HHb], and Δ[oxCCO]. The presented work or results can be a helpful reference to guide optimal selections of wavelength ranges and different wavelength combinations for minimal variances of Δ[HbO], Δ[HHb], and Δ[oxCCO] in an actual bbNIRS system.

5.2 Limitations and Future Work

In the study of investigating the neural mechanisms underlying the decision-making process, 64-channel EEG was employed to record the brain activities of subjects while performing the tasks. Although subjects were informed to limit their motion before participating in the study, they still needed to type their chosen value of the product quantity during the decision period for each trial. In addition, subjects could possibly experience a variety of emotional states while receiving feedback on the gained profits. Both situations could cause unpredictable and/or uncontrollable body motions of subjects during data acquisition. Thus, an improved protocol design with less dependence on hand/finger movements should be considered. Another limitation of this study was that the 64-channel EEG system would not facilitate high-spatial-resolution, source-localization images. Consequently, a more channel EEG system would be ideal to accurately map neural responses of the human brain to decision-based tasks.

In the tPBM-fNIRS study, a major weakness was that the potential contribution from the extracranial layers to the hemodynamic results had not been considered. Under the tPBM scenario, both the superficial and cortical layers of tissue received optical stimulation. Thus, the conventional methods to remove superficial-layer effects are not appropriate for this study. In future studies, appropriate experimental setups and algorithms should be developed to remove the confounding factor and thus confirm/refine the tPBM-induced results.

References

[1] Christian Aalkjær and Holger Nilsson. Vasomotion: Cellular background for the oscillator and for the synchronization of smooth muscle cells. British Journal of Pharmacology, 144(5):605–616, March 2005.

[2] L. I. Aftanas and S. A. Golocheikine. Human anterior and frontal midline theta and lower alpha reflect emotionally positive state and internalized attention: High-resolution EEG investigation of meditation. Neuroscience Letters, 310(1):57–60, September 2001.

[3] John P. Aggleton, Richard C. Saunders, Nicholas F. Wright, and Seralynne D. Vann. The origin of projections from the posterior cingulate and retrosplenial cortices to the anterior, medial dorsal and laterodorsal thalamic nuclei of macaque monkeys. European Journal of Neuroscience, 39(1):107–123, 2014.

[4] Fayyaz Ahmad, Iftikhar Ahmad, and Waqar Mahmood Dar. Identification and classification of voxels of human brain for rewardless-related decision making using ANN technique. Neural Computing and Applications, 28(1):1035–1041, December 2017.

[5] Zeynep Akalin Acar and Scott Makeig. Effects of Forward Model Errors on EEG Source Localization. Brain Topography, 26(3):378–396, July 2013.

[6] Fares Al-Shargie, Tong Boon Tang, and Masashi Kiguchi. Assessment of mental stress effects on prefrontal cortical activities using canonical correlation analysis: An fNIRS-EEG study. Biomedical Optics Express, 8(5):2583–2598, May 2017.

[7] Robert R. Alfano, Laura Sordillo, Yang Pu, and Lingyan Shi. Deep optical imaging of tissue with less scattering in the second, third and fourth NIR spectral windows using supercontinuum and other laser coherent light sources, November 2018.

[8] Yasunori Aoki, Ryouhei Ishii, Masao Iwase, Shunichiro Ikeda, Masahiro Hata, Leonides Canuet, Kaoru Imajo, Mieko Tanaka, Haruyasu Matsuzaki, Toshimitsu Musha, and Masatoshi Takeda. Normalized power variance change between pre-ictal and ictal phase of an epilepsy patient using NAT analysis: A case study. In 2013 35th Annual International Conference of the IEEE Engineering in Medicine and Biology Society (EMBC), pages 437–440, July 2013.

[9] Dizem Arifler, Tingting Zhu, Sara Madaan, and Ilias Tachtsidis. Optimal wavelength combinations for near-infrared spectroscopic monitoring of changes in brain tissue hemoglobin and cytochrome c oxidase concentrations. Biomedical Optics Express, 6(3):933–947, 2015.

[10] Immanuel Babu Henry Samuel, Chao Wang, Zhenhong Hu, and Mingzhou Ding. The frequency of alpha oscillations: Task-dependent modulation and its functional significance. NeuroImage, 183:897–906, December 2018.

[11] Gemma Bale, Clare E. Elwell, and Ilias Tachtsidis. From Jöbsis to the present day: A review of clinical near-infrared spectroscopy measurements of cerebral cytochrome-c-oxidase. Journal of Biomedical Optics, 21(9):091307, May 2016.

[12] Gemma Bale, Subhabrata Mitra, Isabel de Roever, Magdalena Sokolska, David Price, Alan Bainbridge, Roxana Gunny, Cristina Uria-Avellanal, Giles S Kendall, Judith Meek, et al. Oxygen dependency of mitochondrial metabolism indicates outcome of newborn brain injury. Journal of Cerebral Blood Flow & Metabolism, 39(10):2035–2047, 2019.

[13] Gemma Bale, Subhabrata Mitra, Judith Meek, Nicola Robertson, and Ilias Tachtsidis. A new broadband near-infrared spectroscopy system for in-vivo measurements of cerebral cytochrome-c-oxidase changes in neonatal brain injury. Biomedical optics express, 5(10):3450–3466, 2014.

[14] A. C. Barolet, I. V. Litvinov, and D. Barolet. Light-induced nitric oxide release in the skin beyond UVA and blue light: Red & near-infrared wavelengths. Nitric Oxide, 117:16–25, December 2021.

[15] D. W. Barrett and F. Gonzalez-Lima. Transcranial infrared laser stimulation produces beneficial cognitive and emotional effects in humans. Neuroscience, 230:13–23, January 2013.

[16] Antoine Bechara, Hanna Damasio, and Antonio R. Damasio. Emotion, Decision Making and the Orbitofrontal Cortex. Cerebral Cortex, 10(3):295–307, March 2000.

[17] Silvia Benavides-Varela and Judit Gervain. Learning word order at birth: A NIRS study. Developmental Cognitive Neuroscience, 25:198–208, 2017.

[18] Marvin H Berman, James P Halper, Trent W Nichols, H Jarrett, Alan Lundy, and Jason H Huang. Photobiomodulation with Near Infrared Light Helmet in a Pilot, Placebo Controlled Clinical Trial in Dementia Patients Testing Memory and Cognition. Journal of neurology and neuroscience, 8(1):176, 2017.

[19] Philip R Bevington, D Keith Robinson, J Morris Blair, A John Mallinckrodt, and Susan McKay. Data reduction and error analysis for the physical sciences. Computers in Physics, 7(4):415–416, 1993.

[20] Mahasweta Bhattacharya and Anirban Dutta. Computational Modeling of the Photon Transport, Tissue Heating, and Cytochrome C Oxidase Absorption during Transcranial Near-Infrared Stimulation. Brain Sciences, 9(8):179, August 2019.

[21] Irving J. Bigio and Sergio Fantini. Quantitative Biomedical Optics: Theory, Methods, and Applications. Cambridge University Press, January 2016.

[22] Nathaniel J Blanco, W Todd Maddox, and Francisco Gonzalez-Lima. Improving executive function using transcranial infrared laser stimulation. Journal of Neuropsychology, 11(1):14–25, 2017.

[23] DA Boas, CE Elwell, M Ferrari, and G Taga. Twenty years of functional near-infrared spectroscopy: Introduction for the special issue. NeuroImage, 85:1, 2014.

[24] David A Boas and Maria Angela Franceschini. Haemoglobin oxygen saturation as a biomarker: The problem and a solution. Philosophical Transactions of the Royal Society A: Mathematical, Physical and Engineering Sciences, 369(1955):4407–4424, 2011.

[25] Blanca Marin Bosch, Aurélien Bringard, Giulio Ferretti, Sophie Schwartz, and Kinga Iglói. Effect of cerebral vasomotion during physical exercise on associative memory, a near-infrared spectroscopy study. Neurophotonics, 4(4):041404, July 2017.

[26] L. A Brown, B. J Key, and T. A Lovick. Inhibition of vasomotion in hippocampal cerebral arterioles during increases in neuronal activity. Autonomic Neuroscience, 95(1):137–140, January 2002.

[27] Ed Bullmore and Olaf Sporns. Complex brain networks: Graph theoretical analysis of structural and functional systems. Nature Reviews Neuroscience, 10(3):186–198, March 2009.

[28] Niko A. Busch and Rufin VanRullen. Spontaneous EEG oscillations reveal periodic sampling of visual attention. Proceedings of the National Academy of Sciences, 107(37):16048–16053, September 2010.

[29] Danilo Bzdok, Adrian Heeger, Robert Langner, Angela R. Laird, Peter T. Fox, Nicola Palomero-Gallagher, Brent A. Vogt, Karl Zilles, and Simon B. Eickhoff. Subspecialization in the human posterior medial cortex. NeuroImage, 106:55–71, February 2015.

[30] Filipa Campos Viola, Jeremy Thorne, Barrie Edmonds, Till Schneider, Tom Eichele, and Stefan Debener. Semi-automatic identification of independent components representing EEG artifact. Clinical Neurophysiology, 120(5):868–877, May 2009.

[31] Jianwei Cao, Xinlong Wang, Hanli Liu, and George Alexandrakis. Directional changes in information flow between human brain cortical regions after application of anodal transcranial direct current stimulation (tDCS) over Broca's area. Biomedical Optics Express, 9(11):5296–5317, 2018.

[32] Charly Caredda, Laurent Mahieu-Williame, Raphaël Sablong, Michaël Sdika, Jacques Guyotat, and Bruno Montcel. Optimal spectral combination of a hyperspectral camera for intraoperative hemodynamic and metabolic brain mapping. Applied Sciences, 10(15):5158, 2020.

[33] Albert E Cerussi, Vaya W Tanamai, David Hsiang, John Butler, Rita S Mehta, and Bruce J Tromberg. Diffuse optical spectroscopic imaging correlates with final pathological response in breast cancer neoadjuvant chemotherapy. Philosophical Transactions of the Royal Society A: Mathematical, Physical and Engineering Sciences, 369(1955):4512–4530, 2011.

[34] B. Chance, C. E. Cooper, D. T. Delpy, E. O. R. Reynolds, Chris E. Cooper, and Roger Springett. Measurement of cytochrome oxidase and mitochondrial energetics by near–infrared spectroscopy. Philosophical Transactions of the Royal Society of London. Series B: Biological Sciences, 352(1354):669–676, June 1997.

[35] Christiane Charriaut-Marlangue, Philippe Bonnin, Hoa Pham, Gauthier Loron, Pierre-Louis Leger, Pierre Gressens, Sylvain Renolleau, and Olivier Baud. Nitric oxide signaling in the brain: A new target for inhaled nitric oxide? Annals of Neurology, 73(4):442–448, 2013.

[36] Wei-Liang Chen, Julie Wagner, Nicholas Heugel, Jeffrey Sugar, Yu-Wen Lee, Lisa Conant, Marsha Malloy, Joseph Heffernan, Brendan Quirk, Anthony Zinos, Scott A. Beardsley, Robert Prost, and Harry T. Whelan. Functional Near-Infrared Spectroscopy and Its Clinical Application in the Field of Neuroscience: Advances and Future Directions. Frontiers in Neuroscience, 14:724, 2020.

[37] Danial Chitnis, Dimitrios Airantzis, David Highton, Rhys Williams, Phong Phan, Vasiliki Giagka, Samuel Powell, Robert J. Cooper, Ilias Tachtsidis, Martin Smith, Clare E. Elwell, Jeremy C. Hebden, and Nicholas Everdell. Towards a wearable near infrared spectroscopic probe for monitoring concentrations of multiple chromophores in biological tissue in vivo. Review of Scientific Instruments, 87(6):065112, June 2016.

[38] Dong-Hee Choi, Kyoung-Hee Lee, Ji-Hye Kim, Moon Young Kim, Jeong Hoon Lim, and Jongmin Lee. Effect of 710nm visible light irradiation on neurite outgrowth in primary rat cortical neurons following ischemic insult. Biochemical and Biophysical Research Communications, 422(2):274–279, June 2012.

[39] Samantha S. Cohen and Lucas C. Parra. Memorable Audiovisual Narratives Synchronize Sensory and Supramodal Neural Responses. eNeuro, 3(6), November 2016.

[40] Michael J. Conlan, John W. Rapley, and Charles M. Cobb. Biostimulation of wound healing by low-energy laser irradiation A review. Journal of Clinical Periodontology, 23(5):492–496, 1996.

[41] Nicholas R Cooper, Rodney J Croft, Samuel J. J Dominey, Adrian P Burgess, and John H Gruzelier. Paradox lost? Exploring the role of alpha oscillations during externally vs. internally directed attention and the implications for idling and inhibition hypotheses. International Journal of Psychophysiology, 47(1):65–74, January 2003.

[42] Isabel de Roever, Gemma Bale, Subhabrata Mitra, Judith Meek, Nicola J Robertson, and Ilias Tachtsidis. Investigation of the pattern of the hemodynamic response as measured by functional near-infrared spectroscopy (fNIRS) studies in newborns, less than a month old: A systematic review. Frontiers in human neuroscience, 12:371, 2018.

[43] Arnaud Delorme and Scott Makeig. EEGLAB: An open source toolbox for analysis of single-trial EEG dynamics including independent component analysis. Journal of Neuroscience Methods, 134(1):9–21, March 2004.

[44] Seth G. Disner, Christopher G. Beevers, and Francisco Gonzalez-Lima. Transcranial Laser Stimulation as Neuroenhancement for Attention Bias Modification in Adults with Elevated Depression Symptoms. Brain Stimulation: Basic, Translational, and Clinical Research in Neuromodulation, 9(5):780–787, September 2016.

[45] Grzegorz M Dmochowski, Ahmed Duke Shereen, Destiny Berisha, and Jacek P Dmochowski. Near-Infrared Light Increases Functional Connectivity with a Non-thermal Mechanism. Cerebral Cortex Communications, 1(1), January 2020.

[46] Jacek P. Dmochowski, Matthew A. Bezdek, Brian P. Abelson, John S. Johnson, Eric H. Schumacher, and Lucas C. Parra. Audience preferences are predicted by temporal reliability of neural processing. Nature Communications, 5(1):4567, July 2014.

[47] Jacek P. Dmochowski, Paul Sajda, Joao Dias, and Lucas C. Parra. Correlated Components of Ongoing EEG Point to Emotionally Laden Attention – A Possible Marker of Engagement? Frontiers in Human Neuroscience, 6:112, May 2012.

[48] Turgut Durduran, Regine Choe, Wesley B Baker, and Arjun G Yodh. Diffuse optics for tissue monitoring and tomography. Reports on Progress in Physics, 73(7):076701, 2010.

[49] Janis T. Eells, Margaret T. T. Wong-Riley, James VerHoeve, Michele Henry, Ellen V. Buchman, Mary P. Kane, Lisa J. Gould, Rina Das, Marti Jett, Brian D. Hodgson, David Margolis, and Harry T. Whelan. Mitochondrial signal transduction in accelerated wound and retinal healing by near-infrared light therapy. Mitochondrion, 4(5):559–567, September 2004.

[50] Dean Falk and Kathleen R. Gibson. Evolutionary Anatomy of the Primate Cerebral Cortex. Cambridge University Press, April 2001.

[51] Qianqian Fang. Mesh-based Monte Carlo method using fast ray-tracing in Plücker coordinates. Biomedical Optics Express, 1(1):165–175, August 2010.

[52] Marco Ferrari, Makii Muthalib, and Valentina Quaresima. The use of near-infrared spectroscopy in understanding skeletal muscle physiology: Recent developments. Philosophical Transactions of the Royal Society A: Mathematical, Physical and Engineering Sciences, 369(1955):4577–4590, 2011.

[53] Flavia Filimon, Marios G Philiastides, Jonathan D Nelson, Niels A Kloosterman, and Hauke R Heekeren. How embodied is perceptual decision making? Evidence for separate processing of perceptual and motor decisions. Journal of Neuroscience, 33(5):2121–2136, 2013.

[54] Andreas Fink, Christian Rominger, Mathias Benedek, Corinna M. Perchtold, Ilona Papousek, Elisabeth M. Weiss, Anna Seidel, and Daniel Memmert. EEG alpha activity during imagining creative moves in soccer decision-making situations. Neuropsychologia, 114:118–124, June 2018.

[55] John Foxe and Adam Snyder. The Role of Alpha-Band Brain Oscillations as a Sensory Suppression Mechanism during Selective Attention. Frontiers in Psychology, 2, 2011.

[56] Andras M Fulop, Seema Dhimmer, James R Deluca, David D Johanson, Richard V Lenz, Keyuri B Patel, Peter C Douris, and Chukuka S Enwemeka. A meta-analysis of the efficacy of laser phototherapy on pain relief. The Clinical journal of pain, 26(8):729–736, October 2010.

[57] Tsukasa Funane, Hirokazu Atsumori, Hiroki Sato, Masashi Kiguchi, and Atsushi Maki. Relationship between wavelength combination and signal-to-noise ratio in measuring hemoglobin concentrations using visible or near-infrared light. Optical review, 16(4):442–448, 2009.

[58] Laurence J. Garey. Brodmann's 'Localisation In The Cerebral Cortex'. World Scientific, May 1999.

[59] Amir Hossein Ghaderi, Ali Jahan, Fatemeh Akrami, and Maryam Moghadam Salimi. Transcranial photobiomodulation changes topology, synchronizability, and complexity of resting state brain networks. Journal of Neural Engineering, 18(4):046048, May 2021.

[60] Luca Giannoni, Frédéric Lange, and Ilias Tachtsidis. Investigation of the quantification of hemoglobin and cytochrome-c-oxidase in the exposed cortex with near-infrared hyperspectral imaging: A simulation study. Journal of biomedical optics, 25(4):046001, 2020.

[61] Cinzia Giorgetta, Alessandro Grecucci, Nicolao Bonini, Giorgio Coricelli, Gianpaolo Demarchi, Christoph Braun, and Alan G. Sanfey. Waves of regret: A meg study of emotion and decision-making. Neuropsychologia, 51(1):38–51, January 2013.

[62] Matthew F. Glasser, Timothy S. Coalson, Emma C. Robinson, Carl D. Hacker, John Harwell, Essa Yacoub, Kamil Ugurbil, Jesper Andersson, Christian F. Beckmann, Mark Jenkinson, Stephen M. Smith, and David C. Van Essen. A multi-modal parcellation of human cerebral cortex. Nature, 536(7615):171–178, August 2016.

[63] Parnaz Golnar-Nik, Sajjad Farashi, and Mir-Shahram Safari. The application of EEG power for the prediction and interpretation of consumer decision-making: A neuromarketing study. Physiology & Behavior, 207:90–98, August 2019.

[64] Leo A Goodman. On the exact variance of products. Journal of the American statistical association, 55(292):708–713, 1960.

[65] Benjamin Griffiths, Ali Mazaheri, Stefan Debener, and Simon Hanslmayr. Brain oscillations track the formation of episodic memories in the real world. NeuroImage, 143:256–266, December 2016.

[66] Benjamin James Griffiths, Stephen D Mayhew, Karen J Mullinger, João Jorge, Ian Charest, Maria Wimber, and Simon Hanslmayr. Alpha/beta power decreases track the fidelity of stimulus-specific information. eLife, 8:e49562, November 2019.

[67] S L Grillo, N A Duggett, A Ennaceur, and P L Chazot. Non-invasive infra-red therapy (1072 nm) reduces β-amyloid protein levels in the brain of an Alzheimer's disease mouse model, TASTPM. Journal of photochemistry and photobiology B, Biology, 123:13–22, June 2013.

[68] Fred Grover, Jon Weston, and Michael Weston. Acute Effects of Near Infrared Light Therapy on Brain State in Healthy Subjects as Quantified by qEEG Measures. Photomedicine and Laser Surgery, 35(3):136–141, March 2017.

[69] Christian Habeck, Brian C. Rakitin, James Moeller, Nikolaos Scarmeas, Eric Zarahn, Truman Brown, and Yaakov Stern. An event-related fMRI study of the neural networks underlying the encoding, maintenance, and retrieval phase in a delayed-match-to-sample task. Cognitive Brain Research, 23(2):207–220, May 2005.

[70] Azadeh HajiHosseini and Clay B. Holroyd. Sensitivity of frontal beta oscillations to reward valence but not probability. Neuroscience Letters, 602:99–103, August 2015.

[71] Azadeh HajiHosseini and Cendri A Hutcherson. Alpha oscillations and event-related potentials reflect distinct dynamics of attribute construction and evidence accumulation in dietary decision making. eLife, 10:e60874, July 2021.

[72] Takafumi Hamaoka, Kevin K McCully, Masatsugu Niwayama, and Britton Chance. The use of muscle near-infrared spectroscopy in sport, health and medical sciences: Recent developments. Philosophical Transactions of the Royal Society A: Mathematical, Physical and Engineering Sciences, 369(1955):4591–4604, 2011.

[73] Simon Hanslmayr, Bernhard Spitzer, and Karl-Heinz Bäuml. Brain Oscillations Dissociate between Semantic and Nonsemantic Encoding of Episodic Memories. Cerebral Cortex, 19(7):1631–1640, July 2009.

[74] Yong He and Alan Evans. Graph theoretical modeling of brain connectivity. Current Opinion in Neurology, 23(4):341–350, August 2010.

[75] Hauke R Heekeren, Matthais Kohl, Hellmuth Obrig, Rüdiger Wenzel, Wolfram von Pannwitz, Steven J Matcher, Ulrich Dirnagl, Chris E Cooper, and Arno Villringer. Noninvasive assessment of changes in cytochrome-c oxidase oxidation in human subjects during visual stimulation. Journal of Cerebral Blood Flow & Metabolism, 19(6):592–603, 1999.

[76] Hauke R. Heekeren, Isabell Wartenburger, Helge Schmidt, Hans-Peter Schwintowski, and Arno Villringer. An fMRI study of simple ethical decision-making. NeuroReport, 14(9):1215–1219, July 2003.

[77] S. Gregory Hipskind, Fred L. Grover, T. Richard Fort, Dennis Helffenstein, Thomas J. Burke, Shane A. Quint, Garrett Bussiere, Michael Stone, and Timothy Hurtado. Pulsed Transcranial Red/Near-Infrared Light Therapy Using Light-Emitting Diodes Improves Cerebral Blood Flow and Cognitive Function in Veterans with Chronic Traumatic Brain Injury: A Case Series. Photomedicine and Laser Surgery, November 2018.

[78] Emma Holmes, Douglas W. Barrett, Celeste L. Saucedo, Patrick O'Connor, Hanli Liu, and F. Gonzalez-Lima. Cognitive Enhancement by Transcranial Photobiomodulation Is Associated With Cerebrovascular Oxygenation of the Prefrontal Cortex. Frontiers in Neuroscience, 13:1129, October 2019.

[79] Xin Hou, Zong Zhang, Chen Zhao, Lian Duan, Yilong Gong, Zheng Li, and Chaozhe Zhu. NIRS-KIT: A MATLAB toolbox for both resting-state and task fNIRS data analysis. Neurophotonics, 8(1):010802, January 2021.

[80] Wan-Ping Hu, Jeh-Jeng Wang, Chia-Li Yu, C. Lan, Gow-Shing Chen, and H. Yu. Helium-neon laser irradiation stimulates cell proliferation through photostimulatory effects in mitochondria. The Journal of investigative dermatology, 2007.

[81] Yi Hu, Yafeng Pan, Xinwei Shi, Qing Cai, Xianchun Li, and Xiaojun Cheng. Inter-brain synchrony and cooperation context in interactive decision making. Biological psychology, 133:54–62, 2018.

[82] Theodore J Huppert, Solomon G Diamond, Maria A Franceschini, and David A Boas. HomER: A review of time-series analysis methods for near-infrared spectroscopy of the brain. Applied Optics, 48(10):D280–D298, 2009.

[83] Jungyun Hwang, Darla M. Castelli, and F. Gonzalez-Lima. Cognitive enhancement by transcranial laser stimulation and acute aerobic exercise. Lasers in Medical Science, 31(6):1151–1160, August 2016.

[84] S Jacques, T Li, and S Prahl. Mcxyz. c, a 3D Monte Carlo simulation of heterogeneous tissues, 2013.

[85] Steven L. Jacques. Optical properties of biological tissues: A review. Physics in Medicine and Biology, 58(11):R37–R61, May 2013.

[86] N. Jaiswal, W. Ray, and S. Slobounov. Encoding of visual–spatial information in working memory requires more cerebral efforts than retrieval: Evidence from an EEG and virtual reality study. Brain Research, 1347:80–89, August 2010.

[87] Munsif Ali Jatoi, Nidal Kamel, Aamir Saeed Malik, and Ibrahima Faye. EEG based brain source localization comparison of sLORETA and eLORETA. Australasian Physical & Engineering Sciences in Medicine, 37(4):713–721, December 2014.

[88] Shudong Jiang, Brian W Pogue, Kelly E Michaelsen, Michael Jermyn, Michael A Mastanduno, Tracy E Frazee, Peter A Kaufman, and Keith D Paulsen. Pilot study assessment of dynamic vascular changes in breast cancer with near-infrared tomography from prospectively targeted manipulations of inspired end-tidal partial pressure of oxygen and carbon dioxide. Journal of biomedical optics, 18(7):076011, 2013.

[89] Lee Jollans, Robert Whelan, Louise Venables, Oliver H. Turnbull, Matteo Cella, and Simon Dymond. Computational EEG modelling of decision making under ambiguity reveals spatio-temporal dynamics of outcome evaluation. Behavioural Brain Research, 321:28–35, 2017.

[90] Valer Jurcak, Daisuke Tsuzuki, and Ippeita Dan. 10/20, 10/10, and 10/5 systems revisited: Their validity as relative head-surface-based positioning systems. NeuroImage, 34(4):1600–1611, 2007.

[91] Jon H. Kaas and Iwona Stepniewska. Motor Cortex. In V. S. Ramachandran, editor, Encyclopedia of the Human Brain, pages 159–169. Academic Press, New York, January 2002.

[92] Blair Kaneshiro, Duc T. Nguyen, Anthony M. Norcia, Jacek P. Dmochowski, and Jonathan Berger. Natural music evokes correlated EEG responses reflecting temporal structure and beat. NeuroImage, 214:116559, July 2020.

[93] Tuna Karu. Primary and secondary mechanisms of action of visible to near-IR radiation on cells. Journal of Photochemistry and Photobiology B: Biology, 49(1):1–17, March 1999.

[94] Agnes Keszler, Brian Lindemer, Neil Hogg, Dorothee Weihrauch, and Nicole L. Lohr. Wavelength-dependence of vasodilation and NO release from S-nitrosothiols and dinitrosyl iron complexes by far red/near infrared light. Archives of Biochemistry and Biophysics, 649:47–52, July 2018.

[95] Jason J. Ki, Simon P. Kelly, and Lucas C. Parra. Attention Strongly Modulates Reliability of Neural Responses to Naturalistic Narrative Stimuli. Journal of Neuroscience, 36(10):3092–3101, March 2016.

[96] Evgenii Kim, Eloise Anguluan, and Jae Gwan Kim. Monitoring cerebral hemodynamic change during transcranial ultrasound stimulation using optical intrinsic signal imaging. Scientific Reports, 7(1):13148, October 2017.

[97] Jae G Kim and H Liu. Variation of haemoglobin extinction coefficients can cause errors in the determination of haemoglobin concentration measured by near-infrared spectroscopy. Physics in Medicine & Biology, 52(20):6295, 2007.

[98] W Klimesch, M Doppelmayr, H Russegger, T Pachinger, and J Schwaiger. Induced alpha band power changes in the human EEG and attention. Neuroscience Letters, 244(2):73–76, March 1998.

[99] Laszlo Kocsis, Peter Herman, and Andras Eke. The modified Beer–Lambert law revisited. Physics in Medicine & Biology, 51(5):N91, 2006.

[100] Etienne Koechlin, Gianpaolo Basso, Pietro Pietrini, Seth Panzer, and Jordan Grafman. The role of the anterior prefrontal cortex in human cognition. Nature, 399(6732):148–151, May 1999.

[101] Christina Kolyva, Arnab Ghosh, Ilias Tachtsidis, David Highton, Chris E Cooper, Martin Smith, and Clare E Elwell. Cytochrome c oxidase response to changes in cerebral oxygen delivery in the adult brain shows higher brain-specificity than haemoglobin. Neuroimage, 85:234–244, 2014.

[102] Christina Kolyva, Ilias Tachtsidis, Arnab Ghosh, Tracy Moroz, Chris E Cooper, Martin Smith, and Clare E Elwell. Systematic investigation of changes in oxidized cerebral cytochrome c oxidase concentration during frontal lobe activation in healthy adults. Biomedical optics express, 3(10):2550–2566, 2012.

[103] Ozlem Korucuoglu, Michael P. Harms, Serguei V. Astafiev, James T. Kennedy, Semyon Golosheykin, Deanna M. Barch, and Andrey P. Anokhin. Test-retest reliability of fMRI-measured brain activity during decision making under risk. NeuroImage, 214:116759, July 2020.

[104] Clemens Kreutz and Jens Timmer. Systems biology: Experimental design. The FEBS Journal, 276(4):923–942, 2009.

[105] Sreenath P Kyathanahally, Ana Franco-Watkins, Xiaoxia Zhang, Vince D Calhoun, and Gopikrishna Deshpande. A realistic framework for investigating decision making in the brain with high spatiotemporal resolution using simultaneous EEG/fMRI and joint ICA. IEEE journal of biomedical and health informatics, 21(3):814–825, 2016.

[106] Frédéric Lange and Ilias Tachtsidis. Clinical brain monitoring with time domain NIRS: A review and future perspectives. Applied Sciences, 9(8):1612, 2019.

[107] Tobias Larsen and John P O'Doherty. Uncovering the spatio-temporal dynamics of value-based decision-making in the human brain: A combined fMRI–EEG study. Philosophical Transactions of the Royal Society B: Biological Sciences, 369(1655):20130473, 2014.

[108] Will Lawn, Ludovico Mitchener, Tom P. Freeman, Abdelmalek Benattayallah, James A. Bisby, Matt B. Wall, Chris M. Dodds, Helen V. Curran, and Celia J.A. Morgan. Value-based decision-making of cigarette and nondrug rewards in dependent and occasional cigarette smokers: An FMRI study. Addiction Biology, 25(4):e12802, 2020.

[109] Hae In Lee, Sae-Won Lee, So Young Kim, Nam Gyun Kim, Kyoung-Jun Park, Byung Tae Choi, Yong-Il Shin, and Hwa Kyoung Shin. Pretreatment with light-emitting diode therapy reduces ischemic brain injury in mice through endothelial nitric oxide synthase-dependent mechanisms. Biochemical and Biophysical Research Communications, 486(4):945–950, May 2017.

[110] Robert Leech, Rodrigo Braga, and David J. Sharp. Echoes of the Brain within the Posterior Cingulate Cortex. Journal of Neuroscience, 32(1):215–222, January 2012.

[111] Robert Leech and David J. Sharp. The role of the posterior cingulate cortex in cognition and disease. Brain, 137(1):12–32, January 2014.

[112] Robert Leech and Jonathan Smallwood. Chapter 5 - The posterior cingulate cortex: Insights from structure and function. In Brent A. Vogt, editor, Handbook of Clinical Neurology, volume 166 of Cingulate Cortex, pages 73–85. Elsevier, January 2019.

[113] Lin Li, Olajide Babawale, Amarnath Yennu, Cynthia Trowbridge, Ryan Hulla, Robert J. Gatchel, and Hanli Liu. Whole-cortical graphical networks at wakeful rest in young and older adults revealed by functional near-infrared spectroscopy. Neurophotonics, 5(3):035004, July 2018.

[114] Katharina Limbach and Paul M. Corballis. Alpha-power modulation reflects the balancing of task requirements in a selective attention task. Psychophysiology, 54(2):224–234, 2017.

[115] Hanli Liu, Yulin Song, Katherine L Worden, Xin Jiang, Anca Constantinescu, and Ralph P Mason. Noninvasive investigation of blood oxygenation dynamics of tumors by near-infrared spectroscopy. Applied Optics, 39(28):5231–5243, 2000.

[116] Nicole L. Lohr, Agnes Keszler, Phillip Pratt, Martin Bienengraber, David C. Warltier, and Neil Hogg. Enhancement of nitric oxide release from nitrosyl hemoglobin and nitrosyl myoglobin by red/near infrared radiation: Potential role in cardioprotection. Journal of Molecular and Cellular Cardiology, 47(2):256–263, August 2009.

[117] Ying Ma, Mohammed A. Shaik, Sharon H. Kim, Mariel G. Kozberg, David N. Thibodeaux, Hanzhi T. Zhao, Hang Yu, and Elizabeth M. C. Hillman. Wide-field optical mapping of neural activity and brain haemodynamics: Considerations and novel approaches. Philosophical Transactions of the Royal Society B: Biological Sciences, 371(1705):20150360, October 2016.

[118] James Macdonald, Santosh Mathan, and Nick Yeung. Trial-by-Trial Variations in Subjective Attentional State are Reflected in Ongoing Prestimulus EEG Alpha Oscillations. Frontiers in Psychology, 2:82, 2011.

[119] Richard J. Maddock, Amy S. Garrett, and Michael H. Buonocore. Posterior cingulate cortex activation by emotional words: fMRI evidence from a valence decision task. Human Brain Mapping, 18(1):30–41, 2003.

[120] Kevin J. Manning and David C. Steffens. Chapter 11 - Systems Neuroscience in Late-Life Depression. In Thomas Frodl, editor, Systems Neuroscience in Depression, pages 325–340. Academic Press, San Diego, January 2016.

[121] Josep Marco-Pallarés, Thomas F. Münte, and Antoni Rodríguez-Fornells. The role of high-frequency oscillatory activity in reward processing and learning. Neuroscience & Biobehavioral Reviews, 49:1–7, February 2015.

[122] Eric Maris and Robert Oostenveld. Nonparametric statistical testing of EEG-and MEG-data. Journal of Neuroscience Methods, 164(1):177–190, 2007.

[123] Dominik Marti, Rikke N. N. Aasbjerg, Peter E. E. Andersen, and Anders K. K. Hansen. MCmatlab: An open-source, user-friendly, MATLAB-integrated three-dimensional Monte Carlo light transport solver with heat diffusion and tissue damage. Journal of Biomedical Optics, 23(12):121622, December 2018.

[124] S. J. Matcher, C. E. Elwell, C. E. Cooper, M. Cope, and D. T. Delpy. Performance Comparison of Several Published Tissue Near-Infrared Spectroscopy Algorithms. Analytical Biochemistry, 227(1):54–68, May 1995.

[125] Ann C. McKee, Rhoda Au, Howard J. Cabral, Neil W. Kowall, Sudha Seshadri, Caroline A. Kubilus, Jon Drake, and Philip A. Wolf. Visual Association Pathology in Preclinical Alzheimer Disease. Journal of Neuropathology & Experimental Neurology, 65(6):621–630, June 2006.

[126] Molly Memel and Lee Ryan. Visual integration enhances associative memory equally for young and older adults without reducing hippocampal encoding activation. Neuropsychologia, 100:195–206, June 2017.

[127] E. Mester, T. Spiry, B. Szende, and Jolan G. Tota. Effect of laser rays on wound healing. The American Journal of Surgery, 122(4):532–535, October 1971.

[128] Dionyssios Mintzopoulos, Timothy E. Gillis, Clark E. Tedford, and Marc J. Kaufman. Effects of Near-Infrared Light on Cerebral Bioenergetics Measured with Phosphorus Magnetic Resonance Spectroscopy. Photomedicine and Laser Surgery, 35(8):395–400, August 2017.

[129] Paul Mongan, Sulpicio G. Soriano III, Tod B. Sloan, and Glenn P. Gravlee. A Practical Approach to Neuroanesthesia. Lippincott Williams & Wilkins, June 2013.

[130] Margaret A. Naeser, Michael D. Ho, Paula I. Martin, Michael R. Hamblin, and Bang-Bon Koo. Increased Functional Connectivity Within Intrinsic Neural Networks in Chronic Stroke Following Treatment with Red/Near-Infrared Transcranial Photobiomodulation: Case Series with Improved Naming in Aphasia. Photobiomodulation, Photomedicine, and Laser Surgery, 38(2):115–131, February 2020.

[131] Hiroshi Nawashiro, Kojiro Wada, Kanji Nakai, and Shunichi Sato. Focal Increase in Cerebral Blood Flow After Treatment with Near-Infrared Light to the Forehead in a Patient in a Persistent Vegetative State. Photomedicine and Laser Surgery, 30(4):231–233, April 2012.

[132] S Nioka and B Chance. NIR spectroscopic detection of breast cancer. Technology in cancer research & treatment, 4(5):497–512, 2005.

[133] Haijing Niu and Yong He. Resting-state functional brain connectivity: Lessons from functional near-infrared spectroscopy. The Neuroscientist, 20(2):173–188, 2014.

[134] Haijing Niu, Zhen Li, Xuhong Liao, Jinhui Wang, Tengda Zhao, Ni Shu, Xiaohu Zhao, and Yong He. Test-Retest Reliability of Graph Metrics in Functional Brain Networks: A Resting-State fNIRS Study. PLOS ONE, 8(9):e72425, September 2013.

[135] Haijing Niu, Jinhui Wang, Tengda Zhao, Ni Shu, and Yong He. Revealing Topological Organization of Human Brain Functional Networks with Resting-State Functional near Infrared Spectroscopy. PLOS ONE, 7(9):e45771, September 2012.

[136] J. Adam Noah, Xian Z. Zhang, Swethasri Dravida, Courtney DiCocco, Tatsuya Suzuki, Richard N. Aslin, Ilias Tachtsidis, and Joy Hirsch. Comparison of short-channel separation and spatial domain filtering for removal of non-neural components in functional near-infrared spectroscopy signals. Neurophotonics, 8(1):015004, February 2021.

[137] Michael D. Nunez, Joachim Vandekerckhove, and Ramesh Srinivasan. How attention influences perceptual decision making: Single-trial EEG correlates of drift-diffusion model parameters. Journal of Mathematical Psychology, 76:117–130, February 2017.

[138] Robert Oostenveld, Pascal Fries, Eric Maris, and Jan-Mathijs Schoffelen. FieldTrip: Open source software for advanced analysis of MEG, EEG, and invasive electrophysiological data. Computational Intelligence and Neuroscience, 2011, 2011.

[139] Ishara Paranawithana, Darren Mao, Yan T. Wong, and Colette M. McKay. Reducing false discoveries in resting-state functional connectivity using short channel correction: An fNIRS study. Neurophotonics, 9(1):015001, January 2022.

[140] Roberto D. Pascual-Marqui. Discrete, 3D distributed, linear imaging methods of electric neuronal activity. Part 1: Exact, zero error localization. arXiv:0710.3341 [math-ph, physics:physics, q-bio], October 2007.

[141] Roberto D. Pascual-Marqui, Dietrich Lehmann, Martha Koukkou, Kieko Kochi, Peter Anderer, Bernd Saletu, Hideaki Tanaka, Koichi Hirata, E. Roy John, Leslie Prichep, Rolando Biscay-Lirio, and Toshihiko Kinoshita. Assessing interactions in the brain with exact low-resolution electromagnetic tomography. Philosophical Transactions of the Royal Society A: Mathematical, Physical and Engineering Sciences, 369(1952):3768–3784, October 2011.

[142] D. Pastore, C. Di Martino, G. Bosco, and S. Passarella. Stimulation of ATP synthesis via oxidative phosphorylation in wheat mitochondria irradiated with helium-neon laser. Biochemistry and Molecular Biology International, 39(1):149–157, May 1996.

[143] Michael S Patterson, Britton Chance, and Brian C Wilson. Time resolved reflectance and transmittance for the noninvasive measurement of tissue optical properties. Applied optics, 28(12):2331–2336, 1989.

[144] Giovanni Pellegrino, Alexis Machado, Nicolas von Ellenrieder, Satsuki Watanabe, Jeffery A Hall, Jean-Marc Lina, Eliane Kobayashi, and Christophe Grova. Hemodynamic response to interictal epileptiform discharges addressed by personalized EEG-fNIRS recordings. Frontiers in Neuroscience, 10:102, 2016.

[145] Gabriel Pelletier and Lesley K. Fellows. Viewing orbitofrontal cortex contributions to decision-making through the lens of object recognition. Behavioral Neuroscience, 135(2):182–191, 2021.

[146] Philip V. Peplow, Tzu-Yun Chung, and G. David Baxter. Laser Photobiomodulation of Wound Healing: A Review of Experimental Studies in Mouse and Rat Animal Models. Photomedicine and Laser Surgery, 28(3):291–325, June 2010.

[147] Nicholas C. Petruzzi and Maqbool Dada. Pricing and the Newsvendor Problem: A Review with Extensions. Operations Research, 47(2):183–194, April 1999.

[148] Nicholas C. Petruzzi and Maqbool Dada. Newsvendor Models. In Wiley Encyclopedia of Operations Research and Management Science. John Wiley & Sons, Ltd, 2011.

[149] Paola Pinti, Felix Scholkmann, Antonia Hamilton, Paul Burgess, and Ilias Tachtsidis. Current status and issues regarding pre-processing of fNIRS neuroimaging data: An investigation of diverse signal filtering methods within a general linear model framework. Frontiers in Human Neuroscience, 12:505, 2019.

[150] Paola Pinti, Ilias Tachtsidis, Antonia Hamilton, Joy Hirsch, Clarisse Aichelburg, Sam Gilbert, and Paul W Burgess. The present and future use of functional near-infrared spectroscopy

(fNIRS) for cognitive neuroscience. Annals of the New York Academy of Sciences, 1464(1):5, 2020.

[151] M Andrea Pisauro, Elsa Fouragnan, Chris Retzler, and Marios G Philiastides. Neural correlates of evidence accumulation during value-based decisions revealed via simultaneous EEG-fMRI. Nature communications, 8:15808, 2017.

[152] Irene Sophia Plank, Catherine Hindi Attar, Stefanie Lydia Kunas, Isabel Dziobek, and Felix Bermpohl. Motherhood and theory of mind: Increased activation in the posterior cingulate cortex and insulae. Social Cognitive and Affective Neuroscience, page nsab109, October 2021.

[153] David Polezzi, Giuseppe Sartori, Rino Rumiati, Giulio Vidotto, and Irene Daum. Brain correlates of risky decision-making. Neuroimage, 49(2):1886–1894, 2010.

[154] Narun Pornpattananangkul, Shannon Grogans, Rongjun Yu, and Robin Nusslock. Single-trial EEG dissociates motivation and conflict processes during decision-making under risk. NeuroImage, 188:483–501, 2019.

[155] Andreas Trier Poulsen, Simon Kamronn, Jacek Dmochowski, Lucas C Parra, and Lars Kai Hansen. EEG in the classroom: Synchronised neural recordings during video presentation. Scientific Reports, 7:43916, 2017.

[156] Robert Oliver Poyton and Marina Hendrickson. Molecular Basis for Photobiomodulation: Light-Induced Nitric Oxide Synthesis by Cytochrome c Oxidase in Low-Level Laser Therapy. In Handbook of Low-Level Laser Therapy. Jenny Stanford Publishing, 2016.

[157] Tyrell Pruitt, Caroline Carter, Xinlong Wang, Anqi Wu, and Hanli Liu. Photobiomodulation at Different Wavelengths Boosts Mitochondrial Redox Metabolism and Hemoglobin Oxygenation: Lasers vs. Light-Emitting Diodes In Vivo. Metabolites, 12(2):103, February 2022.

[158] Tyrell Pruitt, Xinlong Wang, Anqi Wu, Elisa Kallioniemi, Mustafa M. Husain, and Hanli Liu. Transcranial Photobiomodulation (tPBM) With 1,064-nm Laser to Improve Cerebral Metabolism of the Human Brain In Vivo. Lasers in Surgery and Medicine, 52(9):807–813, 2020.

[159] Sivaraman Purushothuman, Daniel M Johnstone, Charith Nandasena, John Mitrofanis, and Jonathan Stone. Photobiomodulation with near infrared light mitigates Alzheimer's disease-related pathology in cerebral cortex – evidence from two transgenic mouse models. Alzheimer's Research & Therapy, 6(1):2, January 2014.

[160] Valentina Quaresima, Silvia Bisconti, and Marco Ferrari. A brief review on the use of functional near-infrared spectroscopy (fNIRS) for language imaging studies in human newborns and adults. Brain and language, 121(2):79–89, 2012.

[161] Brendan J Quirk, Kristina D Desmet, Michele Henry, Ellen Buchmann, Margaret Wong-Riley, Janis T Eells, and Harry T Whelan. Therapeutic effect of near infrared (NIR) light on Parkinson's disease models. Frontiers in bioscience (Elite edition), 4:818–823, January 2012.

[162] Narender Ramnani and Adrian M. Owen. Anterior prefrontal cortex: Insights into function from anatomy and neuroimaging. Nature Reviews Neuroscience, 5(3):184–194, March 2004.

[163] Erin L Rich, Frederic M Stoll, and Peter H Rudebeck. Linking dynamic patterns of neural activity in orbitofrontal cortex with decision making. Current Opinion in Neurobiology, 49:24–32, April 2018.

[164] Manuela Rizzi, Mario Migliario, Stelvio Tonello, Vincenzo Rocchetti, and Filippo Renò. Photobiomodulation induces in vitro re-epithelialization via nitric oxide production. Lasers in Medical Science, 33(5):1003–1008, July 2018.

[165] Julio C. Rojas, Aleksandra K. Bruchey, and Francisco Gonzalez-Lima. Low-Level Light Therapy Improves Cortical Metabolic Capacity and Memory Retention. Journal of Alzheimer's Disease, 32(3):741–752, January 2012.

[166] Edmund T. Rolls and Fabian Grabenhorst. The orbitofrontal cortex and beyond: From affect to decision-making. Progress in Neurobiology, 86(3):216–244, November 2008.

[167] A. B. Rowley, S. J. Payne, I. Tachtsidis, M. J. Ebden, J. P. Whiteley, D. J. Gavaghan, L. Tarassenko, M. Smith, C. E. Elwell, and D. T. Delpy. Synchronization between arterial blood pressure and cerebral oxyhaemoglobin concentration investigated by wavelet cross-correlation. Physiological Measurement, 28(2):161–173, February 2007.

[168] G. M. Rubanyi. Endothelium-derived relaxing and contracting factors. Journal of Cellular Biochemistry, 46(1):27–36, May 1991.

[169] Mikail Rubinov and Olaf Sporns. Complex network measures of brain connectivity: Uses and interpretations. NeuroImage, 52(3):1059–1069, September 2010.

[170] N Sadato, G Campbell, V Ibáñez, M Deiber, and M Hallett. Complexity affects regional cerebral blood flow change during sequential finger movements. The Journal of neuroscience, 16(8):2691–2700, April 1996.

[171] Farzad Salehpour, Fereshteh Farajdokht, Marjan Erfani, Saeed Sadigh-Eteghad, Siamak Sandoghchian Shotorbani, Michael R. Hamblin, Pouran Karimi, Seyed Hossein Rasta, and Javad Mahmoudi. Transcranial near-infrared photobiomodulation attenuates memory impairment and hippocampal oxidative stress in sleep-deprived mice. Brain Research, 1682:36–43, March 2018.

[172] M. Sofía Sappia, Naser Hakimi, Willy N. J. M. Colier, and Jörn M. Horschig. Signal quality index: An algorithm for quantitative assessment of functional near infrared spectroscopy signal quality. Biomedical Optics Express, 11(11):6732–6754, October 2020.

[173] Saman Sarraf, Danielle D. Desouza, John A. E. Anderson, and Cristina Saverino. MCADNNet: Recognizing Stages of Cognitive Impairment Through Efficient Convolutional fMRI and MRI Neural Network Topology Models. IEEE Access, 7:155584–155600, 2019.

[174] Angelo Sassaroli and Sergio Fantini. Comment on the modified Beer–Lambert law for scattering media. Physics in Medicine & Biology, 49(14):N255, 2004.

[175] Celeste L. Saucedo, Emily C. Courtois, Zachary S. Wade, Meghan N. Kelley, Nusha Kheradbin, Douglas W. Barrett, and F. Gonzalez-Lima. Transcranial laser stimulation: Mitochondrial and cerebrovascular effects in younger and older healthy adults. Brain Stimulation: Basic, Translational, and Clinical Research in Neuromodulation, 14(2):440–449, March 2021.

[176] Felix Scholkmann, Stefan Kleiser, Andreas Jaakko Metz, Raphael Zimmermann, Juan Mata Pavia, Ursula Wolf, and Martin Wolf. A review on continuous wave functional near-infrared spectroscopy and imaging instrumentation and methodology. Neuroimage, 85:6–27, 2014.

[177] Maurice E. Schweitzer and Gérard P. Cachon. Decision Bias in the Newsvendor Problem with a Known Demand Distribution: Experimental Evidence. Management Science, 46(3):404–420, March 2000.

[178] EM Sevick, B Chance, J Leigh, S Nioka, and M Maris. Quantitation of time-and frequency-resolved optical spectra for the determination of tissue oxygenation. Analytical biochemistry, 195(2):330–351, 1991.

[179] Lingyan Shi and Robert R. Alfano. Deep Imaging in Tissue and Biomedical Materials: Using Linear and Nonlinear Optical Methods. CRC Press, March 2017.

[180] Lingyan Shi, Laura A. Sordillo, Adrián Rodríguez-Contreras, and Robert Alfano. Transmission in near-infrared optical windows for deep brain imaging. Journal of Biophotonics, 9(1-2):38–43, 2016.

[181] Guofa Shou, Lei Ding, and Deepika Dasari. Probing neural activations from continuous EEG in a real-world task: Time-frequency independent component analysis. Journal of Neuroscience Methods, 209(1):22–34, July 2012.

[182] Yajing Si, Fali Li, Keyi Duan, Qin Tao, Cunbo Li, Zehong Cao, Yangsong Zhang, Bharat Biswal, Peiyang Li, Dezhong Yao, and Peng Xu. Predicting individual decision-making responses based on single-trial EEG. NeuroImage, 206:116333, February 2020.

[183] Christian M. Siedentopf, Stefan M. Golaszewski, Felix M. Mottaghy, Christian C. Ruff, Stephan Felber, and Andreas Schlager. Functional magnetic resonance imaging detects activation of the visual association cortex during laser acupuncture of the foot in humans. Neuroscience Letters, 327(1):53–56, July 2002.

[184] Gergely Silasi, Dongsheng Xiao, Matthieu P. Vanni, Andrew C. N. Chen, and Timothy H. Murphy. Intact skull chronic windows for mesoscopic wide-field imaging in awake mice. Journal of Neuroscience Methods, 267:141–149, July 2016.

[185] Martin Smith. Shedding light on the adult brain: A review of the clinical applications of near-infrared spectroscopy. Philosophical Transactions of the Royal Society A: Mathematical, Physical and Engineering Sciences, 369(1955):4452–4469, 2011.

[186] Michael E Smith and Alan Gevins. Attention and brain activity while watching television: Components of viewer engagement. Media Psychology, 6(3):285–305, 2004.

[187] Diana C. Sordillo, Laura A. Sordillo, Peter P. Sordillo, Lingyan Shi, and Robert R. Alfano. Short wavelength infrared optical windows for evaluation of benign and malignant tissues. Journal of Biomedical Optics, 22(4):045002, April 2017.

[188] Cornelis J Stam and Jaap C Reijneveld. Graph theoretical analysis of complex networks in the brain. Nonlinear Biomedical Physics, 1:3, July 2007.

[189] A. Stefanovska, M. Bracic, and H.D. Kvernmo. Wavelet analysis of oscillations in the peripheral blood circulation measured by laser Doppler technique. IEEE Transactions on Biomedical Engineering, 46(10):1230–1239, October 1999.

[190] Aneta Stefanovska. Physics of the human cardiovascular system. Contemporary Physics, 40(1):31–55, 1999.

[191] Petteri Stenroos, Jaakko Paasonen, Raimo A. Salo, Kimmo Jokivarsi, Artem Shatillo, Heikki Tanila, and Olli Gröhn. Awake Rat Brain Functional Magnetic Resonance Imaging Using Standard Radio Frequency Coils and a 3D Printed Restraint Kit. Frontiers in Neuroscience, 12:548, 2018.

[192] Aleh Sudakou, Stanislaw Wojtkiewicz, Frédéric Lange, Anna Gerega, Piotr Sawosz, Ilias Tachtsidis, and Adam Liebert. Depth-resolved assessment of changes in concentration of chromophores using time-resolved near-infrared spectroscopy: Estimation of cytochrome-c-oxidase uncertainty by Monte Carlo simulations. Biomedical optics express, 10(9):4621–4635, 2019.

[193] Thomas Tannou, Eloi Magnin, Alexandre Comte, Régis Aubry, and Sven Joubert. Neural Activation in Risky Decision-Making Tasks in Healthy Older Adults: A Meta-Analysis of fMRI Data. Brain Sciences, 11(8):1043, August 2021.

[194] Ariel Telpaz, Ryan Webb, and Dino J. Levy. Using EEG to Predict Consumers' Future Choices. Journal of Marketing Research, 52(4):511–529, August 2015.

[195] Fenghua Tian, Snehal N Hase, F Gonzalez-Lima, and Hanli Liu. Transcranial laser stimulation improves human cerebral oxygenation. Lasers in surgery and medicine, 48(4):343–349, 2016.

[196] Fenghua Tian, Haijing Niu, Bilal Khan, George Alexandrakis, Khosrow Behbehani, and Hanli Liu. Enhanced Functional Brain Imaging by Using Adaptive Filtering and a Depth Compensation Algorithm in Diffuse Optical Tomography. IEEE Transactions on Medical Imaging, 30(6):1239–1251, June 2011.

[197] Ruxandra I. Tivadar and Micah M. Murray. A Primer on Electroencephalography and Event-Related Potentials for Organizational Neuroscience. Organizational Research Methods, 22(1):69–94, January 2019.

[198] Nghi Truong, Hashini Wanniarachchi, Yan Lang, Xinlong Wang, Sridhar Nerur, Kay-Yut Chen, and Hanli Liu. Analysis of Correlation in Neural Responses across Multiple Subjects or Trials during Decision-making for Newsvendor Problem. In 2020 IEEE 20th International Conference on Bioinformatics and Bioengineering (BIBE), pages 530–537, October 2020.

[199] Yoichi Uozumi, Hiroshi Nawashiro, Shunichi Sato, Satoko Kawauchi, Katsuji Shima, and Makoto Kikuchi. Targeted increase in cerebral blood flow by transcranial near-infrared laser irradiation. Lasers in Surgery and Medicine, 42(6):566–576, 2010.

[200] Elizabeth L Urquhart, Xinlong Wang, Hanli Liu, Paul J Fadel, and George Alexandrakis. Differences in net information flow and dynamic connectivity metrics between physically active and inactive subjects measured by functional near-infrared spectroscopy (fNIRS) during a fatiguing handgrip task. Frontiers in Neuroscience, 14:167, 2020.

[201] Elizabeth L Urquhart, Hashini Wanniarachchi, Xinlong Wang, Francisco Gonzalez-Lima, George Alexandrakis, and Hanli Liu. Transcranial photobiomodulation-induced changes in human brain functional connectivity and network metrics mapped by whole-head functional near-infrared spectroscopy in vivo. Biomedical Optics Express, 11(10):5783–5799, 2020.

[202] Enrique Vargas, Douglas W. Barrett, Celeste L. Saucedo, Li-Da Huang, Jacob A. Abraham, Hirofumi Tanaka, Andreana P. Haley, and F. Gonzalez-Lima. Beneficial neurocognitive effects of transcranial laser in older adults. Lasers in Medical Science, 32(5):1153–1162, July 2017.

[203] Giovanni Vecchiato, Laura Astolfi, Fabrizio De Vico Fallani, Jlenia Toppi, Fabio Aloise, Francesco Bez, Daming Wei, Wanzeng Kong, Jounging Dai, Febo Cincotti, Donatella Mattia, and Fabio Babiloni. On the Use of EEG or MEG Brain Imaging Tools in Neuromarketing Research. Computational Intelligence and Neuroscience, 2011:643489, 2011.

[204] Anouk Vermeij, Aisha S. S. Meel-van den Abeelen, Roy P. C. Kessels, Arenda H. E. A. van Beek, and Jurgen A. H. R. Claassen. Very-low-frequency oscillations of cerebral hemodynamics and blood pressure are affected by aging and cognitive load. NeuroImage, 85:608–615, January 2014.

[205] Arno Villringer, J Planck, C Hock, L Schleinkofer, and U Dirnagl. Near infrared spectroscopy (NIRS): A new tool to study hemodynamic changes during activation of brain function in human adults. Neuroscience letters, 154(1-2):101–104, 1993.

[206] Gerd T. Waldhauser, Verena Braun, and Simon Hanslmayr. Episodic Memory Retrieval Functionally Relies on Very Rapid Reactivation of Sensory Information. Journal of Neuroscience, 36(1):251–260, January 2016.

[207] W. B. Wang, Richard Gozali, Lingyan Shi, Lukas Lindwasser, and R. R. Alfano. Deep transmission of Laguerre–Gaussian vortex beams through turbid scattering media. Optics Letters, 41(9):2069–2072, May 2016.

[208] Xinlong Wang, Jacek P Dmochowski, Li Zeng, Elisa Kallioniemi, Mustafa Husain, F Gonzalez-Lima, and Hanli Liu. Transcranial photobiomodulation with 1064-nm laser modulates brain electroencephalogram rhythms. Neurophotonics, 6(2):025013, 2019.

[209] Xinlong Wang, Liang-Chieh Ma, Sadra Shahdadian, Anqi Wu, Nghi Cong Dung Truong, and Hanli Liu. Metabolic Connectivity and Hemodynamic-Metabolic Coherence of Human Prefrontal Cortex at Rest and Post Photobiomodulation Assessed by Dual-Channel Broadband NIRS. Metabolites, 12(1):42, January 2022.

[210] Xinlong Wang, Divya D. Reddy, Sahil S. Nalawade, Suvra Pal, Francisco Gonzalez-Lima, and Hanli Liu. Impact of heat on metabolic and hemodynamic changes in transcranial infrared laser stimulation measured by broadband near-infrared spectroscopy. Neurophotonics, 5(1):011004, September 2017.

[211] Xinlong Wang, Fenghua Tian, Divya D Reddy, Sahil S Nalawade, Douglas W Barrett, Francisco Gonzalez-Lima, and Hanli Liu. Up-regulation of cerebral cytochrome-c-oxidase and hemodynamics by transcranial infrared laser stimulation: A broadband near-infrared spectroscopy study. Journal of Cerebral Blood Flow & Metabolism, 37(12):3789–3802, 2017.

[212] Xinlong Wang, Fenghua Tian, Sagar S Soni, F Gonzalez-Lima, and Hanli Liu. Interplay between up-regulation of cytochrome-c-oxidase and hemoglobin oxygenation induced by near-infrared laser. Scientific Reports, 6:30540, 2016.

[213] Xinlong Wang, Hashini Wanniarachchi, Anqi Wu, F. Gonzalez-Lima, and Hanli Liu. Transcranial photobiomodulation and thermal stimulation induce distinct topographies of EEG

alpha and beta power changes in healthy humans. Scientific Reports, 11(1):18917, September 2021.

[214] Hashini Wanniarachchi, Yan Lang, Xinlong Wang, Tyrell Pruitt, Sridhar Nerur, Kay-Yut Chen, and Hanli Liu. Alterations of Cerebral Hemodynamics and Network Properties Induced by Newsvendor Problem in the Human Prefrontal Cortex. Frontiers in Human Neuroscience, 14:598, 2021.

[215] P. Welch. The use of fast Fourier transform for the estimation of power spectra: A method based on time averaging over short, modified periodograms. IEEE Transactions on Audio and Electroacoustics, 15(2):70–73, June 1967.

[216] Petra Wobst, Rüdiger Wenzel, Matthias Kohl, Hellmuth Obrig, and Arno Villringer. Linear aspects of changes in deoxygenated hemoglobin concentration and cytochrome oxidase oxidation during brain activation. Neuroimage, 13(3):520–530, 2001.

[217] Geoffrey F. Woodman. A brief introduction to the use of event-related potentials in studies of perception and attention. Attention, Perception, & Psychophysics, 72(8):2031–2046, November 2010.

[218] Valentin Wyart, Vincent de Gardelle, Jacqueline Scholl, and Christopher Summerfield. Rhythmic Fluctuations in Evidence Accumulation during Decision Making in the Human Brain. Neuron, 76(4):847–858, November 2012.

[219] Dominik G Wyser, Olivier Lambercy, Felix Scholkmann, Martin Wolf, and Roger Gassert. Wearable and modular functional near-infrared spectroscopy instrument with multidistance measurements at four wavelengths. Neurophotonics, 4(4):041413, 2017.

[220] Jun Yao and Julius P. A. Dewald. Evaluation of different cortical source localization methods using simulated and experimental EEG data. NeuroImage, 25(2):369–382, April 2005.

[221] Ruoyang Yao, Xavier Intes, and Qianqian Fang. Direct approach to compute Jacobians for diffuse optical tomography using perturbation Monte Carlo-based photon ‘replay’. Biomedical Optics Express, 9(10):4588–4603, October 2018.

[222] Zachary Yaple, Mario Martinez-Saito, Nikita Novikov, Dmitrii Altukhov, Anna Shestakova, and Vasily Klucharev. Power of Feedback-Induced Beta Oscillations Reflect Omission of Rewards: Evidence From an EEG Gambling Study. Frontiers in Neuroscience, 12, 2018.

[223] Akio Yasukawa, Haruki Hrui, Yoshihisa Koyama, Masahiro Nagai, and Kazuo Takakuda. The Effect of Low Reactive-Level Laser Therapy (LLLT) with Helium-Neon Laser on Operative Wound Healing in a Rat Model. Journal of Veterinary Medical Science, 69(8):799–806, 2007.

[224] Jong Chul Ye, Sungho Tak, Kwang Eun Jang, Jinwook Jung, and Jaeduck Jang. NIRS-SPM: Statistical parametric mapping for near-infrared spectroscopy. NeuroImage, 44(2):428–447, 2009.

[225] Derek York. Least-squares fitting of a straight line. Canadian Journal of Physics, 44(5):1079–1086, 1966.

[226] Meryem A. Yücel, Juliette Selb, Christopher M. Aasted, Mike P. Petkov, Lino Becerra, David Borsook, and David A. Boas. Short separation regression improves statistical significance

and better localizes the hemodynamic response obtained by near-infrared spectroscopy for tasks with differing autonomic responses. Neurophotonics, 2(3):035005, September 2015.

[227] Dandan Zhang, Ruolei Gu, Tingting Wu, Lucas S Broster, Yi Luo, Yang Jiang, and Yuejia Luo. An electrophysiological index of changes in risk decision-making strategies. Neuropsychologia, 51(8):1397–1407, 2013.

[228] Quan Zhang, Emery N. Brown, and Gary E. Strangman. Adaptive filtering for global interference cancellation and real-time recovery of evoked brain activity: A Monte Carlo simulation study. Journal of Biomedical Optics, 12(4):044014, July 2007.

[229] Yiheng Zhang, Dana H Brooks, Maria Angela Franceschini, and David A Boas. Eigenvector-based spatial filtering for reduction of physiological interference in diffuse optical imaging. Journal of Biomedical Optics, 10(1):011014, 2005.

[230] Xin Zhou, Gabriel Sobczak, Colette M. McKay, and Ruth Y. Litovsky. Comparing fNIRS signal qualities between approaches with and without short channels. PLOS ONE, 15(12):e0244186, December 2020.

[231] Zhao Zhuo, Shi-Min Cai, Zhong-Qian Fu, and Jie Zhang. Hierarchical organization of brain functional networks during visual tasks. Physical Review E, 84(3):031923, September 2011.

[232] Reza Zomorrodi, Genane Loheswaran, Abhiram Pushparaj, and Lew Lim. Pulsed Near Infrared Transcranial and Intranasal Photobiomodulation Significantly Modulates Neural Oscillations: A pilot exploratory study. Scientific Reports, 9(1):6309, April 2019.

Appendix A

Alteration of EEG Power during Decision-Making Process

In Chapter 2, I have assessed the power of spatially filtered EEG signals, namely, CorrCA projection components, to better understand cortical synchrony or desynchrony of brain responses evoked through different NP task periods. However, although the experimental results on normalized power of the CorrCA projection components demonstrated synchrony reduction in the alpha and beta oscillations by the engagement state of subjects during DCS and FB periods, it is not clear which brain areas significantly contributed to the alterations in EEG power evoked by the task difficulty. Thus, in this appendix, I sought to investigate the power variations of whole-head EEG signals. The cluster-based permutation test (CBPT) [17, 122, 138, 144] was employed as the statistical method to identify significant differences in power between four task periods, namely, DCS, R1, FB, and R2, and the baseline.

A.1 Cluster-based permutation test on EEG power

To investigate the differences in brain responses to the NP task among four experimental periods, I applied the cluster-based permutation test (CBPT) [17, 122, 138, 144] to the EEG power of four task periods, namely, DCS, R1, FB, and R2, and the baseline power, i.e., the power during the first 30 s before executing the NP-based decision-making task. Such an analysis allows us to identify significant spatial clusters exhibiting the differences in brain responses to task periods. Moreover, CBPT helps to avoid the normality requirement of the assessed data and the problem of strict correction for multiple comparisons suffered by multi-channel EEG data.

The processing routine to perform the CBPT-based EEG power analysis is as follows. First, time-frequency dependent power from preprocessed EEG data was extracted using Morlet wavelets. For each subject, we obtained a $[D \times N_f \times N_t]$ power matrix, where D is the number of EEG channels, N_f is the number of frequencies, and N_t is the number of time samples (N_t equals to the whole test duration in second as the time resolution is 1 sec). The time-averaged power of 30 s of baseline (BL) and four task periods, including decision (DCS), first recovery (R1), feedback (FB), and second recovery (R2) was then calculated. Note that the power of task periods was averaged for all trials of each subject. Since the decision period duration varied from trial to trial and from subject to subject, a common duration of 5 sec was chosen to compute the average power of the decision period. This step resulted in five matrices $\mathbf{P}_{BL/DCS/R1/FB/R2} \in \mathbb{R}^{D \times N_f}$ corresponding to 30s of BL and four task periods (DCS, R1, FB, and R2), where D is the number of EEG channels and N_f is the number of frequencies. Finally, frequency-band-specific EEG power was calculated for five commonly used EEG frequency bands, namely, delta (1-4 Hz), theta(4-8 Hz), alpha (8-13 Hz), beta (13-30 Hz), and gamma (30-60 Hz), by averaging the frequency-dependent power within the corresponding frequency range. Therefore, for each frequency band and each subject, we had the frequency-band-specific power matrices $\mathbf{P}^{(m)}_{\langle pr \rangle,k} \in \mathbb{R}^{D}$, where $\langle pr \rangle$ denotes the experimental periods, including 'BL', 'DCS', 'R1', 'FB', and 'R2', $k = 1 \ldots 5$ corresponds to five EEG frequency bands and m represents the m-th subject. The concatenated power matrices of all subjects would be the input of the CBPT to investigate the difference in neural responses across four NP-based task period. Figure A.1 summarized the principle steps of this power analysis procedure.

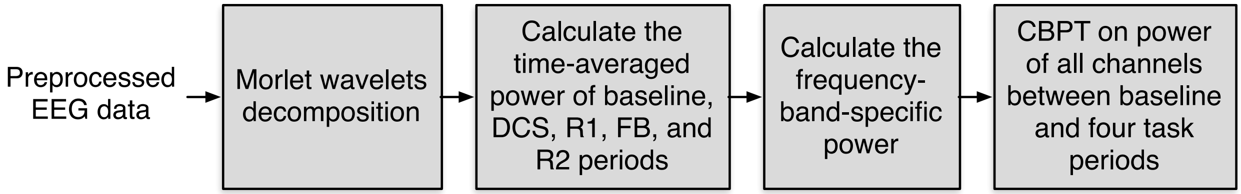

Figure A.1: Flowchart for performing the CBPT-based EEG power analysis.

I used the functions from the Fieldtrip toolbox [138] to perform the CBPT. The channel neighbors for spatial clustering were defined within a distance of 5 cm from the center channel, which resulted in an average of 5.25 neighbors per channel. The critical cluster threshold for considering a data point as a candidate member of a cluster was computed based on the statistical distribution of the permutation data and the cluster alpha of 0.05. The number of randomization was set to 2000. The Monte Carlo method was used to calculate the significance probability of each cluster. Clusters whose p-value were less than the critical $\alpha = 0.05$ were considered significant.

A.2 Experimental results

Figure A.2 depicts the results obtained by the cluster-based permutation test comparing the EEG power between baseline and four task periods. Four rows correspond to four task periods, including DCS, R1, FB, and R2, respectively. Topographical maps depict the averaged normalized power of four task periods (i.e., $\mathbf{P}_{\langle pr \rangle,k}/\mathbf{P}_{\langle BL \rangle,k}$, where $\langle pr \rangle$ can be DCS, R1, FB, or R2). Significant clusters are marked as 'x' sign for $\alpha_{\text{cluster}} = 0.05$ and '*' sign for $\alpha_{\text{cluster}} = 0.01$. The red sign means that the power of the corresponding task period is stronger than that of the baseline, while the purple sign represents vice versa.

CBPT revealed significant decrease in power of alpha and beta frequency bands during the decision period (topographical maps on the first row, third and fourth columns with purple signs). Meanwhile, significant increase in power during the first rest was observed for delta, theta, alpha, and beta frequency bands. Specifically, the alpha frequency band depicted extremely significant increase in power during the first rest compared to other frequency bands. The power decreased again during the feedback period, especially for the beta frequency band. Finally, the power increased again during the second rest, although such increase was not as strong as during the first recovery period.

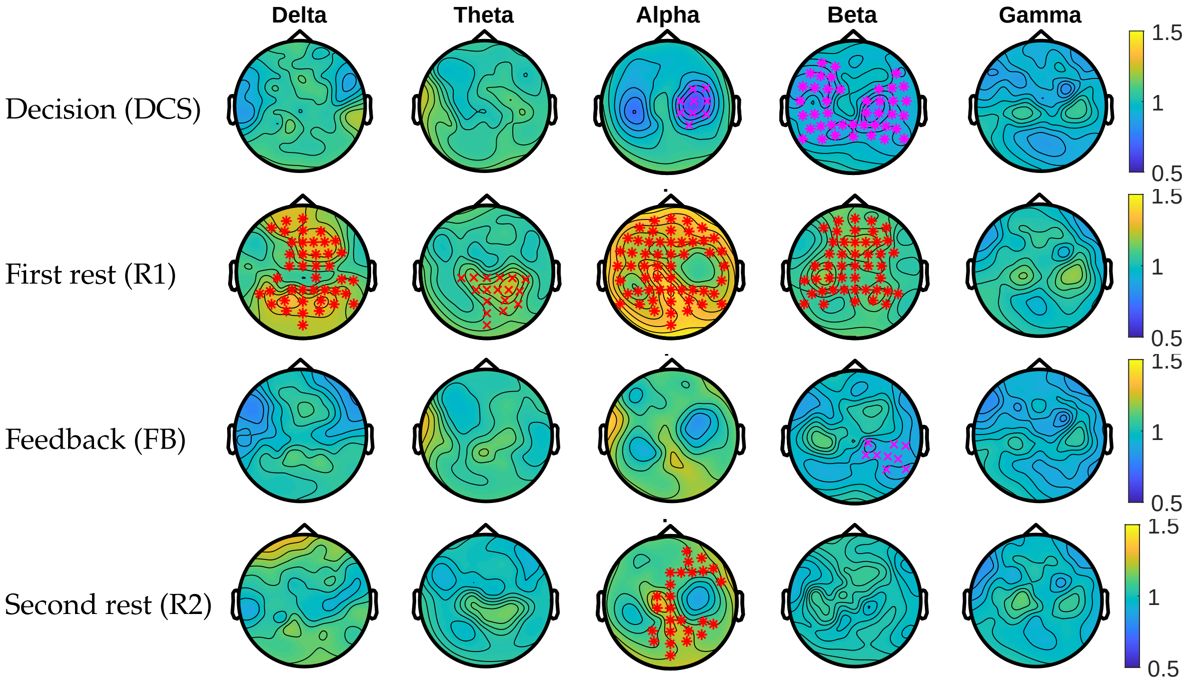

Figure A.2: Results of the cluster-based permutation test comparing the EEG power between baseline and four task periods. Topographical maps depict the normalized power of four task periods (i.e., $\mathbf{P}_{\langle pr \rangle,k}/\mathbf{P}_{\langle BL \rangle,k}$, where $\langle pr \rangle$ can be DCS, R1, FB, or R2). Significant clusters are marked as 'x' sign for $\alpha_{\text{cluster}} = 0.05$ and '*' sign for $\alpha_{\text{cluster}} = 0.01$. The red sign means that the power of the corresponding task period is stronger than that of the baseline, while the purple sign represents vice versa.

Appendix B

Optical Intrinsic Signal Imaging (OISI) System

Besides well-known imaging modalities such as EEG, MEG, or NIRS, optical intrinsic signal imaging (OISI) [96, 117] is also considered a low-cost, compact, simple neuroimaging technique to provide concurrent functional information during brain stimulation. OISI can image a large area of the small animal brain with high spatial and temporal resolution. Thus, OISI can be employed to investigate the hemodynamic responses to tPBM in mice for a better mechanistic understanding of tPBM effects.

B.1 Determining the optical pathlength for optical intrinsic signal imaging (OISI) using Monte Carlo simulation

Monte Carlo simulation [51] was used to determine the optical pathlength for OISI system. A $[3 \times 3 \times 3]$ cm slab of interest tissue was first defined by the corresponding geometry and the associated optical properties (absorption coefficient μ_a, scattering coefficient μ_s, anisotropy g, and refractive index n). The optical properties for the mouse brain was obtained from [117], while those for human arms were measured using a near infrared frequency resolved spectroscopy oximeter (Oxiplex TS, ISS Inc., Illinois USA). A surface of $[1 \times 1]$ cm was considered as the field of view of the exposed tissue. All photons exiting this field of view were considered to calculate the mean pathlength. Multiple pencil beams at different locations within the $[1.5 \times 1.5]$ cm square with a step of 0.1 cm for both x- and y-axes and with different beam angles from -45^o to 45^o with a step of 5^o were defined to represent the wide-field light source of the real system. The procedure to estimate the optical pathlength for OISI system is as follows. For each photon beam at a specific location with different angles, I launched the MC simulation and saved the path history of all detected photons. The trajectory length of each detected photon was calculated as $L_k = \sum_{i=1}^{N_k} x_{k,i} \exp[-\mu_a(\lambda)x_{k,i}]$ [221]. The average pathlength of the current photon beam was estimated as $L = \sum_{k=1}^{N} L_k/N$. I repeated the same procedure for multiple photon beams with different locations and angles. The average pathlength of all photon beams was considered as the optical pathlength for OISI system.

Table B.1: Summary of the optical properties of the simulation medium and the corresponding estimated pathlength obtained by MC simulation.

	470 nm	**530 nm**	**630 nm**
μ_a (cm^{-1})	3.78	5.43	0.29
μ_s' (cm^{-1})	12.1	10	7.6
Pathlength (cm)	0.3971	0.3461	2.1344

B.2 Aim occlusion experiment using OISI system

To verify the pathlength estimation using MC simulation, I conducted the arm occlusion experiment whose protocol is shown in Figure B.1. The arm surface will be sequentially illuminated with 470 nm, 530 nm, and 625 nm light using high-power collimator LED sources (LCS0470/0530/0625, Mightex, Toronto, ON). The reflected light will be collected using an EMCCD camera (iXon 888, Andor, UK) with an EF 50 mm f/1.2L lens (Canon, USA). The subjects were instructed to sit comfortably and keep their arm still during the experiment. A pneumatic cuff was inflated around the arm with two pressure: 100 mmHg for a venous occlusion and 200 mmHg for an arterial occlusion. Each measurement consisted of 1 min of baseline, 3 mins of arm occlusion and 3 mins of post-occlusion.

The average intensities over the whole image acquired by the camera for three wavelengths

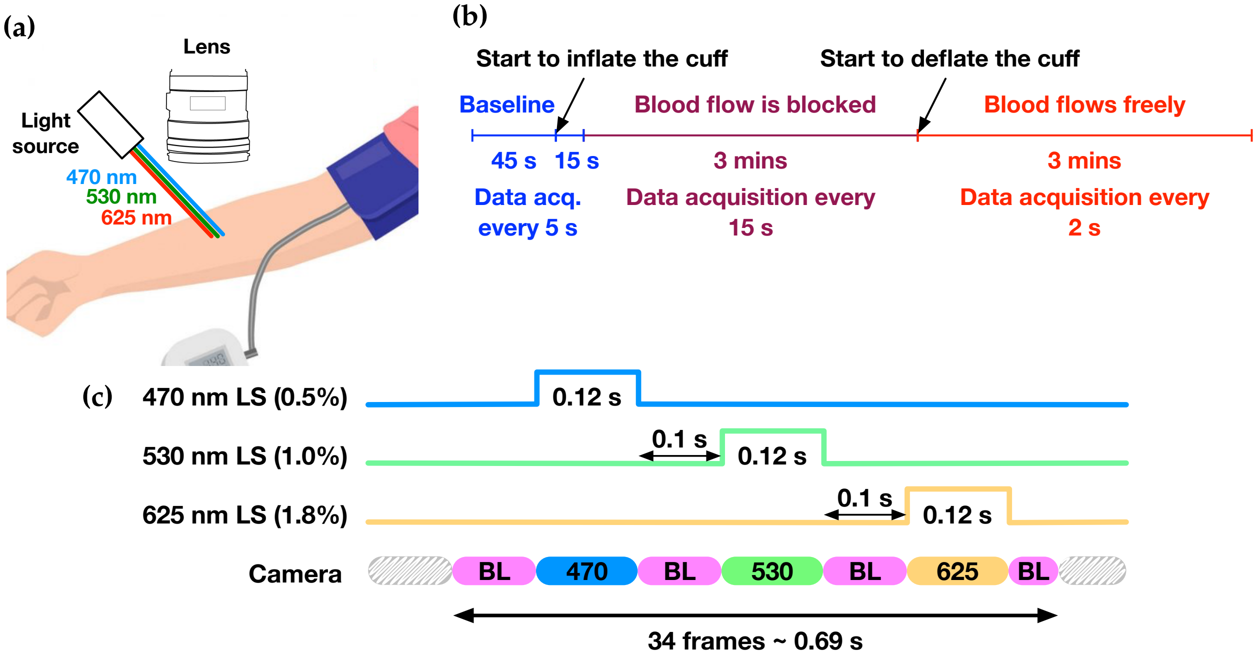

Figure B.1: Arm occlusion experimental setup and protocol. (a) OISI light source-detector configuration. (b) Arm occlusion protocol: 1 min of baseline, 3 mins of blocking blood flow, and 3 mins of free blood flow. (c) Light source timing setup. Three light sources of 470 nm, 530 nm, and 625 nm were used in the OISI system.

were utilized to estimate the changes in [HbO] and [Hb] concentrations. The calculation was based on the modified Beer-Lambert Law with the average pathlength obtained from the MC simulation. The results of Δ[HbO], Δ[Hb], and Δ[HbT] obtained for both occlusion conditions are shown in Figure B.2. For the case of venous occlusion in which the arteries still open, both Δ[HbO] and Δ[Hb] increase (as well as Δ[HbT]). For the case of arterial occlusion in which both arteries and veins are closed, we observed an increase of Δ[Hb] and a decrease of Δ[HbO], while Δ[HbT] stayed around zero. Thus, experimental results showed the reliability of the derived pathlength of OISI system obtained by MC simulation.

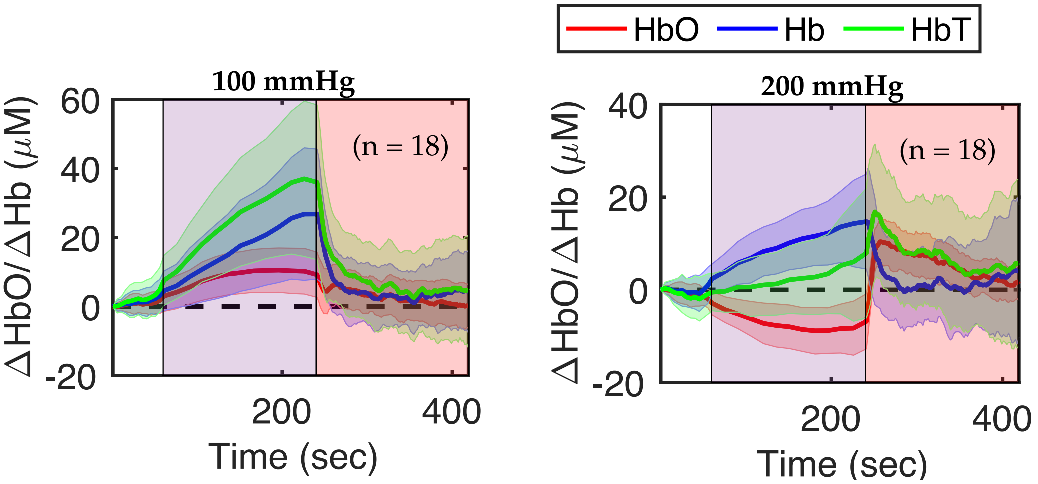

Figure B.2: Results of the arm occlusion experiment. Two occlusion conditions were used: 100 mmHg for venous occlusion (left side) and 200 mmHg for arterial occlusion (right side). Red curves indicate the changes in oxyhemoglobin concentration Δ[HbO], blue curves indicate the changes in deoxyhemoglobin concentration Δ[Hb], and green curves indicate the changes in total hemoglobin concentration. Error bars indicate the standard error of the mean (n = 18) for both venous and arterial occlusion.

B.3 Wide-field intrinsic signal imaging of the mouse skull for mechanistic understanding of tPBM effects

I plan to use OISI to investigate the responses of the exposed skull of mice to tPBM at multiple wavelengths, including 808 nm, 852 nm, and 1064 nm. The experimental protocol was being reviewed by the Institutional Animal Care and Use Committee (IACUC) of the University of Texas at Arlington. For the preliminary experiment, I plan to have a total of 20 mice for 4 groups: sham condition, tPBM with 808 nm, tPBM with 852 nm, and tPBM with 1064 nm. The experimental protocol is shown in Figure B.3.

B.3.1 Animal preparation

The wide-field cranial window for mice will be prepared following the procedure described in [184]. Briefly, the mice will be anesthetized for cranial window surgery. The scalp over both hemispheres,

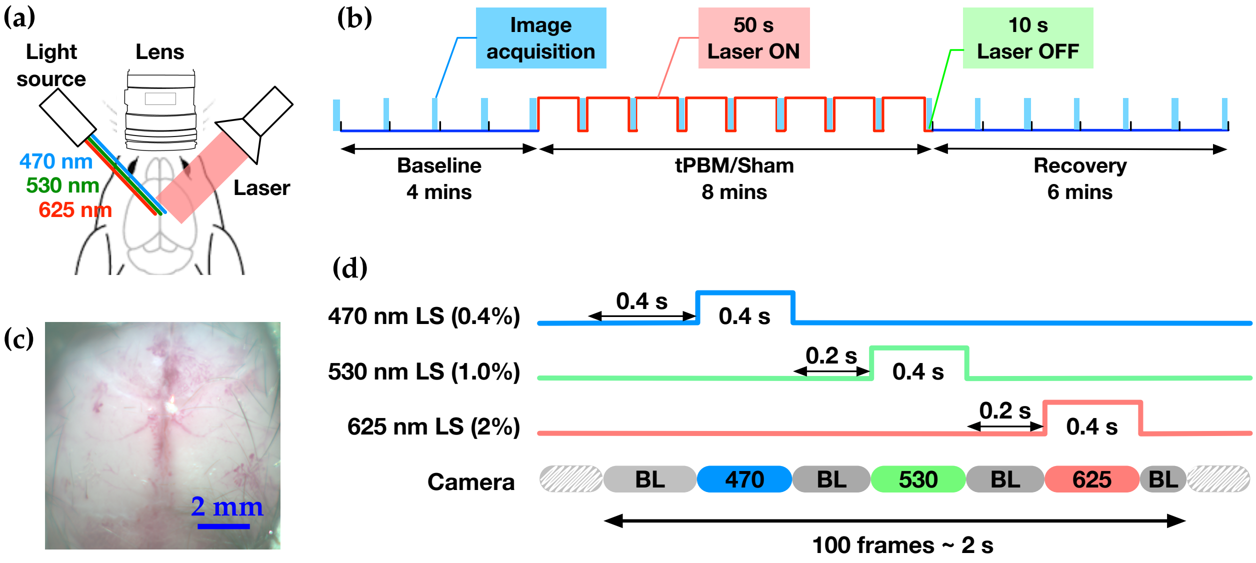

Figure B.3: (a) OISI system setup for imaging the exposed cortex of mice with tPBM. Three light sources of 470 nm, 530 nm, and 625 nm were used in the OISI system. (b) OISI with tPBM experimental protocol. (c) Demonstration of an image obtained by the OISI system for the moistened skull . (d) Light source timing setup.

approximately 8 mm in diameter, will be removed. Any existing connective tissue will be further cleaned up to ensure that the skull is completely clear. The exposed skull will be moistened with saline water throughout the measurement to maintain skull transparency. During the experiment, the mice will be enclosed in a homemade restraint kit [191] to minimize the movement.

B.3.2 Experimental setup

The setup of OISI system for imaging the exposed skull of mice with tPBM is shown in Figure B.3(a). The surface of interest will be sequentially illuminated with 470 nm, 530 nm, and 625 nm light using high-power collimator LED sources (LCS0470/0530/0625, Mightex, Toronto, ON). The reflected light will be collected using an EMCCD camera (iXon 888, Andor, UK) with an EF 50 mm f/1.2L lens (Canon, USA).

tPBM at multiple wavelengths, including 808 nm, 852 nm, and 1064 nm, will be applied globally over the whole exposed skull or locally at a specific location by noncontact delivery. Laser beam sizes of 12 mm and 1 mm will be utilized for global and local transcranial stimulation, respectively. Three tPBM light source power densities of 20, 50, and 100 mW/cm^2 will also be employed to investigate the differences in hemodynamic responses of the brain to tPBM. A general OISI-tPBM protocol is shown in Figure B.3(b). An example of the image obtained by the OISI for the moistened skull is also shown in Figure Figure B.3(c).

The data acquired at three wavelengths will be used to calculate the changes in hemoglobin concentrations (i.e., Δ[HbO] and Δ[Hb]). Such a calculation is based on the modified Beer-Lambert Law and was described in detail in [117]. The spatio-temporal hemodynamic signals obtained from the OISI system will be further analyzed locally to understand better the hemoglobin response of different compartment of the brain. Since both global and local tPBM stimulation will be applied to the mouse brain, the spatio-temporal information received from the OISI system also helps to understand better the effects of tPBM on the excitation region as well as the surrounding areas. Furthermore, thanks to the high spatial resolution of the OISI system, the functional connectivity (FC) of the mouse cortex can also be evaluated for different ISO frequency bands within three experimental periods to investigate further the neurovascular coherence under tPBM.

Appendix C

Matlab code

C.1 EEG data analysis using CorrCA method

C.1.1 Preprocessing using EEGLAB

```
%%%%%%%%%%%%%%%%%%%%%%%%%%%%%%%%%%%%%%%%%%%%%%%%%%%%%%%%%%%%%%%%%%%%%%%%%%%
% Preprocess EEG data using EEGLAB functions
%
% Preprocessing steps: Load raw data -> Import channel locations ->
% Re-reference -> Down-sample -> Remove DC offset -> Bandpass filter
%%%%%%%%%%%%%%%%%%%%%%%%%%%%%%%%%%%%%%%%%%%%%%%%%%%%%%%%%%%%%%%%%%%%%%%%%%%
clear
close all
clc

main_fd = uigetdir;
curr_fd = cd;

subj_list = 1:31;

eeglab

downsample_freq = 250;
nb_channel = 64;

for i_subj = subj_list
   sub_fd = [main_fd,'SUB',num2str(i_subj),filesep];
   filelist = dir([sub_fd,'*.bdf']);
   for i_exp = 1:length(filelist)
      EEG = pop_biosig([sub_fd,filelist(i_exp).name],...
         'channels',1:64);
      EEG = eeg_checkset( EEG );
      EEG=pop_chanedit(EEG, 'lookup',...
         [curr_fd,filesep,'standard_1005.elc'],...
         'load',[]);
      EEG = pop_reref( EEG, []);
      EEG = pop_resample( EEG, downsample_freq);
      EEG = pop_rmbase( EEG, [],[]);
```

```
      EEG = pop_eegfiltnew(EEG, 'locutoff',0.5,'hicutoff',58,...
         'plotfreqz',0);
      EEG = eeg_checkset( EEG );
      EEG.setname = 'reref_resample_rmbase_filt';
      pop_saveset(EEG,'filename',...
         [filelist(i_exp).name(1:end-4),'_filtered.set'],...
         'filepath',sub_fd);
   end
end
```

C.1.2 Inter-Subject Correlation Analysis

```
%%%%%%%%%%%%%%%%%%%%%%%%%%%%%%%%%%%%%%%%%%%%%%%%%%%%%%%%%%%%%%%%%%%%%%%%%%%
% Analyze the COBA dataset using Correlated Component Analysis method
% All subjects were considered at the same time to estimate the CorrCA
% space
% Inter-Subject Correlation analysis
%%%%%%%%%%%%%%%%%%%%%%%%%%%%%%%%%%%%%%%%%%%%%%%%%%%%%%%%%%%%%%%%%%%%%%%%%%%

clear
close all
clc

% pararmeters for loading EEG data
data_fd = uigetdir;
sub_name = 'sub';
freq_bands = {'Delta','Theta','Alpha','Beta','Gamma'};

subject_list = [1 3 4 6 7 9 10 12:14 16:19 21:24 26:30];

save_fd = uigetdir;
result_fd = 'CorrCA_COBA/';

if exist([save_fd result_fd],'dir')==0
   mkdir([save_fd result_fd])
end

nb_channels = 64;

% some ISC processing parameters
gamma = 0.1; % shrinkage parameter; smaller gamma for less regularization
Nsec = 1; % time-window (in seconds) over which to compute time-resolved ISC
Ncomp = 4; % number of components to display (all D are computed)
```

```matlab
Nscalp = 4; % number of scalp projections to display

Twin = 1; % time-window to estimate time-resolved power (in second)

% some parameters for preprocessing
kIQD=4; % multiple of interquartile differences to mark as outliers samples
kIQDp=3; % multiple of interquartile differences to mark as outliers channels
HPcutoff =0.5; % HP filter cut-off frequequency in Hz
debug = 0; % turn this on to show data before/after preprocessing.

nb_trials = 40;

%% load time data
time_stamp = [];
for i=1:length(subject_list)
   inputpath = strcat(data_fd,sub_name,num2str(subject_list(i)),'/');
   load([inputpath 'sub' num2str(subject_list(i)) '_time/Time_Stamp.mat']); % variable t_stamp
   time_stamp = [time_stamp;t_stamp(2:end,:)];
end

min_dcs = 5; % in second
min_r1 = 5;
min_fb = 10;
min_r2 = 5;

time_mark = [];
for ii = 1:nb_trials
   time_mark = [time_mark,(ii-1)*(min_dcs+min_r1+min_fb+min_r2)+1,...
      (ii-1)*(min_dcs+min_r1+min_fb+min_r2)+1+min_dcs,...
      (ii-1)*(min_dcs+min_r1+min_fb+min_r2)+1+min_dcs+min_r1,...
      (ii-1)*(min_dcs+min_r1+min_fb+min_r2)+1+min_dcs+min_r1+min_fb];
end

%% prepare data for CorrCA
for i=1:length(subject_list)
   inputpath = strcat(data_fd,sub_name,num2str(subject_list(i)),'/');
   inputname = ['ICA_' sub_name num2str(subject_list(i))];
   if exist([inputpath inputname '_v2.set'],'file')==2
      [EEG, command] = pop_loadset( [inputname '_v2.set'], inputpath);
   else
      [EEG, command] = pop_loadset( [inputname '.set'], inputpath);
   end
```

```
   fs = EEG.srate; % Sampling frequency
   % EEG.data [channels x time_samples]
   % In the case of all subjects with 40 trials, we need
   % X [time_samples x channels x subjects]
   data = double(EEG.data'); % time_samples x channels
   X_sub = [];
   for ii=1:nb_trials
      X_sub = [X_sub;data(time_stamp((i-1)*nb_trials+ii,1)*fs+1:...
         (time_stamp((i-1)*nb_trials+ii,1)+min_dcs)*fs,:);...
         data(time_stamp((i-1)*nb_trials+ii,2)*fs+1:...
         (time_stamp((i-1)*nb_trials+ii,2)+min_r1)*fs,:);...
         data(time_stamp((i-1)*nb_trials+ii,3)*fs+1:...
         (time_stamp((i-1)*nb_trials+ii,3)+min_fb)*fs,:);...
         data(time_stamp((i-1)*nb_trials+ii,4)*fs+1:...
         (time_stamp((i-1)*nb_trials+ii,4)+min_r2)*fs,:)];
   end

   X(:,:,i) = X_sub;

   X_baseline(:,:,i) = double(EEG.data(:,0*fs+1:30*fs))'; % nb_channel x nb_tsamples

end

%% Perform CorrCA method
% T samples, D channels, N subjects
[T,D,N] = size(X);

[W,ISC,A,ISC_persubject,ISC_persecond,ISC_persecond_subject] = corr_ca(X,Nsec,fs,gamma);

sname = sprintf('EEG_COBA_CorrCA_ISC_features_nbt_%d.mat',...
   nb_trials);
save(sname,'W','ISC','A','ISC_persubject','ISC_persecond',...
   'ISC_persecond_subject');

clear Y
for nn=1:N
   Y_baseline(:,:,nn) = X_baseline(:,:,nn)*W;
   Y(:,:,nn)=X(:,:,nn)*W; %Y [T x D x N]
end

% Estimate time-resolved power
```

```
band_power = EEG_power_bytime(Y,Twin,Ncomp,fs);
% band_power: nb_tslots x nb_subjects x nb_components x
% nb_freq_bands
baseline_power = EEG_power_bytime(Y_baseline,Twin,Ncomp,fs);

Y_baseline_4 = Y_baseline(:,1:4,:);
Y_4 = Y(:,1:4,:);

sname = sprintf('EEG_COBA_CorrCA_ISC_power_nbt_%d.mat',...
   nb_trials);
save(sname,'Y_4','Y_baseline_4','band_power','baseline_power');
```

```
function [W,ISC,A,ISC_persubject,ISC_persecond,ISC_persecond_subject] = corr_ca(X,Nsec,fs,gamma)
%%%%%%%%%%%%%%%%%%%%%%%%%%%%%%%%%%%%%%%%%%%%%%%%%%%%%%%%%%%%%%%%%%%%%%%%%%
% modified from the code provided by Dr. Parra and Dr. Dmochowski
% Original source code: https://www.parralab.org/corrca/
%%%%%%%%%%%%%%%%%%%%%%%%%%%%%%%%%%%%%%%%%%%%%%%%%%%%%%%%%%%%%%%%%%%%%%%%%%

if (nargin<4) % isempty(gamma)
   gamma = 0.1;
end


[T,D,N] = size(X);

% compute cross-covariance between all subjects i and j
Rij = permute(reshape(cov(X(:,:)),[D N D N]),[1 3 2 4]);

% compute within- and between-subject covariances
Rw = 1/N* sum(Rij(:,:,1:N+1:N*N),3); % pooled over all subjects
Rb = 1/(N-1)/N*(sum(Rij(:,:,:),3) - N*Rw); % pooled over all pairs of subjects

% shrinkage regularization of Rw
Rw_reg = (1-gamma)*Rw + gamma*mean(eig(Rw))*eye(size(Rw));

% compute correlated components W using regularized Rw, sort components by ISC
[W,ISC]=eig(Rb,Rw_reg);
[ISC,indx]=sort(diag(ISC),'descend');
W=W(:,indx);

% compute forward model (scalp projections) A
A=Rw*W/(W'*Rw*W);
```

```

% Compute ISC resolved by subject, see Cohen et al.
for ii=1:N
   Rw=0; Rb=0;
   for j=1:N
      if ii~=j
         Rw = Rw+1/(N—1)*(Rij(:,:,ii,ii)+Rij(:,:,j,j));
         Rb = Rb+1/(N—1)*(Rij(:,:,ii,j)+Rij(:,:,j,ii));
      end
   end
   ISC_persubject(:,ii) = diag(W'*Rb*W)./diag(W'*Rw*W);
end

% Compute ISC resolved in time / in time and by subject
for t = 1:floor((T—Nsec*fs)/fs)
   Xt = X((1:Nsec*fs)+(t—1)*fs,:,:);
   Rij = permute(reshape(cov(Xt(:,:)),[D N D N]),[1 3 2 4]);
   Rw = 1/N* sum(Rij(:,:,1:N+1:N*N),3); % pooled over all subjects
   Rb = 1/(N—1)/N*(sum(Rij(:,:,:),3) — N*Rw); % pooled over all pairs of subjects
   ISC_persecond(:,t) = diag(W'*Rb*W)./diag(W'*Rw*W);
   for i=1:N
      Rwn = 0; Rbn = 0;
      for j=1:N
         if i~=j
            Rwn = Rwn+1/(N—1)*(Rij(:,:,i,i)+Rij(:,:,j,j));
            Rbn = Rbn+1/(N—1)*(Rij(:,:,i,j)+Rij(:,:,j,i));
         end
      end
      ISC_persecond_subject(:,t,i) = diag(W'*Rbn*W)./diag(W'*Rwn*W);
   end
end
```

```
function [band_power,varargout] = EEG_power_bytime(EEG_signal,Twin,nb_cchan,fs,varargin)
%%%%%%%%%%%%%%%%%%%%%%%%%%%%%%%%%%%%%%%%%%%%%%%%%%%%%%%%%%%%%%%%%%%%%%%%%%%
% Calculate the time—resolved EEG power for different frequency bands
%
% Input:
% — EEG_signal [nb_samples x nb_channels/components x nb_subjects]
% — Twin: time window (in second)
% — nb_cchan: number of components to compute spectral power density
% — fs: sampling rate
% — baseline: vector containing the beginning and ending instants of baseline
```

```matlab
%
% Output: band_power [nb_tslot x nb_subjects x nb_cchan x nb_freq_band]
% baseline_power,norm_power
%%%%%%%%%%%%%%%%%%%%%%%%%%%%%%%%%%%%%%%%%%%%%%%%%%%%%%%%%%%%%%%%%%%%%%%%%%%%

nb_samples = size(EEG_signal,1);
nb_subjects = size(EEG_signal,3);
freq_bands = [1 4 8 13 30 60];

if length(varargin)==1
   baseline = varargin{1};

   for n=1:nb_subjects
      data = EEG_signal(baseline(1)*fs+1:baseline(2)*fs,1:nb_cchan,n)';

      % compute power spectrum of epoched data
      [spectra,freqs] = spectopo(data, 0, fs,'plot','off'); % power spectral density in dB

      % Set the following frequency bands: delta=1-4, theta=4-8, alpha=8-13, beta=13-30, gamma=30-60.
      for i_freq = 1:length(freq_bands)-1
         baseline_power(n,:,i_freq) = mean(...
            10.^(spectra(:,freqs>freq_bands(i_freq) &...
            freqs<freq_bands(i_freq+1))/10),2);
      end
   end
   varargout{1} = baseline_power;
end

for t = 1:ceil(nb_samples/fs/Twin)
   t_begin = (t-1)*fs*Twin+1;
   t_end = t*fs*Twin;
   for n=1:nb_subjects

      data = EEG_signal(t_begin:min(t_end,size(EEG_signal,1)),1:nb_cchan,n)';
      % compute power spectrum of epoched data
      [spectra,freqs] = spectopo(data, 0, fs,'plot','off');

      % Set the following frequency bands: delta=1-4, theta=4-8, alpha=8-13, beta=13-30, gamma=30-60.
      for i_freq = 1:length(freq_bands)-1
         band_power(t,n,:,i_freq) = mean(...
```

```
            10.^(spectra(:,freqs>freq_bands(i_freq) &...
            freqs<freq_bands(i_freq+1))/10),2);
      end
   end
   if length(varargin)==1
      norm_power(t,:,:,:) = band_power(t,:,:,:)./...
         reshape(baseline_power,size(band_power(t,:,:,:)));
   end
end
if length(varargin) == 1
   varargout{2} = norm_power;
end
```

C.1.3 Inter-Trial Correlation Analysis

```
%%%%%%%%%%%%%%%%%%%%%%%%%%%%%%%%%%%%%%%%%%%%%%%%%%%%%%%%%%%%%%%%%%%%%%%%%%%
% Analyze the COBA dataset using Correlated Component Analysis method
% All subjects were considered at the same time to estimate the CorrCA
% space
% Inter—Trial Correlation analysis
%%%%%%%%%%%%%%%%%%%%%%%%%%%%%%%%%%%%%%%%%%%%%%%%%%%%%%%%%%%%%%%%%%%%%%%%%%%

clear
close all
clc

% pararmeters for loading EEG data
data_fd = uigetdir;
sub_name = 'sub';
freq_bands = {'Delta','Theta','Alpha','Beta','Gamma'};

subject_list_org = [1 3 4 6 7 9 10 12:14 16:19 21:24 26:30];

nb_channels = 64;

% some ITC processing parameters
gamma = 0.1; % shrinkage parameter; smaller gamma for less regularization
Nsec = 1; % time—window (in seconds) over which to compute time—reposeved ISC
Ncomp = 4; % number of components to display (all D are computed)
Nscalp = 4; % number of scalp projections to display

Twin = 1; % time—window to estimate time—resolved power (in second)

```

```
% some parameters for preprocessing
kIQD=3; % multiple of interquartile differences to mark as outliers samples
kIQDp=4; % multiple of interquartile differences to mark as outliers channels
HPcutoff =0.5; % HP filter cut-off frequequency in Hz
debug = 0; % turn this on to show data before/after preprocessing.

nb_iter = 3;

start_trial = 1;

%% case Inter-Trial Correlation

min_dcs = 5; % in second
min_r1 = 5;
min_fb = 10;
min_r2 = 5;

nb_trial = 40;

for i=1:length(subject_list)
   inputpath = strcat(data_fd,sub_name,num2str(subject_list(i)),'/');
   load([inputpath 'sub' num2str(subject_list(i)) '_time/Time_Stamp.mat']); % variable t_stamp

   inputname = ['ICA_' sub_name num2str(subject_list(i))];
   if exist([inputpath inputname '_v2.set'],'file')==2
      [EEG, command] = pop_loadset( [inputname '_v2_rpca_fica_pruned.set'], inputpath);
   else
      [EEG, command] = pop_loadset( [inputname '_rpca_fica_pruned.set'], inputpath);
   end
   fs = EEG.srate; % Sampling frequency
   % EEG.data [channels x time_samples]
   % In the case of all subjects with 40 trials, we need
   % X [time_samples x channels x subjects]
   data = double(EEG.data'); % time_samples x channels
   X_sub = [];
   for i_trial=start_trial:(start_trial+nb_trial-1)
      ii = i_trial;%trial_ks_dcs(i_trial);
      X_sub = [X_sub;data(t_stamp(ii+1,1)*fs+1:(t_stamp(ii+1,1)+min_dcs)*fs,:);...
         data(t_stamp(ii+1,2)*fs+1:(t_stamp(ii+1,2)+min_r1)*fs,:);...
         data(t_stamp(ii+1,3)*fs+1:(t_stamp(ii+1,3)+min_fb)*fs,:);...
```

```matlab
         data(t_stamp(ii+1,4)*fs+1:(t_stamp(ii+1,4)+min_r2)*fs,:)];

   end

   X_org(:,:,i) = X_sub;

   X_baseline(:,:,i) = double(EEG.data(:,0*fs+1:30*fs))'; % nb_channel x nb_tsamples

end

X = permute(X_org,[2 3 1]);
% nb_channels x nb_subjects x nb_time_samples
X_trial = reshape(X,size(X,1),size(X,2),(min_dcs+min_r1+min_fb+min_r2)*fs,[]);
% nb_channels x nb_subjects x nb_time_samples (one trial) x nb_trials
X_ch_tr_ts_su = permute(X_trial,[1 4 3 2]);
% nb_channels x nb_trials x nb_time_samples (one trial) x nb_subjects
X_reshape = reshape(X_ch_tr_ts_su,size(X_ch_tr_ts_su,1),size(X_ch_tr_ts_su,2),...
   (size(X_ch_tr_ts_su,3)*size(X_ch_tr_ts_su,4)));
% nb_channels x nb_trials x (nb_time_samples (one trial) x nb_subjects)
X = permute(X_reshape,[3 1 2]);

% T samples, D channels, N subjects/trials
[T,D,N] = size(X);

[W,ISC,A,ISC_persubject,ISC_persecond,ISC_persecond_subject] = ...
   corr_ca_ITC(X,X_org,Nsec,fs,gamma);

sname = sprintf('EEG_COBA_CorrCA_ITC_features_strial_%d_nbt_%d.mat',...
   start_trial,nb_trial);
save(sname,'W','ISC','A','ISC_persubject','ISC_persecond',...
   'ISC_persecond_subject');


clear Y
for nn=1:size(X_org,3)
   Y_baseline(:,:,nn) = X_baseline(:,:,nn)*W;
   Y(:,:,nn)=X_org(:,:,nn)*W; %Y [T x D x N]
end

% Estimate time-resolved power
band_power = EEG_power_bytime(Y,Twin,Ncomp,fs);
% band_power: nb_tslots x nb_subjects x nb_components x
```

```
% nb_freq_bands
baseline_power = EEG_power_bytime(Y_baseline,Twin,Ncomp,fs);

Y_baseline_4 = Y_baseline(:,1:4,:);
Y_4 = Y(:,1:4,:);

sname = sprintf('EEG_COBA_CorrCA_ITC_power_strial_%d_nbt_%d.mat',...
   start_trial,nb_trial);
save(sname,'Y_4','Y_baseline_4','band_power','baseline_power');
```

```
function [W,ISC,A,ISC_persubject,ISC_persecond,ISC_persecond_subject]...
   = corr_ca_ITC(X,X_org,Nsec,fs,gamma)
%%%%%%%%%%%%%%%%%%%%%%%%%%%%%%%%%%%%%%%%%%%%%%%%%%%%%%%%%%%%%%%%%%%%%%%%%%
% modified from the code provided by Dr. Parra and Dr. Dmochowski for the
% case of Inter—Trial Correlation analysis
% Original source code: https://www.parralab.org/corrca/
%%%%%%%%%%%%%%%%%%%%%%%%%%%%%%%%%%%%%%%%%%%%%%%%%%%%%%%%%%%%%%%%%%%%%%%%%%

if (nargin<4) % isempty(gamma)
   gamma = 0.1;
end


[T,D,N] = size(X);

% compute cross—covariance between all trials i and j
Rij = permute(reshape(cov(X(:,:)),[D N D N]),[1 3 2 4]);

% compute within— and between—trial covariances
Rw = 1/N* sum(Rij(:,:,1:N+1:N*N),3); % pooled over all trials
Rb = 1/(N—1)/N*(sum(Rij(:,:,:),3) — N*Rw); % pooled over all pairs of trials

% shrinkage regularization of Rw
Rw_reg = (1—gamma)*Rw + gamma*mean(eig(Rw))*eye(size(Rw));

% compute correlated components W using regularized Rw, sort components by ISC
[W,ISC]=eig(Rb,Rw_reg);
[ISC,indx]=sort(diag(ISC),'descend');
W=W(:,indx);

% compute forward model (scalp projections) A
A=Rw*W/(W'*Rw*W);

```

```
% re—apply for the original signal
[T,D,N] = size(X_org);

% compute cross—covariance between all subjects i and j
Rij = permute(reshape(cov(X_org(:,:)),[D N D N]),[1 3 2 4]);

% compute within— and between—subject covariances
Rw = 1/N* sum(Rij(:,:,1:N+1:N*N),3); % pooled over all subjects
Rb = 1/(N—1)/N*(sum(Rij(:,:,:),3) — N*Rw); % pooled over all pairs of subjects

% Compute ISC resolved by subject, see Cohen et al.
for ii=1:N
   Rw=0; Rb=0;
   for j=1:N
      if ii~=j
         Rw = Rw+1/(N—1)*(Rij(:,:,ii,ii)+Rij(:,:,j,j));
         Rb = Rb+1/(N—1)*(Rij(:,:,ii,j)+Rij(:,:,j,ii));
      end
   end
   ISC_persubject(:,ii) = diag(W'*Rb*W)./diag(W'*Rw*W);
end

% Compute ISC resolved in time / in time and by subject
for t = 1:floor((T—Nsec*fs)/fs)
   Xt = X_org((1:Nsec*fs)+(t—1)*fs,:,:);
   Rij = permute(reshape(cov(Xt(:,:)),[D N D N]),[1 3 2 4]);
   Rw = 1/N* sum(Rij(:,:,1:N+1:N*N),3); % pooled over all subjects
   Rb = 1/(N—1)/N*(sum(Rij(:,:,:),3) — N*Rw); % pooled over all pairs of subjects
   ISC_persecond(:,t) = diag(W'*Rb*W)./diag(W'*Rw*W);
   for i=1:N
      Rwn = 0; Rbn = 0;
      for j=1:N
         if i~=j
            Rwn = Rwn+1/(N—1)*(Rij(:,:,i,i)+Rij(:,:,j,j));
            Rbn = Rbn+1/(N—1)*(Rij(:,:,i,j)+Rij(:,:,j,i));
         end
      end
      ISC_persecond_subject(:,t,i) = diag(W'*Rbn*W)./diag(W'*Rwn*W);
   end
end
```

C.1.4 Plotting ISC/ITC results

```matlab
%%%%%%%%%%%%%%%%%%%%%%%%%%%%%%%%%%%%%%%%%%%%%%%%%%%%%%%%%%%%%%%%%%%%%%%%%%
% Plot time—resolved ISC or ITC results
% Prepare ISC or ITC results for statistical analysis
%%%%%%%%%%%%%%%%%%%%%%%%%%%%%%%%%%%%%%%%%%%%%%%%%%%%%%%%%%%%%%%%%%%%%%%%%%
clear
close all
clc

%% parameters
save_fd = uigetdir;
result_fd = 'CorrCA_COBA/';

if exist([save_fd result_fd],'dir')==0
   mkdir([save_fd result_fd])
end

nb_components = 3; % number of CorrCA components

min_dcs = 5; % duration of task periods in second
min_r1 = 5;
min_fb = 10;
min_r2 = 5;

time_mark = [0 min_dcs min_dcs+min_r1 ...
   min_dcs+min_r1+min_fb min_dcs+min_r1+min_fb+min_r2];
time_mark_period = [1 5; 6 10; 11 20; 21 25];

nb_cum_comp = [3 10 30 40];
% number of CorrCA components to calculate the cumulative ISC/ITC

subject_list_type = [1 0; 3 0; 4 0; 6 0; 7 1; 9 0; 10 1; 12 1; 13 1;...
   14 1; 16 0; 17 1; 18 0; 19 1; 21 1; 22 0; 23 0; 24 0; ...
   26 1; 27 0; 28 0; 29 1; 30 1];
% subject list and the corresponding experimental group (0: LM, 1: HM)
subject_list = subject_list_type(:,1);
subject_test_type = subject_list_type(:,2);

% parameters for plotting
typeplot = {'r','b','g','m','k'};
violin_style = 0;
f_alpha = 0.5;
color_violin = [1 0 0; 0 0 1; 0 1 0];
test_type = {'LM','HM'};
```

```

%% load CorrCA results
anal_type = 'ISC'; % CorrCA analysis type: ISC or ITC
fname = ['EEG_COBA_CorrCA_',anal_type,'_features_nbt_',...
   num2str(nb_trials),'.mat'];

load(fname)

%% ISC curve - Low high margin - First k components
nb_trials = floor(size(ISC_persecond,2)/time_mark(end));

ISC_time_subj_temp = permute(...
   ISC_persecond_subject(:,1:time_mark(end)*(nb_trials),:),[1 3 2]);
% ISC_time_subj_temp: nb_comp x nb_subj x nb_tslots (excluding the last
% trial)

ISC_time_subj_temp = reshape(ISC_time_subj_temp,...
   size(ISC_time_subj_temp,1),size(ISC_time_subj_temp,2),...
   time_mark(end),[]);
% ISC_time_subj_temp: nb_comp x nb_subj x trial_duration x nb_trials

ISC_txs{1} = mean(ISC_time_subj_temp,4); % all trials
ISC_txs{2} = mean(ISC_time_subj_temp(:,:,:,1:20),4); % first 20 trials
ISC_txs{3} = mean(ISC_time_subj_temp(:,:,:,21:end),4); % last 20 trials

for i_nb_cum = 1:nb_components % CorrCA components
   for ii=1:3 % type of trials
      for jj=1:2 % low high margin
         ISC_txs_lh{ii,jj,i_nb_cum} = permute(...
            ISC_txs{ii}(i_nb_cum,...
            subject_test_type==(jj-1),:),[3 2 1]);
         for i_period = 1:size(time_mark_period,1)
            mean_time_ISC{ii,jj,i_period,i_nb_cum} = ...
               mean(ISC_txs_lh{ii,jj,i_nb_cum}(...
               time_mark_period(i_period,1):...
               time_mark_period(i_period,2),:),1);
            if i_nb_cum == 1
               cum_mean_time_ISC{ii,jj,i_period} = ...
                  mean(ISC_txs_lh{ii,jj,i_nb_cum}(...
                  time_mark_period(i_period,1):...
                  time_mark_period(i_period,2),:),1);
            else
               cum_mean_time_ISC{ii,jj,i_period} = ...
```

```
                  cum_mean_time_ISC{ii,jj,i_period} + ...
                  mean(ISC_txs_lh{ii,jj,i_nb_cum}(...
                  time_mark_period(i_period,1):...
                  time_mark_period(i_period,2),:),1);
            end
         end
      end
      for i_sec = 1:size(ISC_txs_lh{ii,jj,i_nb_cum},1)
         TF_lm = isoutlier(ISC_txs_lh{ii,1,i_nb_cum}(i_sec,:)',...
            'quartiles'); % find the outlier data
         TF_hm = isoutlier(ISC_txs_lh{ii,2,i_nb_cum}(i_sec,:)',...
            'quartiles');
         [h_ISC_cum_lh(i_sec,ii,i_nb_cum),...
            p_ISC_cum_lh(i_sec,ii,i_nb_cum)] = ...
            ttest2(ISC_txs_lh{ii,1,i_nb_cum}(i_sec,TF_lm==0)',...
            ISC_txs_lh{ii,2,i_nb_cum}(i_sec,TF_hm==0)');
         [p_rs_ISC_cum_lh(i_sec,ii,i_nb_cum),...
            h_rs_ISC_cum_lh(i_sec,ii,i_nb_cum)] = ...
            ranksum(ISC_txs_lh{ii,1,i_nb_cum}(i_sec,TF_lm==0)',...
            ISC_txs_lh{ii,2,i_nb_cum}(i_sec,TF_hm==0)');

         mean_ISC(i_sec,1,i_nb_cum) = ...
            mean(ISC_txs_lh{ii,1,i_nb_cum}(i_sec,TF_lm==0));
         mean_ISC(i_sec,2,i_nb_cum) = ...
            mean(ISC_txs_lh{ii,2,i_nb_cum}(i_sec,TF_hm==0));
         error_ISC(i_sec,1,i_nb_cum) = ...
            std(ISC_txs_lh{ii,1,i_nb_cum}(i_sec,TF_lm==0))/...
            sqrt(size(ISC_txs_lh{ii,1,i_nb_cum}(i_sec,TF_lm==0),2));
         error_ISC(i_sec,2,i_nb_cum) = ...
            std(ISC_txs_lh{ii,2,i_nb_cum}(i_sec,TF_hm==0))/...
            sqrt(size(ISC_txs_lh{ii,2,i_nb_cum}(i_sec,TF_hm==0),2));
      end
   end
end
% ISC_txs_lh: trial_duration x nb_subj

%% create data table for statistical analysis in R
for i_comp = 1:3
   all_tt_comp = [];
   for i_lh = 1:size(mean_time_ISC,2)
      clear ttt
      for i_period = 1:size(mean_time_ISC,3)
         ttt(:,i_period) = mean_time_ISC{1,i_lh,i_period,i_comp};
```

```
      end
      all_tt_comp = [all_tt_comp ttt(:)'];
   end

   g1 = [repmat({'dcs'},1,12),repmat({'r1'},1,12),...
      repmat({'fb'},1,12),repmat({'r2'},1,12),...
      repmat({'dcs'},1,11),repmat({'r1'},1,11),...
      repmat({'fb'},1,11),repmat({'r2'},1,11)];
   g2 = [repmat({'lm'},1,48),repmat({'hm'},1,44)];
   g3 = [repmat(1:12,[1 4]) repmat(13:13+10,[1 4])];
   T = table(g3',all_tt_comp',g1',g2',...
      'VariableNames',{'Subj','ISC','Phase','Test'});
end

%% statistical analysis of cumulative ISC or ITC
for i_period = 1:size(mean_time_ISC,3)-1
   for j_period = i_period+1:size(mean_time_ISC,3)
      [h_period_LM(i_period,j_period),...
         p_period_LM(i_period,j_period)] = ...
         ttest2(cum_mean_time_ISC{1,1,i_period},...
         cum_mean_time_ISC{1,1,j_period});
      [h_period_HM(i_period,j_period),...
         p_period_HM(i_period,j_period)] = ...
         ttest2(cum_mean_time_ISC{1,2,i_period},...
         cum_mean_time_ISC{1,2,j_period});
   end
end

for i_period = 1:size(mean_time_ISC,3)
   [h_lh(i_period),p_lh(i_period)] = ...
      ttest2(cum_mean_time_ISC{1,1,i_period},...
      cum_mean_time_ISC{1,2,i_period});

   [prs_lh(i_period),hrs_lh(i_period)] = ...
      ranksum(cum_mean_time_ISC{1,1,i_period},...
      cum_mean_time_ISC{1,2,i_period});

   for i_lh = 1:size(mean_time_ISC,2)
      mmean_ISC(i_lh,i_period) = mean(cum_mean_time_ISC{1,i_lh,i_period});
      err_ISC(i_lh,i_period) = std(cum_mean_time_ISC{1,i_lh,i_period})/...
         sqrt(length(cum_mean_time_ISC{1,i_lh,i_period}));

      for i_comp = 1:size(mean_time_ISC,4)
```

```
         mmean_ISC_comp(i_lh,i_period,i_comp) = mean(mean_time_ISC{1,i_lh,i_period,i_comp});
         err_ISC_comp(i_lh,i_period,i_comp) = std(mean_time_ISC{1,i_lh,i_period,i_comp})/...
            sqrt(length(mean_time_ISC{1,i_lh,i_period,i_comp}));
      end
   end
end

%% === ISC 3 components — barplot ===
figure(1);
for i_comp = 1:size(mmean_ISC_comp,3)
   subplot(1,3,i_comp)
   bar(0.88:1:3.88,mmean_ISC_comp(1,:,i_comp),0.2,'FaceColor','r');
   hold on
   p=errorbar(0.88:1:3.88,mmean_ISC_comp(1,:,i_comp),...
      err_ISC_comp(1,:,i_comp),'k','LineStyle','none');
   set(get(get(p,'Annotation'),'LegendInformation'),...
      'IconDisplayStyle','off');

   bar(1.12:1:4.12,mmean_ISC_comp(2,:,i_comp),0.2,'FaceColor','b');
   hold on
   p=errorbar(1.12:1:4.12,mmean_ISC_comp(2,:,i_comp),...
      err_ISC_comp(2,:,i_comp),'k','LineStyle','none');
   set(get(get(p,'Annotation'),'LegendInformation'),...
      'IconDisplayStyle','off');

   xlim([0.5 4.5])
   set(gca,'XTick',[1 2 3 4]);
   set(gca,'XTickLabel',{'DCS','R1','FB','R2'});

   xlabel('Experimental period');
   if i_comp==1
      ylabel(anal_type);
   end
   title(['Component ',num2str(i_comp)]);
end
legend('LM (n=12)','HM (n=11)','Location','Best',...
   'Orientation','Horizontal');

%% === cummulative ISC/ITC ===
figure(2);
bar(0.88:1:3.88,mmean_ISC(1,:),0.2,'FaceColor','r');
```

```
hold on
p=errorbar(0.88:1:3.88,mmean_ISC(1,:),err_ISC(1,:),'k','LineStyle','none');
set(get(get(p,'Annotation'),'LegendInformation'),...
   'IconDisplayStyle','off');

bar(1.12:1:4.12,mmean_ISC(2,:),0.2,'FaceColor','b');
hold on
p=errorbar(1.12:1:4.12,mmean_ISC(2,:),err_ISC(2,:),'k','LineStyle','none');
set(get(get(p,'Annotation'),'LegendInformation'),...
   'IconDisplayStyle','off');

xlim([0.5 4.5])
xticks([1 2 3 4]);
xticklabels({'DCS','R1','FB','R2'})
xlabel('Experimental period');
ylabel(['Cumulative ',anal_type]);
legend('LM (n=12)','HM (n=11)','Location','Best',...
   'Orientation','Horizontal');

%% ISC curve - Low high margin - Cum. components

ISC_time_subj_temp = permute(...
   ISC_persecond_subject(:,1:time_mark(end)*(nb_trials-1),:),[1 3 2]);
% ISC_time_subj_temp: nb_comp x nb_subj x nb_tslots (excluding the last
% trial)

ISC_time_subj_temp = reshape(ISC_time_subj_temp,...
   size(ISC_time_subj_temp,1),size(ISC_time_subj_temp,2),...
   time_mark(end),[]);
% ISC_time_subj_temp: nb_comp x nb_subj x trial_duration x nb_trials

ISC_txs{1} = mean(ISC_time_subj_temp,4); % all trials
ISC_txs{2} = mean(ISC_time_subj_temp(:,:,:,1:25),4); % first 20 trials
ISC_txs{3} = mean(ISC_time_subj_temp(:,:,:,21:end),4); % last 20 trials

for i_nb_cum = 1:length(nb_cum_comp)
   for ii=1:3 % type of trials
      for jj=1:2 % low high margin
         ISC_txs_lh{ii,jj,i_nb_cum} = permute(...
            sum(ISC_txs{ii}(1:nb_cum_comp(i_nb_cum),...
            subject_test_type==(jj-1),:),1),[3 2 1]);
      end
      for i_sec = 1:size(ISC_txs_lh{ii,jj,i_nb_cum},1)
```

```
         [h_ISC_cum_lh(i_sec,ii,i_nb_cum),...
            p_ISC_cum_lh(i_sec,ii,i_nb_cum)] = ...
            ttest2(ISC_txs_lh{ii,1,i_nb_cum}(i_sec,:)',...
            ISC_txs_lh{ii,2,i_nb_cum}(i_sec,:)');
         [p_rs_ISC_cum_lh(i_sec,ii,i_nb_cum),...
            h_rs_ISC_cum_lh(i_sec,ii,i_nb_cum)] = ...
            ranksum(ISC_txs_lh{ii,1,i_nb_cum}(i_sec,:)',...
            ISC_txs_lh{ii,2,i_nb_cum}(i_sec,:)');
      end
   end
end
% ISC_txs_lh: trial_duration x nb_subj

figure(3);
i_trial_type = 1;
for i_nb_cum = 1:length(nb_cum_comp)
   for i_lh = 1:2
      if violin_style == 1
         violin(ISC_txs_lh{i_trial_type,i_lh}',...
            'x',1:size(ISC_txs_lh{i_trial_type,i_lh},1),...
            'facecolor',repmat(color_violin(i_lh,:),...
            size(ISC_txs_lh{i_trial_type,i_lh},1),1),...
            'facealpha',f_alpha,...
            'edgecolor','none',...
            'bw',0.1,'mc','k','medc','r-.',...
            'plotlegend',0);
         hold on
      else
         mean_ISC(:,i_lh) = mean(ISC_txs_lh{i_trial_type,i_lh,i_nb_cum},2);
         std_ISC(:,i_lh) = std(ISC_txs_lh{i_trial_type,i_lh,i_nb_cum},0,2)/...
            sqrt(size(ISC_txs_lh{i_trial_type,i_lh,i_nb_cum},2));

         plot(mean_ISC(:,i_lh),typeplot{i_lh},'LineWidth',2);
         hold on
         pp=errorbar(mean_ISC(:,i_lh),std_ISC(:,i_lh),typeplot{i_lh});
         set(get(get(pp,'Annotation'),'LegendInformation'),'IconDisplayStyle','off');
         if i_lh == 2
            temp = max(mean_ISC,[],2)+0.0015;
            plot(find(p_ISC_cum_lh(:,1,i_nb_cum)<0.09),...
               temp(p_ISC_cum_lh(:,1,i_nb_cum)<0.09),'k*','MarkerSize',8);
         end
      end
```

```
   end
   vline([1 min_dcs+1 (min_dcs + min_r1+1) (min_dcs + min_r1+min_fb+1)],...
      {'m' 'm' 'm' 'm'},{'DCS' 'R1' 'FB' 'R2'},0.05);
   xlabel('Time (s)');
   ylabel(anal_type);
   legend({'LM (n=12)','HM (n=11)'},'Location','NorthEast');
end

title(['Cumulative ',anal_type]);

if violin_style==1
   annotation('rectangle',[0.7 .974 .03 .003],'FaceColor','red',...
      'FaceAlpha',f_alpha,'LineStyle','none');
   annotation('textbox', [0.73,0.99, 0.2, 0], ...
      'string', 'Low margin',...
      'HorizontalAlignment','left','LineStyle','none','Color',[0 0 0],...
      'FontWeight','bold','FontSize',11,...
      'FitBoxToText','on')

   annotation('rectangle',[0.8 .974 .03 .003],'FaceColor','blue',...
      'FaceAlpha',f_alpha,'LineStyle','none');
   annotation('textbox', [0.83,0.99, 0.2, 0], ...
      'string', 'High margin',...
      'HorizontalAlignment','left','LineStyle','none','Color',[0 0 0],...
      'FontWeight','bold','FontSize',11,...
      'FitBoxToText','on')
end
```

C.1.5 Plotting PSD of CorrCA projection components

```
%%%%%%%%%%%%%%%%%%%%%%%%%%%%%%%%%%%%%%%%%%%%%%%%%%%%%%%%%%%%%%%%%%%%%%%%%%%
% Plot averaged PSD of 3 CorrCA projection components for 4 task periods
%%%%%%%%%%%%%%%%%%%%%%%%%%%%%%%%%%%%%%%%%%%%%%%%%%%%%%%%%%%%%%%%%%%%%%%%%%%
eeglab
clear
close all
clc

% initial pararmeters
min_dcs = 5; % in second
min_r1 = 5;
min_fb = 10;
min_r2 = 5;
```

```

nb_comp = 3;

save_fd = uigetdir; % main folder to save results
result_fd = 'CorrCA_COBA_PSD/';

if exist([save_fd result_fd],'dir')==0
   mkdir([save_fd result_fd])
end

%% load EEG data
data_fd = uigetdir; % EEG data folder
sub_name = 'sub';
inputpath = strcat(data_fd,sub_name,'1/');
inputname = 'ICA_sub1.set';
[EEG, command] = pop_loadset( inputname, inputpath);

%% load CorrCA results
anal_type = 'ISC'; % CorrCA analysis type: ISC or ITC
fname = ['EEG_COBA_CorrCA_',anal_type,'_features_nbt_',...
   num2str(nb_trials),'.mat'];

corrca_res=load(fname);

%% PSD
cl_list = {'r-','b-','m-','g-'};

figure(1);

nb_samples = size(corrca_res.Y_4,1);
nb_samples_bl = size(corrca_res.Y_baseline_4,1);
Twin = 1; % sec
fs = EEG.srate;
freq_range = 1:61;
for i_comp = 1:nb_comp
   all_spectra = [];
   all_spectra_bl = [];
   for i_subj = 1:size(corrca_res.Y_4,3)
      for i_t = 1:ceil(nb_samples/fs/Twin)
         t_begin = (i_t-1)*fs*Twin+1;
         t_end = i_t*fs*Twin;

         proj_comp = corrca_res.Y_4(:,i_comp,i_subj);
```

```
         data = proj_comp(t_begin:min(t_end,size(proj_comp,1)))';
         [spectra,freqs] = spectopo(data, 0, EEG.srate,'plot','off');
         all_spectra(:,i_t,i_subj) = spectra(freq_range);
         % freq x time x subj
      end
   end

   % original spectra
   tt = reshape(all_spectra,size(all_spectra,1),...
      (min_dcs+min_r1+min_fb+min_r2),...
      size(all_spectra,2)/(min_dcs+min_r1+min_fb+min_r2),...
      size(all_spectra,3));
   tt_dcs = squeeze(mean(mean(tt(:,1:5,:,:),2),3));
   tt_r1 = squeeze(mean(mean(tt(:,6:10,:,:),2),3));
   tt_fb = squeeze(mean(mean(tt(:,11:20,:,:),2),3));
   tt_r2 = squeeze(mean(mean(tt(:,21:25,:,:),2),3));

   subplot(1,3,i_comp)
   plot(freqs(freq_range),...
      mean(tt_dcs,2),...
      cl_list{1},'LineWidth',1.5)
   hold on
   plot(freqs(freq_range),...
      mean(tt_r1,2),...
      cl_list{2},'LineWidth',1.5)
   plot(freqs(freq_range),...
      mean(tt_fb,2),...
      cl_list{3},'LineWidth',1.5)
   plot(freqs(freq_range),...
      mean(tt_r2,2),...
      cl_list{4},'LineWidth',1.5)

   shadedErrorBar(freqs(freq_range),...
      mean(tt_dcs,2),...
      std(tt_dcs,[],2)/sqrt(size(tt_dcs,2)),...
      'lineprops', {cl_list{1},'LineWidth',0.5},...
      'transparent',1);

   shadedErrorBar(freqs(freq_range),...
      mean(tt_r1,2),...
      std(tt_r1,[],2)/sqrt(size(tt_r1,2)),...
      'lineprops', {cl_list{2},'LineWidth',0.5},...
      'transparent',1);
```

```

   shadedErrorBar(freqs(freq_range),...
      mean(tt_fb,2),...
      std(tt_fb,[],2)/sqrt(size(tt_fb,2)),...
      'lineprops', {cl_list{3},'LineWidth',0.5},...
      'transparent',1);

   shadedErrorBar(freqs(freq_range),...
      mean(tt_r2,2),...
      std(tt_r2,[],2)/sqrt(size(tt_r2,2)),...
      'lineprops', {cl_list{4},'LineWidth',0.5},...
      'transparent',1);

   ylim([—10 3])
   ylimits = get(gca,'YLim');
   plot([4 4],ylimits,'k:','LineWidth',1.5);
   plot([8 8],ylimits,'k:','LineWidth',1.5);
   plot([13 13],ylimits,'k:','LineWidth',1.5);
   plot([30 30],ylimits,'k:','LineWidth',1.5);

   xlim([0 60]);
   xlabel('Frequency (Hz)');
   ylabel('PSD (dB)');
   xticks([0 4 8 13 30 60]);
   title(['ISC Component ',num2str(i_comp)]);
   legend({'DCS','R1','FB','R2'});
end
```

C.2 fNIRS data analysis

C.2.1 Preprocessing using Homer2 functions

```
%%%%%%%%%%%%%%%%%%%%%%%%%%%%%%%%%%%%%%%%%%%%%%%%%%%%%%%%%%%%%%%%%%%%%%%%%%
% Preprocess fNIRS data using Homer2 functions
% Preprocessing steps: Intensity to optical density —> Optical density to
% changes in hemoglobin concentration —> Baseline detrending —> Lowpass
% filtering —> Motion artifact correction using PCA
%%%%%%%%%%%%%%%%%%%%%%%%%%%%%%%%%%%%%%%%%%%%%%%%%%%%%%%%%%%%%%%%%%%%%%%%%%
clear
close all
clc

main_fd = uigetdir; % folder for fNIRS data
```

```
exp_type = {'PBO','TRT'};

msave_fd = uigetdir; % folder for saving preprocessed data

nb_subject = 19;
detrend_order = 1; % detrending order
f_lp = 2; % low-pass frequency cutoff
f_hp = 0; % high-pass frequency cutoff
freq_band = 'LPF_2';
nb_PCA_comp = 2; % number of excluded PCA components

load('SD_for_Homer.mat');

for i_exp = 1:length(exp_type)
   for i_subj = 1:nb_subject
      load([main_fd,exp_type{i_exp},...
         '/',exp_type{i_exp},'_sub',...
         num2str(i_subj),'.mat']);

      fs = nirs_data.fs;
      nb_samples = size(nirs_data.oxyData,1);
      t = 1/fs:1/fs:nb_samples/fs;
      tIncMan = true(length(t),1);

      clear v
      v(:,:,1) = nirs_data.oxyData;
      v(:,:,2) = nirs_data.dxyData;
      v(:,:,3) = nirs_data.tHbData;

      dod = hmrIntensity2OD(v(:,:)); % intensity to OD
      dodWavelet = hmrMotionCorrectWavelet(dod,SD,1.5);

      dc = hmrOD2Conc(dod,SD,[6 6 6]); % OD to concentration changes

      % === detrend only baseline ===
      t_min = 8;
      sample_bsl = min(round(t_min*60*fs),nb_samples);
      clear detrend_dc
      for i = 1:3
         detrend_dc(:,i,:) = ...
            detrend_baseline(squeeze(dc(:,i,:)),...
            sample_bsl,detrend_order);
      end
```

```
      % === detrend only baseline ===
      dc = detrend_dc;

      dc = hmrBandpassFilt(dc,fs,f_hp,f_lp); % filtering

      [dc,svs,nSV] = hmrMotionCorrectPCA(SD,...
         dc,tIncMan,nb_PCA_comp); % Motion artifact correction

   end
   nirsdata.oxyData = squeeze(dc(:,1,:));
   nirsdata.dxyData = squeeze(dc(:,2,:));
   nirsdata.totalData = squeeze(dc(:,3,:));
   nirsdata.T = t;
   nirsdata.s = zeros(nb_samples,3);
   nirsdata.s(1,1) = 1;
   nirsdata.s(round(8*60*fs),2) = 1;
   nirsdata.s(round(16*60*fs),3) = 1;

   save_fd = [msave_fd,...
      freq_band,'/',exp_type{i_exp},'/'];
   if ~isfolder(save_fd)
      mkdir(save_fd)
   end
   save([save_fd,'preprocessing_',...
      save_name{i_method},'_',...
      exp_type{i_exp},'_sub_',...
      num2str(i_subj,'%02d'),'.mat'],...
      'nirsdata');
end

function v_detrend = detrend_baseline(v,sample_bsl,detrend_order)

for i_ch = 1:size(v,2)
   pp = polyfit((1:sample_bsl)',...
      v(1:sample_bsl,i_ch),detrend_order);
   base_oxy=polyval(pp,1:size(v,1));
   v_detrend(:,i_ch)=v(:,i_ch)-base_oxy'+mean(v(:,i_ch));
end
end
```

C.2.2 Perform the cluster-based permutation test on the whole-head time-resolved Δ[HbO] signals of tPBM and sham sessions

```
%%%%%%%%%%%%%%%%%%%%%%%%%%%%%%%%%%%%%%%%%%%%%%%%%%%%%%%%%%%%%%%%%%%%%%%%%%
% Perform the cluster-based permutation test on the whole-head
% time-resolved dHbO signals of tPBM and sham sessions
% Using functions from the Fieldtrip toolbox
%%%%%%%%%%%%%%%%%%%%%%%%%%%%%%%%%%%%%%%%%%%%%%%%%%%%%%%%%%%%%%%%%%%%%%%%%%
clear
close all
clc

% load template fNIRS data prepared to adapt with the required data format
% in Fieldtrip
load('template_data_fnirs_for_fieldtrip.mat')

dHbO_permin_PBO.label = temp_data_fnirs.label;
dHbO_permin_PBO.dimord = 'rpt_chan_freq_time';
dHbO_permin_PBO.freq = 0.2;
dHbO_permin_PBO.time = 9:20;
dHbO_permin_PBO.elec = temp_data_fnirs.elec;
dHbO_permin_TRT = dHbO_permin_PBO;

% Load the normalized averaged 1-min dHbO time-series
load('norm_dHbO_permin_PBO_TRT_bsl_30s_17subj.mat')

temp = permute(squeeze(norm_dHbO(:,:,:,1)),[3,2,4,1]);
dHbO_permin_PBO.powspctrm = temp(:,:,:,:);

temp = permute(squeeze(norm_dHbO(:,:,:,2)),[3,2,4,1]);
dHbO_permin_TRT.powspctrm = temp(:,:,:,:);

% Prepare neighbour channels for spatial clustering
cfg_neighb.method = 'distance';
cfg_neighb.neighbourdist = 25;
neighbours = ft_prepare_neighbours(cfg_neighb, temp_data_fnirs);

% Cluster-based permutation test
cfg = [];
cfg.channel = 'all';
cfg.frequency = 0.2;
cfg.method = 'montecarlo';
cfg.statistic = 'ft_statfun_indepsamplesT';
cfg.correctm = 'cluster';
cfg.clusteralpha = 0.05;
cfg.clusterthreshold = 'parametric';
```

```
cfg.clusterstatistic = 'maxsum';
cfg.minnbchan = 1;
cfg.tail = 0;
cfg.clustertail = 0;
cfg.alpha = 0.05;
cfg.numrandomization = 2000;
cfg.correcttail = 'alpha';
cfg.neighbours = neighbours;

design = zeros(1,size(dHbO_permin_PBO.powspctrm,1) + ...
   size(dHbO_permin_TRT.powspctrm,1));
design(1,1:size(dHbO_permin_TRT.powspctrm,1)) = 1;
design(1,(size(dHbO_permin_TRT.powspctrm,1)+1):...
   (size(dHbO_permin_PBO.powspctrm,1)+...
   size(dHbO_permin_TRT.powspctrm,1))) = 2;
cfg.design = design;
cfg.ivar = 1;

[stat] = ft_freqstatistics(cfg, dHbO_permin_TRT, dHbO_permin_PBO);

save('CBPT_dHbO_time_domain.mat','stat');
```

C.2.3 Calculate changes in Δ[HbO] power of three ISO oscillations

```
%%%%%%%%%%%%%%%%%%%%%%%%%%%%%%%%%%%%%%%%%%%%%%%%%%%%%%%%%%%%%%%%%%%%%%%%%%
% Calculate changes in dHbO power of three infra−slow oscillation
% Endogenic (0.003 − 0.02 Hz)
% Neurogenic (0.02 − 0.04 Hz)
% Myogenic (0.04 − 0.15 Hz)
%%%%%%%%%%%%%%%%%%%%%%%%%%%%%%%%%%%%%%%%%%%%%%%%%%%%%%%%%%%%%%%%%%%%%%%%%%
clear
close all
clc

main_fd = uigetdir;

% declare the interested ISO frequency band
freq_band = 'endo'; % 'neuro','myo'
data_type = {'PBO','TRT'};

% load one sample data
file_list = dir([main_fd,freq_band,'/',data_type{1},'/*.mat']);
load([main_fd,freq_band,'/',data_type{1},'/',file_list(1).name]);
```

```matlab

% get some necessary parameters
fs = 1/nirsdata.T(1);
nb_channel = size(nirsdata.oxyData,1);

pre_s = floor(8*60*fs);
subs_dur = 0.5*60;

t_min = ((0:pre_s*2.5-1)/fs)/60;

coi_bl = 1;
Twin = 4*60;
nb_cchan = 10;

for i_exp = 1:length(data_type)
   file_list = dir([main_fd,freq_band,'/',data_type{i_exp},'/*.mat']);
   sub_count = 1;
   for i_sub = [1 3:17 19]
      % load preprocessed dHbO signals
      load([main_fd,freq_band,'/',data_type{i_exp},'/',file_list(i_sub).name]);

      dHbO = nirsdata.oxyData*1e6;
      if size(dHbO,1)<pre_s*2.5
         dHbO = [dHbO;zeros(pre_s*2.5-size(dHbO,1),size(dHbO,2))];
      end
      mean_bsl_dHbO = mean(dHbO(pre_s-floor(subs_dur*fs)+1:pre_s,:),1);
      norm_dHbO(:,:,i_sub,i_exp) = dHbO(1:pre_s*2.5,:)-mean_bsl_dHbO;

      fNIRS_signal = norm_dHbO(:,:,i_sub,i_exp);
      nb_samples = size(fNIRS_signal,1);

      % Calculate the Welch power
      for i_t = 1:ceil(nb_samples/fs/Twin)
         t_begin = round((i_t-1)*fs*Twin+1);
         t_end = round(i_t*fs*Twin);

         data = fNIRS_signal(t_begin:min(t_end,size(fNIRS_signal,1)),...
            1:nb_cchan)';
         if size(data,2)<fix(fs*Twin)
            data = [data,zeros(size(data,1),fix(fs*Twin)-size(data,2))];
         end
         for i_channel = 1:nb_cchan
            [spectra(:,i_channel,i_t,sub_count,i_exp),f] = ...
```

```
          pwelch(data(i_channel,:),...
          fix(Twin/4*fs),0.5*fix(Twin/4*fs),fix(Twin*fs),fs,'power');
      end
    end
    sub_count = sub_count + 1;
  end
end

all_psd_org = permute(spectra,...
  [4 2 1 3 5]);

%% === plot percentage change ===
freq_list = [0.003 0.02;0.02 0.04;0.04 0.2];

freq_idx = reshape( dsearchn(f,freq_list(:)), [],2);

all_psd = sqrt(all_psd_org);
mean_psd_freq = zeros(size(all_psd,1),size(all_psd,2),...
  size(freq_idx,1),size(all_psd,4),size(all_psd,5));

for i_freq = 1:size(freq_idx,1)
  mean_psd_freq(:,:,i_freq,:,:) = sqrt(nanmean(...
    all_psd(:,:,freq_idx(i_freq,1):freq_idx(i_freq,2),:,:),3));
end

diff_psd = 100*(mean_psd_freq - repmat(...
  mean_psd_freq(:,:,:,2,:),[1 1 1 size(all_psd,4) 1]))./...
  repmat(...
  mean_psd_freq(:,:,:,2,:),[1 1 1 size(all_psd,4) 1]);

f1=figure(2);
clf(f1)
channel_list = [3 4 7];

phase_list = {'Pre1','Pre2','Stim1','Stim2','Post'};
count = 1;

for i_channel = channel_list

  for i_phase = 3:size(all_psd,4)
    subplot(size(all_psd,4)-2,length(channel_list),...
      count+(i_phase-3)*length(channel_list))

```

```
      [h,pp] = ttest(squeeze(diff_psd(:,i_channel,:,i_phase,2)),...
         squeeze(diff_psd(:,i_channel,:,i_phase,1)));
      pp_all(:,i_phase,count) = pp;

      temp1 = squeeze(nanmean(diff_psd(:,i_channel,:,i_phase,2),1));
      temp_er1 = squeeze(nanstd(diff_psd(:,i_channel,:,i_phase,2),1)/...
         sqrt(size(all_psd,1)));
      bar(0.9:1:2.9,temp1,0.2,'FaceColor','r');
      hold on
      errorbar(0.9:1:2.9,temp1,temp_er1,'k','LineStyle','none');

      temp2 = squeeze(nanmean(diff_psd(:,i_channel,:,i_phase,1),1));
      temp_er2 = squeeze(nanstd(diff_psd(:,i_channel,:,i_phase,1),1)/...
         sqrt(size(all_psd,1)));
      bar(1.1:1:3.1,temp2,0.2,'FaceColor','b');
      hold on
      errorbar(1.1:1:3.1,temp2,temp_er2,'k','LineStyle','none');
      xlim([0.5 3.5])
      xticks([1 2 3]);
      xticklabels({'Endo','Neuro','Myo'})

      xlabel('Frequency bands');
      ylabel('\DeltaP (%)');
      if i_phase == 3
         title({['Channel ',num2str(i_channel)],...
            phase_list{i_phase}})
      else
         title(phase_list{i_phase})
      end

   end
   count = count + 1;
end
% === plot percentage change ===
```

C.2.4 Compare FC of different period pairs for both tPBM and sham sessions

```
%%%%%%%%%%%%%%%%%%%%%%%%%%%%%%%%%%%%%%%%%%%%%%%%%%%%%%%%%%%%%%%%%%%%%%%%%%%
% Compare functional connectivity of different period pairs for both tPBM
% and sham sessions
%%%%%%%%%%%%%%%%%%%%%%%%%%%%%%%%%%%%%%%%%%%%%%%%%%%%%%%%%%%%%%%%%%%%%%%%%%%
clear
close all
```

```matlab
clc

root_fd = uigetdir; % folder for saving results
main_fd = uigetdir; % folder containing the FC results

phase_fd = {'pre','stim','post'};

corr_pos_bl = 1;

input_signal = 'oxy';

% declare the interested ISO frequency band ('endo','neuro','myo')
freq_band = 'myo';
freq_name = 'Myogenic';

save_name = ['result_ttest_FC_corr_matlab_pos_',...
   num2str(corr_pos_bl),'_',freq_band,...
   '_',input_signal,'_all_channels_rangepos'];

save_fd = [root_fd,save_name,'/'];

if ~isfolder(save_fd)
   mkdir(save_fd)
end

phase_list = {'Pre','Stim','Post'};

nb_subject = 19;
q = 0.05;

all_channel = 1:111;
excl_list = [];
roi_list = [3,4,7,9,12,16,17,18,23,31,32,43];
not_roi_list = setdiff(all_channel,roi_list);

nb_ch_pair = (length(all_channel)-length(excl_list))*length(roi_list)...
   -(length(roi_list)*(length(roi_list)-1)/2);
p_lim = 0.05/nb_ch_pair;
tstat_lim = abs(tinv(p_lim/2,nb_subject-1));

exp_type = {'PBO','TRT'};

all_corr = zeros(length(all_channel),length(all_channel),...
```

```
   nb_subject,length(phase_fd),length(exp_type));

for i_exp = 1:length(exp_type)
   for i_phase = 1:length(phase_fd)
      file_list = dir([main_fd,phase_fd{i_phase},...
                  '/',exp_type{i_exp},'/*.mat']);
      for i_sub = 1:nb_subject
         % load FC results
         corr_result = load([main_fd,phase_fd{i_phase},...
                  '/',exp_type{i_exp},'/',...
                  file_list(i_sub).name]);

         all_corr(:,:,i_sub,i_phase,i_exp) = corr_result.sfzRMatrix_oxy;
      end
   end
end

if corr_pos_bl == 1
   all_corr(all_corr<0)=0;
end


%% === tPBM – Different phases comparison ===
h = zeros(length(phase_fd),length(all_channel),length(all_channel));
p = zeros(length(phase_fd),length(all_channel),length(all_channel));
tstat = zeros(length(phase_fd),length(all_channel),length(all_channel));

phase_pair = 1;
for i_phase = 1:length(phase_fd)–1
   for j_phase = i_phase+1:length(phase_fd)
      for i_channel=1:length(all_channel)–1
         for j_channel = i_channel+1:length(all_channel)

            temp1 = squeeze(all_corr(i_channel,j_channel,:,...
               i_phase,2));
            temp2 = squeeze(all_corr(i_channel,j_channel,:,...
               j_phase,2));

            temp11=temp1(~(isnan(temp1)|isnan(temp2)));
            temp21=temp2(~(isnan(temp1)|isnan(temp2)));

            temp1=temp11(~(isinf(temp11)|isinf(temp21)));
            temp2=temp21(~(isinf(temp11)|isinf(temp21)));
```

```

            [h(phase_pair,i_channel,j_channel),...
               p(phase_pair,i_channel,j_channel),c,...
               ts] = ...
               ttest(temp2,temp1);
            tstat(phase_pair,i_channel,j_channel) = ts.tstat;
         end
      end

      %% === FDR correction ===

      temp_p_FDR = squeeze(p(phase_pair,:,:));
      temp_p_FDR = temp_p_FDR + temp_p_FDR';

      p_for_FDR = temp_p_FDR;

      p_for_FDR(excl_list,:)=0;
      p_for_FDR(:,excl_list)=0;
      p_for_FDR = triu(p_for_FDR);
      p_for_FDR(not_roi_list,not_roi_list)=0;

      roi_p = p_for_FDR(find(p_for_FDR));
      roi_p = sort(roi_p(:));
      V = length(roi_p);
      I = (1:V)';
      pID = roi_p(max(find(roi_p<=I/V*q)));

      [h_p, crit_p, adj_ci_cvrg, adj_p]=fdr_bh(roi_p,q,'pdep','yes');
      % === FDR correction ===

      % === create data file for plotting significant changes in FC ===
      temp = squeeze(tstat(phase_pair,:,:));

      temp1=triu(temp)+triu(temp,1)';
      temp1(isnan(temp1))=0;
      temp1(isinf(temp1))=0;

      temp1(:,excl_list) = 0;
      temp1(excl_list,:) = 0;
      temp1(not_roi_list,not_roi_list)=0;

      if crit_p>0
         crit_tstat = abs(temp1(find(p_for_FDR==crit_p,1,'first')));
```

```
      else
         crit_tstat = 5;
      end

      fileID = fopen([save_fd,...
         save_name,'_',phase_list{j_phase},'-',phase_list{i_phase},...
         '_FDR_q_',strrep(num2str(q),'.','-'),...
         '_TRT',...
         '.edge'],'w');
      fprintf(fileID,'%.3f \t',temp1(:)');
      fclose(fileID);
      % === create data file for plotting significant changes in FC ===

      phase_pair = phase_pair+1;
   end
end
```

```
% fdr_bh() - Executes the Benjamini & Hochberg (1995) and the Benjamini &
% Yekutieli (2001) procedure for controlling the false discovery
% rate (FDR) of a family of hypothesis tests. FDR is the expected
% proportion of rejected hypotheses that are mistakenly rejected
% (i.e., the null hypothesis is actually true for those tests).
% FDR is a somewhat less conservative/more powerful method for
% correcting for multiple comparisons than procedures like Bonferroni
% correction that provide strong control of the family-wise
% error rate (i.e., the probability that one or more null
% hypotheses are mistakenly rejected).
%
% This function also returns the false coverage-statement rate
% (FCR)-adjusted selected confidence interval coverage (i.e.,
% the coverage needed to construct multiple comparison corrected
% confidence intervals that correspond to the FDR-adjusted p-values).
%
%
% Usage:
% >> [h, crit_p, adj_ci_cvrg, adj_p]=fdr_bh(pvals,q,method,report);
%
% Required Input:
% pvals - A vector or matrix (two dimensions or more) containing the
% p-value of each individual test in a family of tests.
%
% Optional Inputs:
% q - The desired false discovery rate. {default: 0.05}
```

```
% method — ['pdep' or 'dep'] If 'pdep,' the original Bejnamini & Hochberg
% FDR procedure is used, which is guaranteed to be accurate if
% the individual tests are independent or positively dependent
% (e.g., Gaussian variables that are positively correlated or
% independent). If 'dep,' the FDR procedure
% described in Benjamini & Yekutieli (2001) that is guaranteed
% to be accurate for any test dependency structure (e.g.,
% Gaussian variables with any covariance matrix) is used. 'dep'
% is always appropriate to use but is less powerful than 'pdep.'
% {default: 'pdep'}
% report — ['yes' or 'no'] If 'yes', a brief summary of FDR results are
% output to the MATLAB command line {default: 'no'}
%
%
% Outputs:
% h — A binary vector or matrix of the same size as the input pvals.
% If the ith element of h is 1, then the test that produced the
% ith p—value in pvals is significant (i.e., the null hypothesis
% of the test is rejected).
% crit_p — All uncorrected p—values less than or equal to crit_p are
% significant (i.e., their null hypotheses are rejected). If
% no p—values are significant, crit_p=0.
% adj_ci_cvrg — The FCR—adjusted BH— or BY—selected
% confidence interval coverage. For any p—values that
% are significant after FDR adjustment, this gives you the
% proportion of coverage (e.g., 0.99) you should use when generating
% confidence intervals for those parameters. In other words,
% this allows you to correct your confidence intervals for
% multiple comparisons. You can NOT obtain confidence intervals
% for non—significant p—values. The adjusted confidence intervals
% guarantee that the expected FCR is less than or equal to q
% if using the appropriate FDR control algorithm for the
% dependency structure of your data (Benjamini & Yekutieli, 2005).
% FCR (i.e., false coverage—statement rate) is the proportion
% of confidence intervals you construct
% that miss the true value of the parameter. adj_ci=NaN if no
% p—values are significant after adjustment.
% adj_p — All adjusted p—values less than or equal to q are significant
% (i.e., their null hypotheses are rejected). Note, adjusted
% p—values can be greater than 1.
%
%
% References:
```

```
% Benjamini, Y. & Hochberg, Y. (1995) Controlling the false discovery
% rate: A practical and powerful approach to multiple testing. Journal
% of the Royal Statistical Society, Series B (Methodological). 57(1),
% 289—300.
%
% Benjamini, Y. & Yekutieli, D. (2001) The control of the false discovery
% rate in multiple testing under dependency. The Annals of Statistics.
% 29(4), 1165—1188.
%
% Benjamini, Y., & Yekutieli, D. (2005). False discovery rate?adjusted
% multiple confidence intervals for selected parameters. Journal of the
% American Statistical Association, 100(469), 71?81. doi:10.1198/016214504000001907
%
%
% Example:
% nullVars=randn(12,15);
% [~, p_null]=ttest(nullVars); %15 tests where the null hypothesis
% %is true
% effectVars=randn(12,5)+1;
% [~, p_effect]=ttest(effectVars); %5 tests where the null
% %hypothesis is false
% [h, crit_p, adj_ci_cvrg, adj_p]=fdr_bh([p_null p_effect],.05,'pdep','yes');
% data=[nullVars effectVars];
% fcr_adj_cis=NaN*zeros(2,20); %initialize confidence interval bounds to NaN
% if ~isnan(adj_ci_cvrg),
% sigIds=find(h);
% fcr_adj_cis(:,sigIds)=tCIs(data(:,sigIds),adj_ci_cvrg); % tCIs.m is available on the
% %Mathworks File Exchagne
% end
%
%
% For a review of false discovery rate control and other contemporary
% techniques for correcting for multiple comparisons see:
%
% Groppe, D.M., Urbach, T.P., & Kutas, M. (2011) Mass univariate analysis
% of event—related brain potentials/fields I: A critical tutorial review.
% Psychophysiology, 48(12) pp. 1711—1725, DOI: 10.1111/j.1469—8986.2011.01273.x
% http://www.cogsci.ucsd.edu/~dgroppe/PUBLICATIONS/mass_uni_preprint1.pdf
%
%
% For a review of FCR—adjusted confidence intervals (CIs) and other techniques
% for adjusting CIs for multiple comparisons see:
```

```
%
% Groppe, D.M. (in press) Combating the scientific decline effect with
% confidence (intervals). Psychophysiology.
% http://biorxiv.org/content/biorxiv/early/2015/12/10/034074.full.pdf
%
%
% Author:
% David M. Groppe
% Kutaslab
% Dept. of Cognitive Science
% University of California, San Diego
% March 24, 2010

%%%%%%%%%%%%%%%% REVISION LOG %%%%%%%%%%%%%%%%%
%
% 5/7/2010—Added FDR adjusted p—values
% 5/14/2013— D.H.J. Poot, Erasmus MC, improved run—time complexity
% 10/2015— Now returns FCR adjusted confidence intervals

function [h, crit_p, adj_ci_cvrg, adj_p]=fdr_bh(pvals,q,method,report)

if nargin<1
   error('You need to provide a vector or matrix of p—values.');
else
   if ~isempty(find(pvals<0,1))
      error('Some p—values are less than 0.');
   elseif ~isempty(find(pvals>1,1))
      error('Some p—values are greater than 1.');
   end
end

if nargin<2
   q=.05;
end

if nargin<3
   method='pdep';
end

if nargin<4
   report='no';
end

```

```
s=size(pvals);
if (length(s)>2) || s(1)>1
   [p_sorted, sort_ids]=sort(reshape(pvals,1,prod(s)));
else
   %p—values are already a row vector
   [p_sorted, sort_ids]=sort(pvals);
end
[dummy, unsort_ids]=sort(sort_ids); %indexes to return p_sorted to pvals order
m=length(p_sorted); %number of tests

if strcmpi(method,'pdep')
   %BH procedure for independence or positive dependence
   thresh=(1:m)*q/m;
   wtd_p=m*p_sorted./(1:m);

elseif strcmpi(method,'dep')
   %BH procedure for any dependency structure
   denom=m*sum(1./(1:m));
   thresh=(1:m)*q/denom;
   wtd_p=denom*p_sorted./[1:m];
   %Note, it can produce adjusted p—values greater than 1!
   %compute adjusted p—values
else
   error('Argument ''method'' needs to be ''pdep'' or ''dep''.');
end

if nargout>3
   %compute adjusted p—values; This can be a bit computationally intensive
   adj_p=zeros(1,m)*NaN;
   [wtd_p_sorted, wtd_p_sindex] = sort( wtd_p );
   nextfill = 1;
   for k = 1 : m
      if wtd_p_sindex(k)>=nextfill
         adj_p(nextfill:wtd_p_sindex(k)) = wtd_p_sorted(k);
         nextfill = wtd_p_sindex(k)+1;
         if nextfill>m
            break;
         end
      end
   end
   adj_p=reshape(adj_p(unsort_ids),s);
end

```

```
rej=p_sorted<=thresh;
max_id=find(rej,1,'last'); %find greatest significant pvalue
if isempty(max_id)
   crit_p=0;
   h=pvals*0;
   adj_ci_cvrg=NaN;
else
   crit_p=p_sorted(max_id);
   h=pvals<=crit_p;
   adj_ci_cvrg=1-thresh(max_id);
end

if strcmpi(report,'yes')
   n_sig=sum(p_sorted<=crit_p);
   if n_sig==1
      fprintf('Out of %d tests, %d is significant using a false discovery rate of %f.\n',m,n_sig,q);
   else
      fprintf('Out of %d tests, %d are significant using a false discovery rate of %f.\n',m,n_sig,q);
   end
   if strcmpi(method,'pdep')
      fprintf('FDR/FCR procedure used is guaranteed valid for independent or positively dependent tests.\n');
   else
      fprintf('FDR/FCR procedure used is guaranteed valid for independent or dependent tests.\n');
   end
end
```

C.3 Quantification of changes in chromophore concentration and error propagation analysis

C.3.1 Quantification of changes in chromophore concentration using the modified Beer-Lambert law

```
function [DPF,eps_HbO,eps_Hb,eps_CCO] = DPF_ext_coef_NT(wl_list)
%%%%%%%%%%%%%%%%%%%%%%%%%%%%%%%%%%%%%%%%%%%%%%%%%%%%%%%%%%%%%%%%%%%%%%%%%%
% Calculate the extinction coefficients of HbO, Hb, and CCO and the
% differential pathlength factor using the diffusion theory
% Input:
% - wl_list: list of wavelengths used to calculate the changes in
% chromophore concentration
```

```matlab
% Output:
% - DPF: differential pathlength factor
% - eps_HbO,eps_Hb,eps_CCO: extinction coefficients of HbO, Hb, and CCO
%%%%%%%%%%%%%%%%%%%%%%%%%%%%%%%%%%%%%%%%%%%%%%%%%%%%%%%%%%%%%%%%%%%%%%%%%%

%% Estimate the extinction coefficients of HbO, Hb, CCO
% Load pre-estimated absorption values of HbO-Hb-CCO-fat-water at
% different wavelengths
ext=xlsread('Extinction_coefficients');
[~,wl_list_idx] = ismember(wl_list,ext(:,1));
eps_HbO=ext(wl_list_idx,2);
eps_Hb=ext(wl_list_idx,3);
eps_CCO=ext(wl_list_idx,4);

%% Calculate DPF
% ua and us of two wavelengths
% Two wavelengths and their corresponding ua and us need to be changed
% depending on the experimental setup
wl1 = 750;
wl2 = 830;
ua1=0.129; % obtain by ISS
ua2=0.129;
us1=12.60;
us2=11.4;
id1 = find(ext(:,1)==wl1);
id2 = find(ext(:,1)==wl2);

HbO=(ext(id2,3)*(ua1)-ext(id1,3)*(ua2))/...
   (log(10)*(ext(id2,3)*ext(id1,2)-ext(id2,2)*ext(id1,3)));
Hb=(ext(id1,2)*(ua2)-ext(id2,2)*(ua1))/...
   (log(10)*(ext(id2,3)*ext(id1,2)-ext(id2,2)*ext(id1,3)));
a=exp((log(wl1)*log(us2/us1))/log(wl1/wl2)+log(us1));
b=log(us2/us1)/log(wl1/wl2);
us=a*((wl_list).^(-b));
us=us';

sub_ext=(ext(wl_list_idx,:)); % get pre-estimated data for interest wavelengths
uaa(:,:)=HbO*sub_ext(:,2)+Hb*sub_ext(:,3);
uaa=uaa*log(10);
ua=uaa;
DPF=((sqrt(3*us))./(2*(sqrt(ua))));
```

```matlab
function [Conc,Va]=calc_HbO_Hb_CCO(...
```

```
   org_spectrum_data,org_wavelength,r,start_point,wl_list_calc,detrend_bl)
%%%%%%%%%%%%%%%%%%%%%%%%%%%%%%%%%%%%%%%%%%%%%%%%%%%%%%%%%%%%%%%%%%%%%%%%%%
% Calculate the changes in chromophore concentration based the modified
% Beer-Lambert law and the error propagation matrix calculated from the SNR
% of the measurement system.
% Input:
% - org_spectrum_data [nb_wavelength x nb_measurement x nb_channel]: data
% from spectrometer
% - org_wavelength [nb_wavelength x 1]: whole wavelength list from the
% spectrometer
% - r: distance between light source and detector (cm)
% - start_point: point for starting calculate concentration changes
% - wl_list_calc [1 x nb_wl]: wavelength list used to calculate
% concentration changes (must be sub-list of the wavelength list from
% the spectrometer)
% - detrend_bl: 1 for linear detrending, 0 for no detrending (default)
% Output:
% - Conc: changes in chromophore concentration (muM)
% - Va: error propagation matrix calculated from the SNR of the measurement
% system
%%%%%%%%%%%%%%%%%%%%%%%%%%%%%%%%%%%%%%%%%%%%%%%%%%%%%%%%%%%%%%%%%%%%%%%%%%

if nargin < 6
   detrend_bl = 0;
end

[DPF,HbO,Hb,CCO] = DPF_ext_coef_NT(wl_list_calc);

XT(1,:) = r*DPF.*HbO;
XT(2,:) = r*DPF.*Hb;
XT(3,:) = r*DPF.*CCO;

%% fix wavelength
ii = [true;diff(floor(org_wavelength)) ~= 0];
wavelength = floor(org_wavelength(ii));
spectrum_data = zeros(length(wavelength),...
   size(org_spectrum_data,2));
for i_measure = 1:size(org_spectrum_data,2)
   spectrum_data(:,i_measure) = accumarray(cumsum(ii),...
      org_spectrum_data(:,i_measure),[],@mean);
end

[~,wl_list_idx] = ismember(wl_list_calc,wavelength);
```

```matlab

%% loop fitting
for i_channel = 1:size(spectrum_data,3)

   current_temp_data = spectrum_data(:,:,i_channel);
   baseline=mean(current_temp_data(:,1:start_point-1),2);

   dOD_raw = log10(repmat(baseline,1,size(spectrum_data,2)-start_point+1))-...
      log10(current_temp_data(:,start_point:end));
   if detrend_bl
      detrend_dOD = detrend(dOD_raw',1);
      detrend_dOD = detrend_dOD';
   else
      detrend_dOD = dOD_raw;
   end

   %for loop for all data sets apart from baselines
   for jj=start_point:size(spectrum_data,2)
      dOD(:,2)=detrend_dOD(:,jj-start_point+1);% change of signal
      dOD(:,1)=wavelength(:,1);
      % select only the data of interested wavelengths
      final_dOD=dOD(wl_list_idx,:);

      % save all dOD data to estimate the theoretical error propagation
      all_OD(jj-start_point+1,:) = final_dOD(:,2);

      Y0=[1e-6; 1e-6; 1e-6]; % fit for the least-square
      [Conc(:,jj),fmin4(:,jj),exitflag,out_stat]=...
         fminsearch(@oxyy,Y0,optimset('TolX',1e-20),r(i_channel),...
         DPF,HbO,Hb,CCO,final_dOD(:,2));

% % uncomment to check the fitted results
% ccco=Conc(3,jj);
% chbo=Conc(1,jj);
% chb=Conc(2,jj);
% fitted_line=(ccco*CCO+chbo*HbO+chb*Hb).*r(i_channel).*DPF;
   end
   % error propagation
   Va = inv(XT*inv(diag(var(all_OD)))*XT')*10^12;
   % changes in chromophore concentration (in muM)
   Conc=Conc*(10^6);
end
```

C.3.2 Monte Carlo simulation

```
%%%%%%%%%%%%%%%%%%%%%%%%%%%%%%%%%%%%%%%%%%%%%%%%%%%%%%%%%%%%%%%%%%%%%%%%%%
% Monte Carlo simulation to generate bbNIRS data of two physiological
% conditions
% Need MCmatlab program (https://github.com/ankrh/MCmatlab) to run the
% simulation
%%%%%%%%%%%%%%%%%%%%%%%%%%%%%%%%%%%%%%%%%%%%%%%%%%%%%%%%%%%%%%%%%%%%%%%%%%

clear
close all
clc

LS_x = 1;% light source location [cm]
LS_y = 0;% light source location [cm]
angle_list = 0;
wavelength_list = 780:900; % [nm]

det_x = -1; % detector location [cm]
det_y = 0; % [cm]
det_z = 0; % [cm]
det_r = 0.2; % [cm]

HbO_list=[40 45];
Hb_list=[26 23];

B = 0.01; % blood volume fraction
S = [0.7 0.8]; % oxygen saturation of hemoglobin
W = 0.75; % water volume fraction
F = 0.10; % fat volume fraction
Me = 0; % volume fraction of melanosomes
oxCCO = [0.1 0.4];
redCCO = [0.4 0.1];

global X1

nb_rep = 10;
norm_det_NFR = zeros(nb_rep,length(wavelength_list),length(HbO_list));

for i_rep = 1:nb_rep
   for i_hbo = 1:length(HbO_list)

      X1 = [B*S(i_hbo) B*(1-S(i_hbo)) W F Me oxCCO(i_hbo) redCCO(i_hbo)]';
```

```matlab

   for i_wavelength = 1:length(wavelength_list)

      %% Geometry definition
      model = MCmatlab.model;

      model.G.nx = 600; % Number of bins in the x direction
      model.G.ny = 600; % Number of bins in the y direction
      model.G.nz = 300; % Number of bins in the z direction
      model.G.Lx = 4; % [cm] x size of simulation cuboid
      model.G.Ly = 4; % [cm] y size of simulation cuboid
      model.G.Lz = 2; % [cm] z size of simulation cuboid

      model.G.mediaPropertiesFunc = @mediaPropertiesFunc; % Media properties defined as a function at the end of this file
      model.G.geomFunc = @geometryDefinition_ArmMeasurement; % Function to use for defining the distribution of media in the cuboid. Defined at the end of this m file.

      % Execution, do not modify the next line:
      model = defineGeometry(model);

      plot(model,'G');

      %% beam definition
      model.MC.simulationTimeRequested = .5; % [min] Time duration of the simulation
      model.MC.farFieldRes = 200;

      model.MC.beam.beamType = 0; % 0: Pencil beam, 1: Isotropically emitting point source, 2: Infinite plane wave, 3: Laguerre-Gaussian LG01 beam, 4: Radial-factorizable beam (e.g., a Gaussian beam), 5: X/Y factorizable beam (e.g., a rectangular LED emitter)

      model.MC.beam.xFocus = LS_x; % [cm] x position of focus
      model.MC.beam.yFocus = LS_y; % [cm] y position of focus
      model.MC.beam.zFocus = 0; % [cm] z position of focus

      model.MC.beam.theta = angle_list*pi/180; % [rad] Polar angle of beam center axis
      model.MC.beam.phi = 0; % [rad] Azimuthal angle of beam center axis
      model.MC.beam.psi = 0; % [rad] (Default: 0) Axial rotation angle of beam, relevant only for XY distributed beams
```

```matlab

        %% Light collector
        model.MC.useLightCollector = true;
        model.MC.LC.x = 0; % [cm] x position of either the center of the objective lens focal plane or the fiber tip
        model.MC.LC.y = 0; % [cm] y position
        model.MC.LC.z = 0; % [cm] z position

        model.MC.LC.theta = pi; % [rad] Polar angle of direction the light collector is facing
        model.MC.LC.phi = 0; % [rad] Azimuthal angle of direction the light collector is facing

        model.MC.LC.f = Inf; % [cm] Focal length of the objective lens (if light collector is a fiber, set this to Inf).
        model.MC.LC.diam = .5; % [cm] Diameter of the light collector aperture. For an ideal thin lens, this is 2*f*tan(asin(NA)).
        model.MC.LC.fieldSize = .5; % [cm] Field Size of the imaging system (diameter of area in object plane that gets imaged). Only used for finite f.
        model.MC.LC.NA = 0.22; % [-] Fiber NA. Only used for infinite f.

        model.MC.LC.res = 1; % X and Y resolution of light collector in pixels, only used for finite f


        %% Monte Carlo simulation

        model.MC.nPhotonsRequested = 5e7; % # of photons to launch

        model.MC.calcNFR = true; % (Default: true) If true, the 3D fluence rate output matrix NFR will be calculated. Set to false if you have a light collector and you're only interested in the image output.
        model.MC.calcNFRdet = true; % (Default: false) If true, the 3D fluence rate output matrix NFRdet will be calculated. Only photons that end up on the light collector are counted in NFRdet.
        model.MC.nExamplePaths = model.MC.nPhotonsRequested/10;

        model.MC.matchedInterfaces = true; % Assumes all refractive indices are the same
        model.MC.boundaryType = 1; % 0: No escaping boundaries, 1: All cuboid boundaries are escaping, 2: Top cuboid boundary only is escaping
```

```
         model.MC.wavelength = wavelength_list(i_wavelength); % [nm] Excitation wavelength, used for determination of optical properties for excitation light

         %% Execution, do not modify the next line:
         model = runMonteCarlo(model);

         %% plot results
         plot(model,'MC');

         %% detection intensity
         norm_det_NFR(i_rep,i_wavelength,i_hbo) = model.MC.LC.image;
         clear model
      end
   end
end

%% Geometry function(s)
% A geometry function takes as input X,Y,Z matrices as returned by the
% ndgrid MATLAB function as well as any parameters the user may have
% provided in the definition of Ginput. It returns the media matrix M,
% containing numerical values indicating the media type (as defined in
% mediaPropertiesFunc) at each voxel location.
function M = geometryDefinition_ArmMeasurement(X,Y,Z,parameters)
tissuedepth = .01;
M = ones(size(X))*1; % Air
M(Z > tissuedepth) = 2; % tissue
end

%% Media Properties function
% The media properties function defines all the optical and thermal
% properties of the media involved by constructing and returning a
% mediaProperties struct with various fields. As its input, the function
% takes the wavelength as well as any other parameters you might specify
% above in the model file, for example parameters that you might loop over
% in a for loop. Dependence on excitation fluence rate FR, temperature T or
% fractional heat damage FD can be specified as in examples 12-15.
function mediaProperties = mediaPropertiesFunc(wavelength,parameters)

global X1

ext=xlsread('extinction coefficients');
tt = sum(ext,2);
```

```
ttt = find(isnan(tt));
ext=ext(1:min(ttt),:);

load spectralLIB.mat
MU(:,1) = interp1(nmLIB,muaoxy,wavelength);
MU(:,2) = interp1(nmLIB,muadeoxy,wavelength);
MU(:,3) = interp1(nmLIB,muawater,wavelength);
MU(:,4) = interp1(nmLIB,muafat,wavelength);
MU(:,5) = interp1(nmLIB,muamel,wavelength);
MU(:,6) = interp1(ext(:,1),ext(:,10)*1e-3,wavelength);
MU(:,7) = interp1(ext(:,1),ext(:,11)*1e-3,wavelength);

j=1;
mediaProperties(j).name = 'air';
mediaProperties(j).mua = 1e-8;
mediaProperties(j).mus = 1e-8;
mediaProperties(j).g = 1;
mediaProperties(j).n = 1;
mediaProperties(j).VHC = 1.2e-3;
mediaProperties(j).TC = 0; % Real value is 2.6e-4, but we set it to zero to neglect the heat transport to air

j=2;
mediaProperties(j).name = 'tissue';
musp500 = 20;
fray = 0.2;
bmie = 1.0;
gg = 0.90;
musp = musp500*(fray*(wavelength/500).^-4 + (1-fray)*(wavelength/500).^-bmie);

mediaProperties(j).mua = MU*X1;

mediaProperties(j).mus = musp/(1-gg);
mediaProperties(j).g = gg;
mediaProperties(j).n = 1.3;
mediaProperties(j).VHC = 3391*1.109e-3;
mediaProperties(j).TC = 0.37e-2;
end
```

```
function [mua,musp] = mua_tissue_estimation(wavelength_list,B,S,W,F,Me,...
   oxCCO,redCCO)
%%%%%%%%%%%%%%%%%%%%%%%%%%%%%%%%%%%%%%%%%%%%%%%%%%%%%%%%%%%%%%%%%%%%%%%%
% Estimate the absorption and scattering coefficients of predefined
```

```
% simulation medium
% Input:
% — wavelength_list: interested wavelength combination (nm)
% — B: blood volume fraction
% — S: oxygen saturation of hemoglobin
% — W: water volume fraction
% — F: fat volume fraction
% — Me: volume fraction of melanosomes
% — oxCCO, redCCO: concentrations of oxCCO and reduced CCO (muM)
% Output:
% — mua: absorption coefficient (cm—1)
% — musp: reduced scattering coefficient (cm—1)
% Example:
% wavelength_list = 750:920;
% % Define the medium composition of the interested physiological conditions
% B = 0.01; % blood volume fraction
% S = [0.7 0.8]; % oxygen saturation of hemoglobin
% W = 0.75; % water volume fraction
% F = 0.10; % fat volume fraction
% Me = 0; % volume fraction of melanosomes
% oxCCO = [0.1 0.4]; % concentrations of oxCCO and reduced CCO
% redCCO = [0.4 0.1];
%%%%%%%%%%%%%%%%%%%%%%%%%%%%%%%%%%%%%%%%%%%%%%%%%%%%%%%%%%%%%%%%%%%%%%%%%%

ext=xlsread('extinction coefficients');
tt = sum(ext,2);
ttt = find(isnan(tt));
ext=ext(1:min(ttt),:);

load spectralLIB.mat

for i_cond = 1:length(S)
   X = [B*S(i_cond) B*(1—S(i_cond)) W F Me ]';
   X1 = [B*S(i_cond) B*(1—S(i_cond)) W F Me...
      oxCCO(i_cond) redCCO(i_cond)]';
   for i_wl = 1:length(wavelength_list)
      wavelength = wavelength_list(i_wl);

      MU(:,1) = interp1(nmLIB,muaoxy,wavelength);
      MU(:,2) = interp1(nmLIB,muadeoxy,wavelength);
      MU(:,3) = interp1(nmLIB,muawater,wavelength);
      MU(:,4) = interp1(nmLIB,muafat,wavelength);
      MU(:,5) = interp1(nmLIB,muamel,wavelength);
```

```
      MU(:,6) = interp1(ext(:,1),ext(:,10)*1e-3,wavelength);
      MU(:,7) = interp1(ext(:,1),ext(:,11)*1e-3,wavelength);

      mua(i_wl,i_cond) = MU*X1;
   end
end

musp500 = 20;
fray = 0.2;
bmie = 1.0;
gg = 0.90;
musp = musp500*(fray*(wavelength_list/500).^-4 +...
   (1-fray)*(wavelength_list/500).^-bmie);
```